

1 The Atmospheric Potential Oxygen forward Model Intercomparison Project
2 (APO-MIP1): Evaluating simulated atmospheric transport of air-sea gas exchange
3 tracers and APO flux products

4 Yuming Jin^{1,2}, Britton B. Stephens¹, Matthew C. Long³, Naveen Chandra⁴, Frédéric Chevallier⁵,
5 Joram J.D. Hooghiem⁶, Ingrid T. Luijkx⁶, Shamil Maksyutov⁷, Eric J. Morgan⁸, Yosuke Niwa⁷,
6 Prabir K. Patra^{4,9}, Christian Rödenbeck¹⁰, Jesse Vance¹¹

7 1. Earth Observing Laboratory, NSF National Center for Atmospheric Research, Boulder, CO 80301,
8 USA

9 2. Advanced Study Program, NSF National Center for Atmospheric Research, Boulder, CO 80301

10 3. [C]Worthy, Boulder, CO 80302, USA

11 4. Research Institute for Global Change, Japan Agency for Marine-Earth Science and Technology,
12 Yokohama, 236-0001, Japan

13 5. Laboratoire des Sciences du Climat et de l'Environnement, LSCE/IPSL, CEA-CNRS-UVSQ,
14 Université Paris-Saclay, Gif-sur-Yvette, F-91198, France

15 6. Wageningen University, Environmental Sciences Group, Wageningen, 6700AA, The Netherlands

16 7. Earth System Division, National Institute for Environmental Studies, Tsukuba, 305-8506, Japan

17 8. Geosciences Research Division, Scripps Institution of Oceanography, University of California, San
18 Diego, La Jolla, CA 92093, USA

19 9. Seto Inland Sea Carbon Neutral Research Center, Hiroshima University, Higashi-Hiroshima, 739-8529,
20 Japan

21 10. Max Planck Institute for Biogeochemistry, Jena, 07745, Germany

22 11. Ebb Carbon, San Carlos, CA 94070, USA

23 Correspondence: Yuming Jin (yumingjin@ucar.edu)

24 Abstract

25 Atmospheric Potential Oxygen (APO, defined as $O_2 + 1.1 \times CO_2$) is primarily a tracer of ocean
26 biogeochemistry and fossil fuel burning. APO exhibits strong seasonal variability at mid-to-high
27 latitudes, driven mainly by seasonal air-sea O_2 exchange with small impact from fossil fuel
28 burning, exhibiting strong seasonal variability over mid-to-high latitudes. We present results
29 from the first version of the Atmospheric Potential Oxygen forward Model Intercomparison
30 Project (APO-MIP1), which forward transports three air-sea APO flux products in eight
31 atmospheric transport models or model variants, aiming to evaluate atmospheric transport and
32 flux representations by comparing simulations against surface station, airborne, and shipboard
33 observations of APO. We find significant spread and bias in APO simulations at eastern Pacific
34 surface stations, indicating inconsistencies in representing vertical and coastal atmospheric
35 mixing. A framework using airborne APO observations demonstrates that most atmospheric
36 transport models (ATMs) participating in APO-MIP1 overestimate tracer diffusive mixing across
37 moist isentropes (i.e., diabatic mixing) in mid-latitudes. This framework also enables us to
38 isolate ATM-related biases in simulated APO distributions using independent mixing constraints
39 derived from moist static energy budgets from reanalysis, thereby allowing us to assess
40 large-scale features in air-sea APO flux products. Furthermore, shipboard observations show that
41 ATMs are unable to reproduce seasonal APO gradients over Drake Passage and near Palmer
42 Station, Antarctica, which could arise from uncertainties in APO fluxes or model transport. The
43 transport simulations and flux products from APO-MIP1 provide valuable resources for
44 developing new APO flux inversions and evaluating ocean biogeochemical processes.

45 Short Summary

46 We carry out a comprehensive atmospheric transport model (ATM) intercomparison project. This
47 project aims to evaluate errors in ATMs and three air-sea O_2 exchange products by comparing
48 model simulations with observations collected from surface stations, ships, and aircraft. We also
49 present a model evaluation framework to independently quantify transport-related and
50 flux-related biases that contribute to model-observation discrepancies in atmospheric tracer
51 distributions.

52 1. Introduction

53 Atmospheric potential oxygen (APO), defined as the weighted sum of O_2 and CO_2 concentration
54 ($APO \approx O_2 + 1.1 CO_2$), is an important tracer of fossil fuel burning and ocean biogeochemical
55 processes (Stephens et al., 1998). APO is intended to be unaffected by terrestrial photosynthesis
56 and respiration due to the cancellation of O_2 and CO_2 exchange at an approximate $O_2:C$ ratio of
57 -1.1 (Severinghaus, 1995). APO exhibits a large seasonal cycle driven mainly by air-sea O_2
58 exchange due to upper ocean biological activities, deep water ventilation, and thermally induced
59 O_2 solubility changes. Seasonal APO variability is also slightly affected by the air-sea exchange
60 of CO_2 and N_2 (Manning and Keeling, 2006). APO is decreasing in the atmosphere due to fossil
61 fuel combustion, which acts as an O_2 sink and CO_2 source with a more negative $O_2:CO_2$ ratio
62 (global mean ~ -1.4) compared to the assumed -1.1 ratio from terrestrial processes. Although
63 fossil fuel combustion contributes to an annual interhemispheric gradient that has lower APO in
64 the Northern Hemisphere, it has only a minor effect on the seasonal cycle globally (Keeling &
65 Manning, 2014).

66 APO measurements provide critical constraints on seasonal air-sea O_2 fluxes, which have been
67 used to estimate air-sea gas exchange rates and ocean net community production (NCP), and to
68 benchmark marine NCP in Earth system models (Naegler et al., 2007; Nevison et al., 2018,
69 2012, 2015, 2016). APO has been used for improved partitioning of ocean and land carbon sinks
70 (Friedlingstein et al., 2025; Manning and Keeling, 2006), to constrain ocean heat uptake and
71 meridional heat transport (Resplandy et al., 2016, 2019), and to quantify fossil fuel emissions
72 (Pickers et al., 2022; Rödenbeck et al., 2023). APO measurements are available at surface
73 stations (e.g., Adcock et al., 2023; Battle et al., 2006; Goto et al., 2017; Keeling & Manning,
74 2014; Manning & Keeling, 2006; Nguyen et al., 2022; Tohjima et al., 2019), on ship transects
75 (e.g., Ishidoya et al., 2016; Pickers et al., 2017; Stephens et al., 2003; Thompson et al., 2007;
76 Tohjima et al., 2012, 2015, 2024), and from aircraft (e.g., Bent, 2014; Ishidoya et al., 2012; Jin et
77 al., 2023; Langenfelds, 2002; Morgan et al., 2021; Stephens et al., 2018, 2021).

78 Global-scale air-sea APO fluxes have been estimated from APO measurements and an ATM
79 within a Bayesian inversion framework (Rödenbeck et al., 2008). ATMs are also used to forward
80 transport APO fluxes simulated from ocean biogeochemistry models (Carroll et al., 2020; Yeager
81 et al., 2022) and surface ocean dissolved oxygen (DO) measurements (Garcia and Keeling, 2001;

82 Najjar and Keeling, 2000) to compare with atmospheric observations, providing a basis for
83 model and flux product evaluation (Jin et al., 2023; Keeling et al., 1998; Stephens et al., 1998).
84 However, using atmospheric data to evaluate flux products and to derive fluxes through
85 inversion is fundamentally limited by biases in ATMs, particularly in their representation of
86 vertical transport and diabatic mixing (Jin et al., 2024; Naegler et al., 2007; Nevison et al., 2008;
87 Schuh et al., 2019; Schuh and Jacobson, 2023; Stephens et al., 2007). The systematic
88 uncertainties in transport modeling limit inversions of APO, CO₂, and other greenhouse gases,
89 underscoring the need for independent transport bias assessments to advance global carbon
90 budget constraints.

91 To address uncertainty in ATMs for studying large-scale tracer atmospheric transport and the
92 corresponding surface fluxes, several community model intercomparison (TransCom) projects
93 have been established for various tracers including CO₂ (Baker et al., 2006; Gurney et al., 2003,
94 2004; Law et al., 2008; Patra et al., 2008), N₂O (Thompson et al., 2014), SF₆ (Denning et al.,
95 1999), SF₆ and CH₄ jointly (Patra et al., 2011), as well as an age of air tracer (Krol et al., 2018).
96 Blaine (2005) coordinated a TransCom O₂ experiment to compare model simulations of the O₂
97 seasonal cycle across the Scripps O₂ network. While this experiment provided valuable initial
98 insights into ATM performance in simulating atmospheric O₂ from ocean fluxes, substantial
99 advances in ATMs and more data collected also from aircraft and ships since then motivate an
100 updated intercomparison study with more extensive model-data comparisons and analyses. More
101 recently, CO₂ inversion intercomparisons have been coordinated through the OCO-2 MIP
102 (Crowell et al., 2019; Peiro et al., 2022; Byrne et al., 2023) and the Global Carbon Project (e.g.,
103 Friedlingstein et al., 2025). These experiments reveal substantial spread in forward tracer (e.g.,
104 CO₂) atmospheric distribution and inverted surface fluxes, driven by different ATMs and
105 inversion setups. The spread in forward transport simulations stems from multiple factors,
106 including the choice of wind fields from various reanalysis products or online simulation,
107 regridding fine resolution meteorological data to coarse model grids, the advection scheme that
108 governs large-scale mixing, and parameterized sub-grid processes, such as boundary layer
109 mixing and deep convection. Despite the complexity of different transport pathways, long-lived
110 tracers (e.g., CO₂ and O₂) at mid-latitudes tend to show tracer distributions that are aligned with
111 moist potential temperature (θ_e) surfaces. This is because θ_e surfaces are preferential surfaces for

112 mixing, leading to rapid along- θ_e mixing and slow cross- θ_e mixing (Bailey et al., 2019; Jin et al.,
113 2021; Miyazaki et al., 2008; Parazoo et al., 2011).

114 It is a critical challenge to accurately quantify the rate-limiting cross- θ_e mixing time-scales,
115 which are largely driven by diabatic processes including moist convection and radiative cooling.
116 Here, we define “diabatic mixing rates” as diffusivities that are inversely related to cross- θ_e
117 mixing time-scales. These mixing rates are important for determining the large-scale tracer
118 distribution in ATMs. Jin et al. (2024) established a framework to calculate cross- θ_e mixing rates
119 from ATMs and moist static energy (MSE) budgets from reanalysis based on a mass-indexed
120 isentropic coordinate called M_{θ_e} (Jin et al., 2021). This framework also allows cross- θ_e tracer
121 gradients from airborne observations to provide independent constraints on diabatic mixing. Jin
122 et al. (2024) tested four ATMs used in CO_2 inversions, showing that these models tend to have
123 too fast mixing in the mid-latitudes of the Southern Hemisphere in the austral summer. The too
124 fast mixing is also confirmed by the fact that models simulate smaller CO_2 gradients compared to
125 airborne observations, which is an independent constraint on the mixing rate. The mixing rate
126 constraint and CO_2 gradient constraint also have implications for biases in the inverse model
127 estimates, indicating a too large summer-time Southern Ocean (SO) CO_2 sink. This framework
128 provides a system for independently evaluating transport simulations and flux estimates.

129 Previous TransCom experiments focused primarily on tracers that only have significant sources
130 and sinks over the land, and large seasonal flux cycles tied to the northern terrestrial biosphere.
131 In contrast, APO is a tracer of surface ocean exchange with the largest seasonal variability
132 observed over mid-to-high latitude oceans in both hemispheres. APO offers a distinct perspective
133 for studying atmospheric mixing within and above the marine boundary layer, the long-range
134 tracer transport into and out of the remote Southern Hemisphere, and the ability for inverting
135 tracer flux over the SO from atmospheric measurements.

136 Here we use output from the APO-MIP1 (Stephens et al., 2025), which generated a suite of
137 forward ATM simulations of APO and its components (air-sea O_2 , CO_2 , and N_2 flux, and fossil
138 fuel CO_2 emission and O_2 uptake) from different source fields. This effort was initially motivated
139 by a need to support the calibration of hemispheric-scale seasonal air-sea APO flux estimates
140 from spatially and temporally sparse observations from airborne campaigns (e.g., Jin et al.,

2023), stations, and ships. Here we focus on the other goals of APO-MIP1 which were to use atmospheric APO observations to characterize errors in ATMs and APO flux products.

In Section 2, we describe APO measurements from surface stations, aircraft, and ships, and the experimental design of APO-MIP1. ~~using eight ATMs to simulate transport of three ocean APO flux products, and two fossil fuel products.~~ In Section 3.12, we evaluate simulations against observations, revealing large model spread and errors at eastern Pacific surface stations due to mixing uncertainties, while airborne column-average data show smaller cross-ATMs variability and errors. In Section 3.23, we analyze diabatic mixing rates, demonstrating that ATMs generally overestimate mid-latitude mixing in both hemispheres, allowing us to separate transport and flux-related biases. In Section 3.34, we examine simulations of shipboard data around Drake Passage and the Antarctic Peninsula, revealing that current ATMs and flux products underestimate meridional gradients in APO seasonal amplitude from 53-65°S. The models also fail to capture the APO contrast between Palmer Station flask samples and nearby in-situ ship data due to limitations in representing local topographic flows with coarse-resolution ATMs. In Section 3.4, we discuss the broader implications of our analysis for developing methods to identify processes that introduce transport biases and for improving atmospheric transport modeling.

2. Materials and Methods

2.1 Definition of APO

APO in the unit of per meg (unit-see Keeling et al., 1998) is calculated from atmospheric observations of relative changes in the O₂/N₂ ratio (per meg) and CO₂ mole fraction (ppm) according to Stephens et al. (1998) as

$$APO \approx \delta(O_2/N_2) + \frac{1.1}{x_{O_2}} (CO_2 - 350), \quad (1)$$

with

164

$$\delta(O_2/N_2) = \left(\frac{(\frac{O_2}{N_2})_{sample}}{(\frac{O_2}{N_2})_{reference}} - 1 \right) \cdot 10^6. \quad (2)$$

165 The factor 1.1 represents the approximate exchange ratio of O_2 to CO_2 in terrestrial biospheric
 166 processes (Severinghaus, 1995). We note that this ratio generally varies from 1.01 to 1.14 in
 167 aboveground carbon pools across different temporal and spatial scales (Gallagher et al., 2017;
 168 Hockaday et al., 2009; Keeling, 1988; Worrall et al., 2013). This ratio also exhibits diurnal
 169 change and varies between respiration and photosynthesis in biosphere-atmosphere O_2 and CO_2
 170 exchanges (Faassen et al., 2023, 2024). With our focus on seasonal variations, we use 1.1 as
 171 representative of the O_2 to CO_2 exchange ratio during seasonal growth and decay of terrestrial
 172 biota. A sensitivity test in Jin et al. (2023) showed that varying this ratio by ± 0.05 ~~has~~ only leads
 173 to $\pm 5.1\%$ changes in hemispheric average APO. The impact on APO seasonal cycle amplitude
 174 (SCA) is $\pm 1.44\%$ and $\pm 0.41\%$ in the Northern and Southern Hemisphere, respectively. X_{O_2}
 175 (0.2094) is the reference dry-air mole fraction of O_2 used in the definition of the O_2 scale of the
 176 Scripps O_2 Program (Keeling et al., 2020). $\delta(O_2/N_2)$ is expressed in units of per meg, while CO_2
 177 is converted from ppm units to per meg units by subtracting a reference value of 350 ppm and
 178 then dividing by X_{O_2} . APO observations are typically expressed in per meg units, but they can be
 179 converted to ppm equivalent units by multiplying by X_{O_2} .

180 2.2 Atmospheric measurements

181 The APO-MIP1 (Stephens et al., 2025) required model output sampled to match a collection of
 182 surface station, airborne, and shipboard observations, and also accepted optional output at
 183 additional locations, at higher time resolution, and for full 3-D fields, as shown in Tables S1-2.
 184 Here we evaluate model APO simulations using observation data collected at 10 surface stations,
 185 on 10 airborne campaigns from three projects, and one repeated shipboard transect from 50
 186 cruises. We show sampling locations, and horizontal flight and ship tracks in Fig. 1. We use
 187 surface station APO measurements (2009 to 2018) from 10 sampling sites mainly in the Pacific
 188 from the Scripps O_2 Program surface flask network (Keeling & Manning, 2014; Manning &
 189 Keeling, 2006). The airborne measurements (Stephens et al., 2021) were made on the NSF
 190 NCAR GV aircraft during the HIAPER Pole-to-Pole Observation project from 2009 to 2011

(HIPPO, Wofsy, 2011) and the O₂/N₂ Ratio and CO₂ Airborne Southern Ocean Study in 2016 (ORCAS, Stephens et al., 2018), and from the NASA DC-8 aircraft during the Atmospheric Tomography Mission from 2016-2018 (ATom, Thompson et al., 2022). Shipboard measurements were made on transects crossing the Drake Passage by the NSF ARSV Laurence M. Gould from 2012-2017 (Stephens, 2025). Details of surface station, airborne, and shipboard APO measurements are provided in Appendix A.

As the primary focus of this study is the APO seasonal cycle and its latitudinal distribution, we remove interannual trends from the observational data. For surface station and airborne measurements, we remove the long-term trend by subtracting a deseasonalized cubic spline fit (smoothing parameter of 0.8) derived from the global mean APO time series using Scripps O₂ Program data following Hamme & Keeling (2008). For the ship data, we apply a similar detrending procedure but use only South Pole Observatory (SPO) data to derive the long-term trend.

2.3 Components of APO in the atmosphere and prescribed surface fluxes

APO exhibits seasonal variations primarily driven by air-sea exchange (F_{APO}^{ocn}), which comprises three components: air-sea exchange of O₂ ($F_{O_2}^{ocn}$), CO₂ ($F_{CO_2}^{ocn}$), and N₂ ($F_{N_2}^{ocn}$). Additionally, APO is influenced by fossil fuel emission of CO₂ ($F_{CO_2}^{ff}$) and consumption of O₂ ($F_{O_2}^{ff}$), which together combine to form a sink for APO due to fossil fuel burning (F_{APO}^{ff}). Fluxes are defined as positive to the atmosphere.

In this study, we primarily simulate APO by performing forward transport of these individual flux components in ATMs, except one inverse model flux product that provides net F_{APO}^{ocn} directly. We combined these components to calculate the net atmospheric APO anomalies in units of per meg as

$$\delta APO = \delta APO^{ocn} + \delta APO^{ff}, \quad (3)$$

with

$$\delta APO^{ocn} = \frac{1}{X_{O_2}} \cdot \Delta O_2^{ocn} - \frac{1}{X_{N_2}} \cdot \Delta N_2^{ocn} + \frac{1.1}{X_{O_2}} \cdot \Delta CO_2^{ocn}, \quad (4)$$

and

$$\delta APO^{ff} = \frac{1}{X_{O_2}} \cdot \Delta O_2^{ff} + \frac{1.1}{X_{O_2}} \cdot \Delta CO_2^{ff}. \quad (5)$$

where ΔO_2^{ocn} , ΔN_2^{ocn} , ΔCO_2^{ocn} , ΔO_2^{ff} , and ΔCO_2^{ff} represents the atmospheric fields in units of deviations in ppm of each flux component ($F_{O_2}^{ocn}$, $F_{CO_2}^{ocn}$, $F_{N_2}^{ocn}$, $F_{O_2}^{ff}$, and $F_{CO_2}^{ff}$) that is forward transport in the ATMs (Stephens et al., 1998). The δ sign denotes tracers in units of per meg.

We utilize three distinct ocean APO flux products: (1) the Jena product, which directly provides F_{APO}^{ocn} from an atmospheric APO inversion framework that assimilates surface station measurements (Rödenbeck et al., 2008); 2) the CESM product, an Earth System Model simulation with prognostic ocean biogeochemistry (Yeager et al., 2022; Long et al., 2021a) that generates separate flux components ($F_{O_2}^{ocn}$ and $F_{CO_2}^{ocn}$); and 3) the DISS product, which provides separate observation-based flux components incorporates surface ocean dissolved oxygen measurements (Garcia & Keeling, 2001; Resplandy et al., 2016) and pCO₂ data (Jersild et al., 2017; Landschützer et al., 2016). $F_{N_2}^{ocn}$ for CESM and DISS is estimated by scaling ocean heat fluxes from CESM and ERA-5, respectively, using the relationship of Keeling et al. (1993). For fossil fuel contributions, we employ the OCO2MIP product for CO₂ emissions (Basu & Nassar, 2021) and the GridFED database for coupled O₂ and CO₂ fluxes from fossil fuel combustion (Jones et al., 2021). Details of each product are provided in Appendix B. All flux fields were linearly interpolated from their original temporal and spatial resolution to 1° longitude × 1° latitude with daily temporal resolution from 1986 to 2020. When flux data were unavailable in the earlier portion of this time period (Jena and OCO2MIP), we set the corresponding fluxes to zero. Participating modelers were requested to simulate at least from 2009 to 2018, following three years of spin up from 2006 to 2008, and optionally longer (Table 1). In addition to Jena, which is simulated directly, we construct the two ΔAPO^{ocn} products using Eq. 4 and two ΔAPO^{ff}

products using Eq. 5, as described in Appendix B. Fig. 2 illustrates the seasonal and latitudinal flux patterns of these three ocean APO flux products and the fossil fuel APO flux from GridFed, which serves as our primary fossil fuel flux dataset in this study.

2.4 Atmospheric tracer transport models

We simulate each component of APO in the atmosphere using the flux fields described in Section 2.3, and eight ATMs (see Table 1). All tracer atmospheric fields are modeled as tracer deviations against an arbitrary background with concentrations in ppm dry air mole fraction (as for CO₂). These tracer mole fractions are later converted to deviations in units of per meg after subtracting the model-specific arbitrary reference according to Eq. 4. We describe key model parameters and setups below.

2.4.1 CAM-SD

The Community Atmosphere Model (CAM) version 6.0 is the atmospheric component of CESM2 (Danabasoglu et al., 2020). The version used here is run online with specified dynamics (SD), wherein the model is constrained with MERRA-2 reanalysis, and uncoupled from the other climate system components. Temperature and horizontal winds (*u* and *v*) are nudged to MERRA-2, 8 times per day, with a normalized strength coefficient of 0.25. Shallow convection is parameterized following the Cloud-Layers Unified by Binormals framework (CLUBB, Golaz et al., 2002), and deep convection is parameterized following Zhang & McFarlane (1995). CAM has not been used for tracer inversions, but has been evaluated extensively for its dynamical properties (e.g., Bailey et al., 2019; Kay et al., 2012)

2.4.2 CAMS_LMDZ

CAMS_LMDZ refers here to the offline transport model from the Atmospheric General Circulation Model of Laboratoire de Météorologie Dynamique, called LMDz. LMDz is the atmospheric component of the Earth System Model of Institut Pierre-Simon-Laplace (IPSL). It is also used to drive the offline model CAMS_LMDz, in which case its horizontal winds are nudged to those of the ERA5 reanalysis [wind fields \(Hersbach et al., 2020\)](#). From the computer code of LMDz, CAMS-LMDz only keeps the transport subroutines for advection (Hourdin & Armengaud, 1999), deep convection (Emanuel, 1991), thermals (Rio & Hourdin, 2008), and

boundary-layer turbulence (Hourdin et al., 2006). All other processes are replaced by an archive of relevant meteorological variables (air mass fluxes, exchange coefficients, temperature, etc.) built with the full LMDz model at the target spatial resolution, thereby allowing relatively small computing time and resources for the offline model. LMDz ensures the physical consistency of the archive of meteorological variables. The meteorological variables are stored as 3-hourly averages. CAMS_LMDZ has been regularly participating in OCO-2 MIP (Byrne et al., 2023) and TransCom intercomparison studies.

2.4.3 CTE_TM5

TM5 is a tracer transport model used for simulating atmospheric trace gas chemistry and transport (Krol et al., 2005). We refer to it as CTE_TM5 because the model was run with the CarbonTracker-Europe (CTE) shell, but this does not alter the TM5 physics and chemistry. TM5 advection is computed using the slopes advection scheme (Russell & Lerner, 1981) and in this work it is driven by ERA-5 reanalysis wind fields, making it an offline model. The convection is computed from the convective entrainment and detrainment fluxes from the ERA-5 reanalysis. Free tropospheric diffusion is computed using the formulation by Louis (1979). Diffusion in the boundary layer is computed using the parametrization by Holtslag & Boville (1993), where the diurnal variability in the boundary layer height is computed using Vogelesang and Holtslag (1996). TM5 is widely used in inversions and regularly participates in MIPs, for different tracers at different model resolutions and driven with different wind reanalysis products (for example, Byrne et al., 2023; Friedlingstein et al., 2025; Gaubert et al., 2019; Krol et al., 2018).

2.4.4 TM3

TM3 (Heimann and Körner, 2003) is an offline atmospheric tracer transport model, in the present runs driven by meteorological fields from the NCEP reanalysis (Kalnay et al., 1996). It was run here on a spatial resolution of 5 degrees longitude, about 3.8 degrees latitude, and 19 vertical layers. The advection uses the slopes scheme (Russell and Lerner, 1981), which is the same as in TM5. Boundary layer mixing is parameterized according to Louis (1979). Vertical mixing due to sub-grid-scale cumulus clouds is calculated using the mass flux scheme of Tiedke (1989). TM3 is the ATM used in Jena APO inversion (Rödenbeck et al., 2008), which is one of the flux products used in this study.

296 2.4.5 MIROC4-ACTM

297 MIROC4-ACTM is a new generation Model for Interdisciplinary Research on Climate (MIROC,
298 version 4.0; Watanabe et al., 2008) atmospheric general circulation model (AGCM)-based
299 chemistry-transport model (ACTM; Patra et al., 2018) . This AGCM is evolved from the Center
300 for Climate System Research, University of Tokyo (CCSR) / National Institute for
301 Environmental Studies (NIES) / Frontier Research Center for Global Change, JAMSTEC
302 (FRCGC) AGCM version 5.7b (Numaguti et al., 1997). The MIROC4 AGCM propagates only
303 explicitly resolved gravity waves into the stratosphere through the implementation of a hybrid
304 vertical coordinate system compared to its predecessor AGCM5.7b. The MIROC4 AGCM
305 online-simulated horizontal winds and temperature are nudged to the Japanese 55-year
306 Reanalysis (JRA-55) at 6-hourly time intervals (Kobayashi et al., 2015). MIROC4-ACTM
307 produces “age-of-air” up to about 5 years in the tropical upper stratosphere (~ 1 hPa) and about 6
308 years in the polar middle stratosphere (~ 10 hPa), in agreement with observational estimates. The
309 convective transport and inter-hemispheric transport of tracers in the model are validated using
310 ²²²Radon and sulphur hexafluoride (SF₆), respectively (Patra et al., 2018).

311 2.4.6 NICAM-TM_gl5 and NICAM-TM_gl6

312 NICAM-TM is an atmospheric transport model based on the Nonhydrostatic Icosahedral
313 Atmospheric Model (NICAM) (Niwa et al., 2011; Satoh et al., 2014). In this study, we used the
314 offline mode of NICAM-TM, which uses air mass fluxes, vertical diffusion coefficients and
315 other meteorological variables; those data are calculated in advance by an online calculation of
316 NICAM, in which horizontal winds are nudged toward the JRA-55 data. In NICAM, the air mass
317 fluxes are calculated consistently with the continuity equation while conserving tracer masses,
318 which do not require any numerical mass fixing (Niwa et al., 2011). For APO-MIP1, two
319 horizontal resolutions were used: “glevel-5” (gl5) and “glevel-6” (gl6), whose mean grid
320 intervals are 223 and 112 km, respectively. The number of the vertical model layers is 40 and the
321 top of the model domain is at approximately 45 km. The vertical diffusion coefficients are
322 calculated with the MYNN (Mellor and Yamada, 1974; Nakanishi and Niino, 2004) Level 2
323 scheme (Noda et al., 2010). The cumulus parameterization scheme used in NICAM-TM is

Chikira & Sugiyama (2010). Model performance for atmospheric constituent transport can be found in Niwa et al. (2011, 2012).

2.4.7 NIES

NIES-TM-FLEXPART is a coupled transport model combining Eulerian (NIES-TM) and Lagrangian (FLEXPART) models. It is a transport modeling component of the variational flux inverse modeling system NIES-TM-FLEXPART-Variational (NTFVAR, Maksyutov et al., 2021). The NIES Transport Model (NIES-TM) is an offline model, originally developed in the 1990s (Maksyutov et al., 2008). In this study, the NIES-TM v.21 is used, which improves SF₆ transport and tropopause height over the former v.08.1 (Belikov et al., 2013), as evaluated in Krol et al. (2018), due to (a) using ERA5 hourly wind data, including vertical wind on model coordinates, on 137 model levels and a 0.625° grid for preparation of the 4-hourly average mass fluxes on 42 hybrid-pressure levels, (b) transporting first-order moments (Russell & Lerner, 1981; Van Leer, 1977) for advection, (c) applying penetrative convection rate and turbulent diffusivity supplied by the ERA5 reanalysis (Hersbach et al., 2020). The version v.21 is the same as used in the OCO-2 MIP (Byrne et al., 2023). NIES-TM is coupled with the Lagrangian model FLEXPART (Stohl et al., 2005) to provide refinement to the near field transport during the last 3 days prior to the observation event as presented by (Belikov et al., 2016). FLEXPART model v.8.0 is driven by 6-hourly JRA-55 winds, interpolated to 40 hybrid pressure levels and 1.25°x1.25° resolution. The surface flux footprints are produced by FLEXPART at 1°x1° resolution and daily time step.

Table 1. Participating ATMs and model parameters.

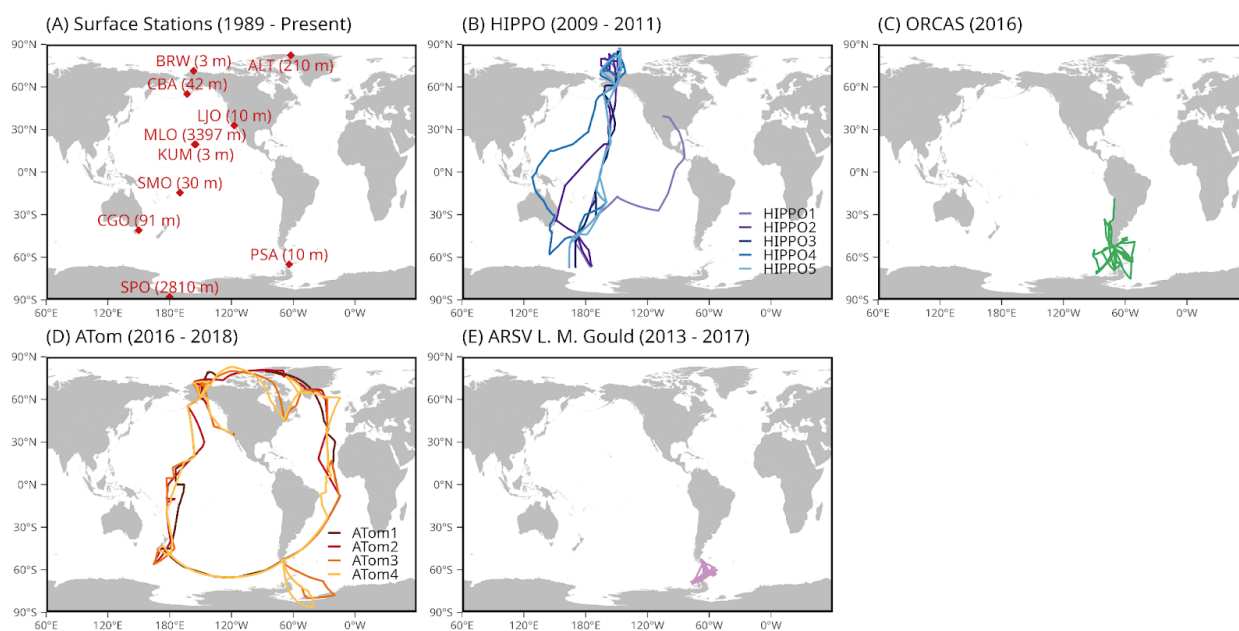
Abbreviation	Model System	Grid (latitude × longitude × levels)	Meteorology	Run start, valid period	Reference(s)
CAM-SD	Community Atmospheric Model	0.9° × 1.25° × 56	MERRA-2	1986, 1989-2019	Danabasoglu et al., 2020
CAMS_LMDZ	Copernicus	1.875° × 3.75° × 39	ERA5	1986,	Chevallier, 2013;

	Atmosphere Monitoring Service			1991-2020	Chevallier et al., 2005, 2010
CTE_TM5	CarbonTracker Europe	$1^{\circ} \times 1^{\circ} \times 25$	ERA5	2000, 2003-2020	Luijkx et al., 2017
Jena_TM3	TM3	$4^{\circ} \times 5^{\circ} \times 19$	NCEP	1986, 1989-2020	Heimann & Körner, 2003
MIROC4- ACTM	MIROC4- ACTM	$2.8^{\circ} \times 2.8^{\circ} \times 67$	JRA-55	1986, 1991-2020	Chandra et al., 2022; Patra et al., 2018
NICAM- TM_g15	NICAM-based Transport Model	$\sim 223 \text{ km} \times 40$	JRA-55	1986, 1989-2020	Niwa et al., 2011, 2017
NICAM- TM_g16		$\sim 112 \text{ km} \times 40$			
NIES	NIES-TM- FLEXPART	$3.75^{\circ} \times 3.75^{\circ} \times 42$ (NIES-TM); $1^{\circ} \times 1^{\circ} \times$ 40 (FLEXPART)	JRA-55	2000, 2003-2020	Belikov et al., 2016; Maksyutov et al., 2021

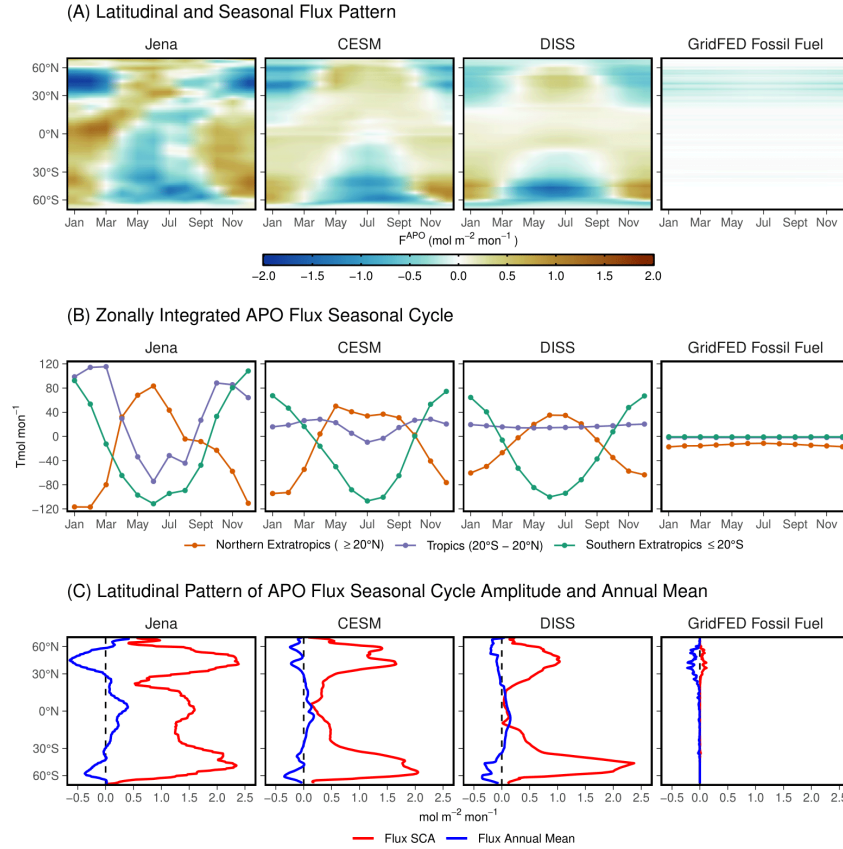
344 2.5 Outputs from transport models

345 For each ATM, we required simulations for all species sampled to match with the observation
346 locations and times in a subset of the full ObsPack CO₂ files GLOBALVIEWplus v7.0 ObsPack
347 (Schuldt et al., 2021), excluding the model spin-up period. This subset corresponds to existing
348 APO observations that are analyzed in this study from Scripps O₂ Program surface stations, NSF
349 NCAR airborne observations, and NSF NCAR and AIST/JMA shipboard programs. The full list
350 of these records is in Table S1. We note that, while the HIPPO, ORCAS, ATom, and Gould
351 ObsPack files contain CO₂ observations from different instruments, their 10-sec sampling times
352 align with the NSF NCAR APO measurements, except during calibration periods for either
353 instrument.

354 We also received optional output, which includes the full set of ObsPack files, 3-D atmospheric
 355 fields, meteorological variables, additional ship data, and output at additional fixed sites (Table
 356 S2). Further details are provided in the APO-MIP1 protocol available at Stephens et al. (2025).
 357 We obtained output matching the full set of ObsPack files from four ATMs, which will be useful
 358 for future network design. We obtained daily mean 3-D gridded concentration fields from six
 359 ATMs. These fields support the calculation of diabatic mixing rates, which we use to evaluate
 360 ATMs and the flux products, following the method of Jin et al. (2024). Details are in Section 3.2.
 361 We also received hourly (from two versions of NICAM) or 3-hourly (from NIES) output for an
 362 extensive list of sites with past or ongoing APO measurements, and co-located samples for ship
 363 sampling programs of NIES VOS, AIST R/V Mirai, and UEA Cap San Lorenzo (Hamburg Süd)
 364 from three models. These data are not analyzed in this study, but are made available at Stephens
 365 et al. (2025).



367 Figure 1: Geographic distribution of APO observations used in this study: (A) Scripps O₂
 368 Program surface stations (red diamonds) with station codes and inlet elevation in meters above
 369 sea level; (B) HIPPO (1 to 5) airborne campaign horizontal flight tracks covering the Pacific
 370 Ocean; (C) ORCAS aircraft measurements concentrated in the Drake passage; (D) ATom (1 to 4)
 371 airborne campaign horizontal flight tracks covering the Pacific and Atlantic Oceans; and (E)
 372 Ship-based measurements from the RV *Laurence M. Gould* operating in the Drake passage.



373

374 Figure 2: Comparison of APO flux patterns from the three air-sea flux products (Jena, CESM,
 375 and DISS) and fossil fuel emissions (GridFed), averaged from 2009 to 2018. (a) Hovmöller
 376 diagrams showing the spatiotemporal distribution of APO fluxes ($\text{mol m}^{-2} \text{mon}^{-1}$) as a function of
 377 latitude and month. (b) Seasonal cycles of zonally integrated fluxes for three latitude bands:
 378 Northern Extratropics ($\geq 20^\circ\text{N}$, orange), Tropics ($20^\circ\text{S}-20^\circ\text{N}$, lavender), and Southern
 379 Extratropics ($< 20^\circ\text{S}$, green). (c) Latitudinal profiles of flux seasonal cycle amplitude (SCA, red)
 380 and annual mean flux (blue). For the annual mean profiles (blue lines in panel C), only the
 381 latitudinal gradients should be interpreted, as the global means may contain biases in the ocean
 382 flux products, which are not the focus of this paper.

383 3. Results and discussion

384 3.1 APO model-observation comparisons at surface stations and along aircraft 385 flight tracks

386 3.1.1 APO seasonal and latitudinal variations at surface stations

387 We show observations and model simulations of APO seasonal cycles at 10 surface stations of
388 the Scripps O₂ program network in Fig. 3. We present annual mean values, seasonal cycle
389 amplitudes (SCA), and phase from both observations and model simulations at these surface
390 stations in Fig. 4, with model-observation differences shown as colors. Observations show
391 clear meridional gradients in APO annual means (Fig. 5A), with higher values in the Southern
392 Hemisphere than Northern Hemisphere, and a southern tropical “bulge” evident at SMO and in
393 the airborne data centered on 15°S. ~~Observations show clear meridional gradients in APO annual
394 means (Fig. 54A), with higher values in the Southern Hemisphere than Northern Hemisphere,
395 and a southern tropical “bulge” evident at SMO and in airborne data (Battle et al., 2006; Gruber
396 et al., 2001; Stephens et al., 1998).~~ The APO SCA shows higher values in the high latitudes of
397 both hemispheres, with larger amplitudes in the Southern Hemisphere compared to the Northern
398 Hemisphere, yet reaches its maximum at the northern mid-latitude station Cold Bay (CBA) (Fig.
399 4B). The seasonal phase exhibits an approximately 6-month difference between hemispheres,
400 while remaining relatively uniform within each hemisphere (Fig. 4C).

401 The higher annual mean APO in the Southern Hemisphere and the southern tropical “bulge” is a
402 result of southward O₂ and CO₂ transport by the oceans, further amplified by net APO uptake in
403 the Northern Hemisphere from fossil fuel burning (Keeling & Manning, 2014; Stephens et al.,
404 1998). The larger APO SCA in mid- to high-latitudes reflects more pronounced seasonal flux
405 cycles resulting from larger marine net primary production (NPP) and sea surface temperature
406 changes in these regions. The thermal and biological effects on APO SCA are further enhanced
407 at eastern Pacific coastal sites (e.g., LJO and CBA), where the shallow marine boundary layer
408 traps high-APO air masses during summer. The 180-days phase difference between the two
409 hemispheres is a result of different seasonal heating and cooling, as well as the biological cycle.

410 3.1.2 Biases in APO-MIP1 simulations at surface stations

411 APO-MIP1 simulations of APO annual means and seasonal cycles at surface stations broadly
412 agree with observations (Figs. 3-4). Simulations driven by CESM fluxes show the best
413 agreement with observed APO features. For annual mean spatial patterns (Fig. 4A), CESM- and
414 DISS-driven simulations show comparable performance in representing the southern tropical
415 “bulge” and north-south gradient in annual means, while significantly outperforming simulations
416 using the Jena flux model in northern stations. The main limitation of simulations using CESM
417 fluxes is an overestimation of annual mean APO values across Pacific sites in the Southern
418 Hemisphere, and an underestimation at LJO. Simulations using DISS fluxes also underestimate
419 the annual mean APO at LJO.

420 APO SCA is well represented in simulations driven by CESM flux, but the SCA at LJO is
421 significantly underestimated in all ATMs except CAM-SD. The underestimation is caused by an
422 overly weak summer-time APO peak (Fig. 3), which also leads to the small annual mean
423 presented above. Simulations using DISS flux generally underestimate SCA, especially in the
424 high latitudes. Simulations using Jena flux, however, generally overestimate the SCA in the mid-
425 to high-latitudes. We find largest SCA biases and cross-ATMs spread at LJO and CBA when
426 using the Jena flux. The biases and model spread are closely related to underrepresentation in
427 ATMs, and will be discussed in the next section. We note that the model biases and spread
428 observed at surface stations are smaller than those reported in the previous TransCom-O₂
429 experiment (Blaine, 2005), indicating improved atmospheric transport modeling.

430 Phase simulations using CESM flux are consistent with observations at most stations, except at
431 two northern low-latitude stations, KUM and MLO, where we find too late seasonal minimum
432 day by up to two weeks. Simulations using DISS flux show even larger biases, with earlier
433 seasonal minimum days at all southern and northern low-latitude stations.

434 3.1.3 Impact of ATM mixing biases

435 We find APO-MIP1 simulations have large model spread and biases at two northern
436 mid-latitudes stations, LJO and CBA (Fig. 3), especially simulations using Jena fluxes. We note
437 that the interdependence of transport models and fluxes in inversions can be seen for the Jena

438 flux product simulations at LJO (Figs. 3-4). As expected, we see good agreement with
439 observations for the Jena flux product transported by the same model used in the Jena APO
440 inversion (Jena_TM3). However, all other ATMs overestimate summertime APO, and
441 consequently SCA, for the Jena flux product at LJO, CBA, and BRW. All other ATMs also
442 simulate too negative wintertime APO at LJO. These biases suggest a stronger regional APO
443 source in the Jena flux product that could have resulted from too rapid dilution of surface flux
444 signals at LJO in both summer and winter.

445 Surface station simulations using CESM flux (Figs. 3-4) also reveal elevated model spread and
446 observation deviations at LJO and CBA. At LJO, all ATMs underestimate summertime APO, and
447 consequently SCA, implying too weak upwind outgassing fluxes. The relative magnitude of
448 simulated summer-time peaks for CESM at LJO and CBA maintains a consistent pattern across
449 different flux products, with CAM-SD consistently showing the highest values and Jena_TM3
450 the lowest, regardless of the flux product used, suggesting consistent biases in the ATMs.

451 This substantial cross-ATMs variability highlights the challenges in accurately representing
452 complex atmospheric vertical transport processes in regions where strong temperature inversions
453 and stratocumulus clouds significantly influence vertical mixing (Naegler et al., 2007; Nevison et
454 al., 2008). The Jena flux product, derived from an inversion that assimilates these station data,
455 relies on the TM3 tracer transport model (Rödenbeck et al., 2008). Previous studies indicate that
456 TM3 consistently overestimates vertical mixing over the Eastern Pacific, leading to larger
457 inverted seasonal fluxes to match station observations (Jin et al., 2023; Naegler et al., 2007). Our
458 analysis suggests that in comparison to Jena_TM3, vertical mixing is weaker in the two versions
459 of NICAM, CAM-SD, MIROC4-ACTM, and CTE_TM5, which show larger summer-time APO
460 anomalies at LJO and CBA. This pattern is consistent across the three flux products considered.

461 The larger model spread at northern coastal sites (e.g., LJO, CBA, and BRW) also highlights the
462 limitations of current coarse-resolution ATMs in representing horizontal coastal flows and
463 land-sea breezes. At LJO, samples are collected only during steady west wind (from the ocean)
464 conditions (Keeling et al., 1998). However, ATMs failed to capture the actual small-scale
465 atmospheric conditions associated with on-shore winds during episodic storm systems, which
466 leads to significant underestimation of oceanic influence (Keeling et al., 1998). APO, as a tracer

467 of air-sea gas exchange, is particularly sensitive to the dilution effects in coarse-resolution
468 models.

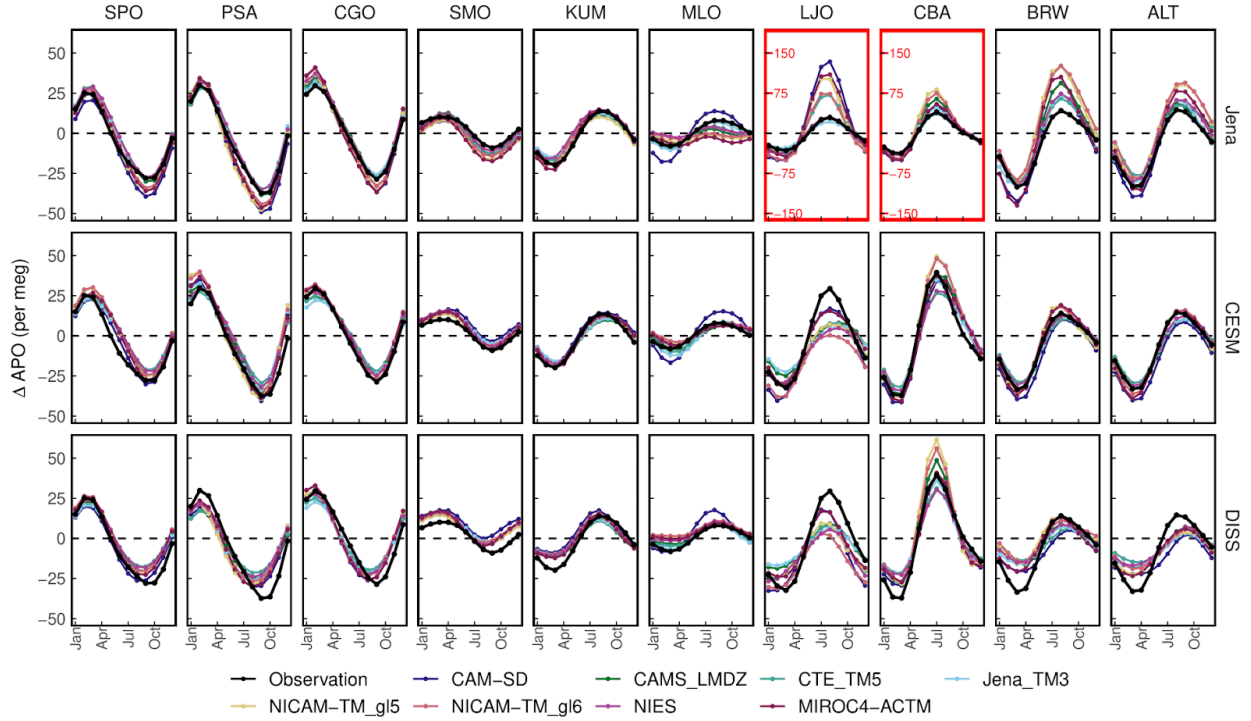
469 **3.1.4 APO seasonal and latitudinal variations along flight tracks and biases in APO-MIP1**

470 We present zonal averages of APO annual means, SCA, and seasonal minimum days derived
471 from airborne data, grouped into 10-degree latitude and 100-mbar bands in Fig. 5A-C (full
472 seasonal cycles in Fig. S1). We further calculate these three metrics as column-average (black)
473 and at 900-mbar (blue) in Fig. 5D-F, where we also compare them with surface station data
474 (shown as red points). The airborne data show patterns similar to those seen at surface stations
475 but provide detailed vertical structures. The vertical profiles consistently show larger SCA at low
476 altitudes, indicating that the main drivers of SCA are near the surface, while annual means and
477 seasonal phases remain uniform across altitudes. Airborne column averages show increasing
478 SCA and decreasing annual means from low to high latitudes, with similar SCA and annual
479 mean values north of 50°N (Fig. 5D-E), whereas station observations show peaks in the
480 mid-latitudes (LJO and CBA) due to high-APO air masses being trapped below the summer
481 marine boundary layer. This trapping effect is also evident in airborne data interpolated to
482 900-mbar.

483 We also calculate APO annual means, SCA, and phases using aircraft simulations from
484 APO-MIP1 (full seasonal cycles in Fig. S1) and compare simulated and observed column
485 averages (1000-400 mbar average) in Fig. 6, with biases in column averages and vertical profiles
486 shown in Figs. S2 and S3-5, respectively. Airborne observation-model comparisons complement
487 those using surface station data. We find similar model biases to those seen in surface data, for
488 example, larger SCA at northern high latitudes with the Jena flux product and smaller SCA at
489 high latitudes with the DISS flux product. The airborne data also reveal three key biases that are
490 not resolved at surface stations. Observations suggest a consistent near-zero annual mean APO in
491 the Southern Hemisphere (south of 30°S), with a spike between 40° and 50°S. However, all three
492 flux products show gradually decreasing annual mean APO south of 30°S, with CESM and DISS
493 flux products showing a smaller spike in magnitude between 40° and 50°S. Simulations using
494 CESM and DISS flux products show **larger annual mean values** ~~a larger SCA~~ in the northern
495 mid-latitudes (40 - 60°N). Additionally, simulations using the Jena flux product in the low

496 northern latitudes show a seasonal minimum day similar to the Southern Hemisphere phase. This
497 bias is caused by low-latitude flux features in the Jena inversion that largely replicate the
498 Southern Hemisphere cycle, likely due to limited observational constraints in this region (Jin et
499 al., 2023).

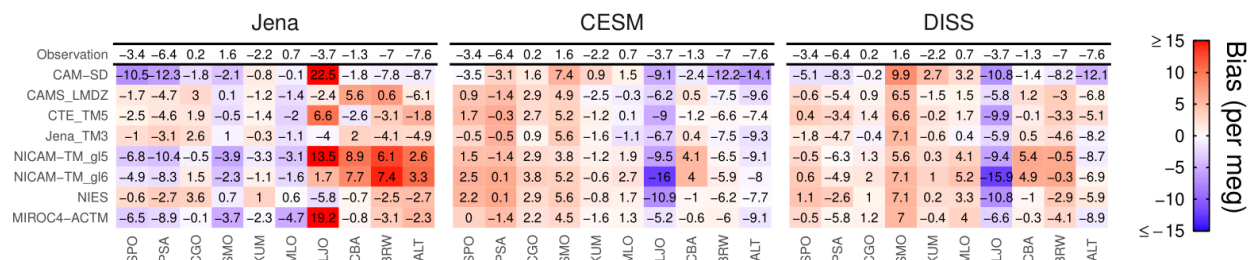
500 Our analysis demonstrates that global airborne measurements provide distinct advantages over
501 station data for evaluating large-scale flux patterns due to the reduced sensitivity of column
502 averages to boundary-layer ATM transport uncertainties. While surface stations show substantial
503 cross-model spread in simulated APO (Figs. 3-4), column-averaged airborne simulations (Fig. 6)
504 reveal remarkable consistency across ATMs when driven by the same flux product. This
505 consistency suggests that column-averaged measurements effectively integrate over local
506 transport features that often dominate surface observations. Here we establish CESM as the most
507 realistic flux product among the three products. The better agreement between observations and
508 CESM-driven simulations provides a more reliable baseline for isolating and quantifying
509 transport-related discrepancies in individual ATMs.



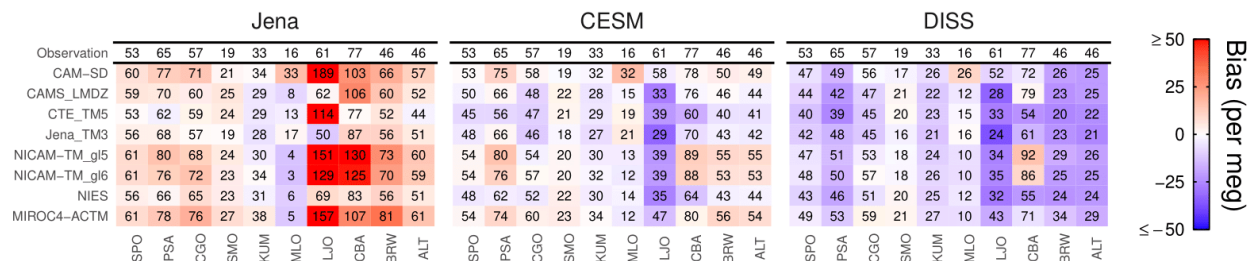
510

511 Figure 3: Comparison of simulated and observed APO seasonal cycles at 10 surface stations
 512 (Fig. 1A), organized from southern high-latitudes (left) to northern high-latitudes (right). In each
 513 panel, the black line represents observations, while colored lines show simulations from different
 514 transport models. Each row of panels corresponds to the three different flux products (Jena,
 515 CESM, and DISS). In each panel, the y-axis shows APO anomalies in per meg units, and the
 516 x-axis shows months from January to December. We note that, for LJO and CBA simulations
 517 using the Jena fluxes, a different y-axis range (three times larger) is used compared to the other
 518 panels. Observations and model simulations at each station are first detrended using a
 519 multiple-station weighted average trend. We calculate monthly mean seasonal APO from 2009 to
 520 2018 for both observations and model simulations.

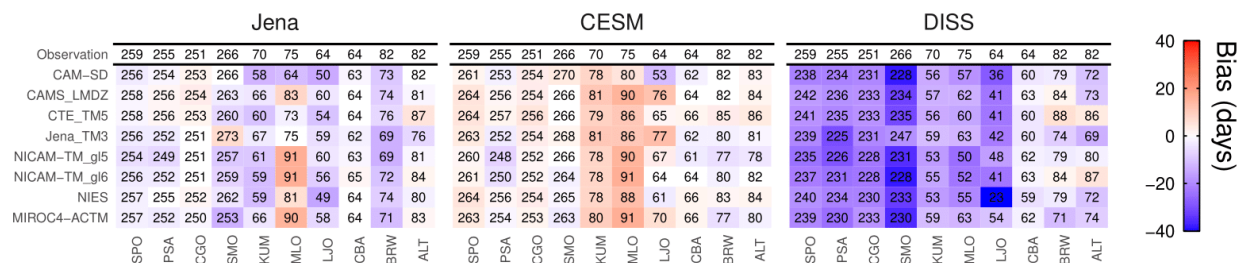
(A) APO Annual Mean (per meg)



(B) APO Seasonal Cycle Amplitude (per meg)



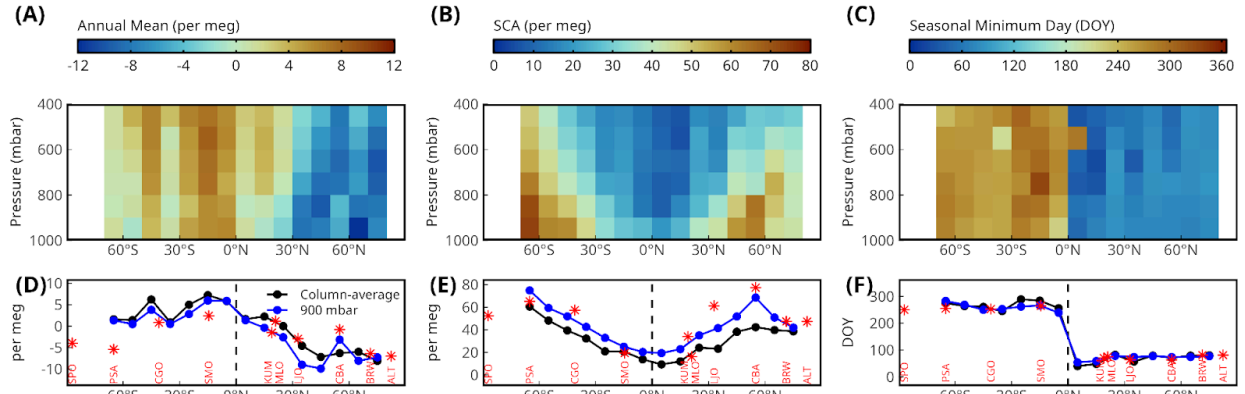
(C) APO Seasonal Minimum Day



521

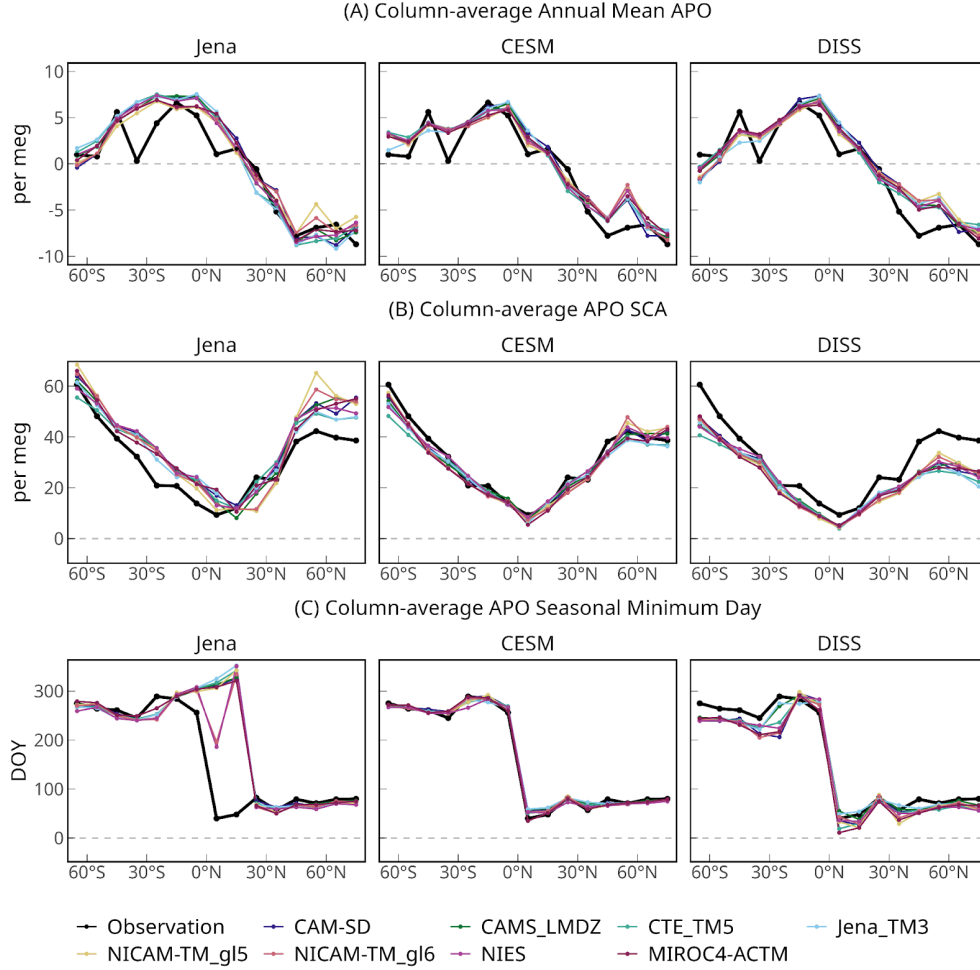
522 Figure 4: Evaluation of APO (A) annual mean relative to a multi-station global mean, (B)
 523 seasonal cycle amplitude, and (C) seasonal minimum day across surface stations using different
 524 flux-transport model combinations. For each panel, results are organized by flux products
 525 (JENA, CESM, DISS) in columns and transport models in rows, with observations on the top.
 526 The metrics are printed in black, with background colors indicating biases relative to
 527 observations. Positive bias is shown in red, and negative bias is shown in blue. Stations from left
 528 to right are organized by latitudes from south to north.

529



530

531 Figure 5: APO annual means (A and D), SCA (B and E), and seasonal minimum day (C and F)
 532 derived from airborne observations. In A-C, we show latitude-pressure distributions, with data
 533 binned into 10 deg latitude by 100-mbar pressure boxes. In D-F, we show 1000-400 mbar
 534 column-averaged (black) and 900-mbar interpolated (blue) values, and also surface station
 535 observations (2009 to 2018). Annual mean is derived from a two-harmonic fit with constant
 536 offset, where the global multi-station trend has been subtracted to detrend the airborne
 537 observations and center the values around zero globally. SCA is calculated as the peak-to-trough
 538 amplitude of the two-harmonic fit, and seasonal minimum day is calculated as the day of
 539 seasonal trough of the two-harmonic fit.



540

541 Figure 6: Comparison of column-average (1000-400 mbar) APO features across latitude from
 542 aircraft observations and model simulations using three different flux products (Jena, CESM, and
 543 DISS). The figure is organized into three sets of panels showing (A) annual mean APO relative
 544 to a multi-station global mean, (B) SCA, and (C) seasonal minimum day. For each feature, we
 545 show latitudinal distributions of observations (black lines) and model simulations (colored lines).
 546 We note that the global mean value has been subtracted from the annual mean values (A) at each
 547 latitude to highlight spatial patterns. We show the column-average (400-1000 mbar) seasonal
 548 cycles of observed and simulated APO for each 10° latitude band in Fig. S1.

549 3.2. Evaluation of diabatic mixing rates diagnosed from transport models

550 In this section, we evaluate the mixing timescale across mid-latitude moist isentropes of each
 551 ATM using the framework developed in Jin et al. (2024). This framework was applied to identify

biases in four ATMs in the mid-latitude Southern Hemisphere using two independent constraints: (1) diagnosed diabatic mixing rates, and (2) cross-isentrope CO_2 gradients. Here we extend the framework to use APO gradients, to include two more reanalysis products, and the analysis in the Northern Hemisphere. We evaluate six of the eight ATMs participating in APO-MIP1 that provide 3-D atmospheric fields (CAM-SD, CTE_TM5, Jena_TM3, NICAM-TM_gl5, NICAM-TM_gl6, and MIROC4-ACTM), which are required to diagnose diabatic mixing rates. Diabatic mixing rates and APO gradients are diagnosed based on the mass-indexed isentropic coordinate M_{θ_e} , which was first introduced by Jin et al. (2021). For each pair of transport models and flux products, we resolve cross- M_{θ_e} diabatic mixing rates and cross- M_{θ_e} APO gradients in the mid-latitudes of both hemispheres. We use observation-based diabatic mixing constraints diagnosed from four meteorological reanalyses, and observed APO gradient constraints calculated from three airborne campaigns. The detailed methodology for calculating M_{θ_e} surfaces, diabatic mixing rates, and cross- M_{θ_e} APO gradients is provided in Appendix C.

We show the climatological monthly mean diabatic mixing rates of two M_{θ_e} surfaces in the Southern Hemisphere in Fig. 7, as well as schematics of the geographic distribution of the two M_{θ_e} surfaces. For each ATM, mixing rates in Fig. 7 are calculated from APO and averaged over three realizations diagnosed from using three flux products. The reanalysis mixing rates are calculated from moist static energy (MSE) budget and shown as average and 1σ spread over the four reanalysis products. The six ATMs and the reanalyses show diabatic mixing rates with clear seasonal cycles, suggesting more rapid mixing across isentropes in the austral winter than summer. ATMs generally overestimate diabatic mixing rates, especially in the summer and winter, when there are large cross- M_{θ_e} APO gradients that lead to well-defined mixing rates. Among the six ATMs, CTE_TM5 and Jena_TM3 show too rapid mixing that is biased high in all seasons. The other four ATMs align better with reanalysis, but still show significant overestimation for most of the year. MIROC4-ACTM shows the best performance. These findings align with Jin et al. (2024), which previously identified that the southern hemisphere summer-time mixing rates are overestimated in ATMs used for CO_2 inversions, with consistent results for the three ATMs (MIROC4-ACTM, Jena_TM3, and CTE_TM5) being used in both studies.

581 We find that biases in diagnosed diabatic mixing rates correlate with biases in cross- M_{θ_e} APO
 582 gradients in each season, with stronger diabatic mixing leading to smaller APO gradients (Fig.
 583 8). Fig. 8 shows the ATM-diagnosed diabatic mixing rates and simulated APO gradients (points)
 584 across six transport models and three flux products at two M_{θ_e} surfaces (30 and 45×10^{16} kg M_{θ_e})
 585 for three selected 2-month periods in the Southern Hemisphere. The points suggest clear linear
 586 relationships between diagnosed mixing rates and simulated APO gradients for each flux product
 587 (shown as fit lines for each flux product). The linear relationships persist across all seasons and
 588 M_{θ_e} surfaces, though with varying slopes depending on the underlying fluxes (Fig. 8). ATMs
 589 generally underestimate cross- M_{θ_e} absolute APO gradients (i.e., a closer to zero gradient) at both
 590 M_{θ_e} surfaces, corresponding to the overestimation of diabatic mixing rates in these models. For
 591 each flux product, biases in cross- M_{θ_e} APO gradients are always larger in fast mixing ATMs
 592 (e.g., Jena_TM3 and CTE_TM5) compared to slow mixing ATMs (e.g., two versions of
 593 NICAM-TM, MIROC4-ACTM, and CAM-SD), with MIROC4-ACTM showing the best
 594 agreement. For each transport model, the simulated gradient shows clear spread across different
 595 flux products. The largest spread occurs in austral winter and spring (Fig. 8C-D), when
 596 simulations with the DISS fluxes show much larger gradients compared to CESM or Jena fluxes.
 597 We note that the direct comparison of simulated and observed gradients for individual models is
 598 complicated by the interplay of ATM biases and flux product biases.

599 To evaluate flux products independently of transport model biases, we leverage both diabatic
 600 mixing rates and APO gradients. For each flux product, the intersection between the mixing
 601 rate-gradient linear fit and the MSE-diagnosed mixing rate indicates the expected APO gradient
 602 with realistic mixing characteristics. Therefore, we can evaluate large-scale flux features in the
 603 flux products by comparing this expected gradient to the observed gradient. Our analysis in Fig.
 604 8 suggests that CESM is the most realistic flux product in the mid-latitude Southern Hemisphere
 605 in all seasons. The expected CESM gradients (intersections of thin blue line and vertical gray
 606 band) fall within the observation uncertainty range in all seasons and surfaces except austral
 607 summer at the 30×10^{16} kg M_{θ_e} surface (Fig. 8A), which suggests a slight underestimation of
 608 uptake in the CESM product. The expected gradients of the Jena flux product also generally fall
 609 within the observation uncertainty range, but shows an even larger underestimation in Fig. 8A.
 610 The expected gradients of the DISS flux product have large biases in the mid-latitude Southern
 611 Hemisphere. The expected gradient is significantly larger in the austral winter (Fig. 8C-D), and

significantly smaller at the 30×10^{16} kg M_{0e} surface in austral summer (Fig. 8A) and austral spring (Fig. 8E), suggesting seasonal biases in the flux pattern.

Biases in expected gradients relative to observed gradients result from errors in the magnitude and spatial distribution of air-sea APO flux, specifically the difference in flux magnitudes between regions north and south of the target M_{0e} surface. For instance, a positive expected gradient bias during austral summer at the 30×10^{16} kg M_{0e} surface (Fig. 8A) in the DISS product could stem from underestimated outgassing in high southern latitudes, excessive outgassing in lower latitudes, or both. In addition, a flux product could produce realistic expected gradients despite underestimating absolute fluxes both north and south of the M_{0e} surface if the difference remains correct. Resolving these inherent ambiguities requires additional observational constraints from surface stations, ships, and aircraft, which we addressed in Section 3.1.

While the focus of Jin et al. (2024) was on the mid-latitude Southern Hemisphere, we extend our analysis of the mid-latitude diabatic mixing rates to the Northern Hemisphere at the 45×10^{16} kg M_{0e} surface (Fig. 9). ATMs also generally overestimate diabatic mixing rates in the Northern Hemisphere, except during summer (JJA). Whereas MSE-diagnosed mixing rates peak in northern summer, ATM-diagnosed mixing rates have their seasonal minimum at this time. We note that APO gradients in ATMs are close to zero during JJA, leading to poorly defined diabatic mixing rates. We carry out the same transport model and flux product analyses in the Northern Hemisphere in January to March (Fig. 10A) and August to October (Fig. 10B). MIROC4-ACTM still demonstrates the closest agreement with reanalysis data in both seasons, and CTE_TM5 shows the largest mixing rate bias. We note that TM3 and TM5 are based on similar parameterization schemes, but TM3 outperforms TM5. In both seasons, the expected gradients inferred from CESM flux align with the airborne observations, while Jena and DISS overestimate and underestimate expected gradients, respectively.

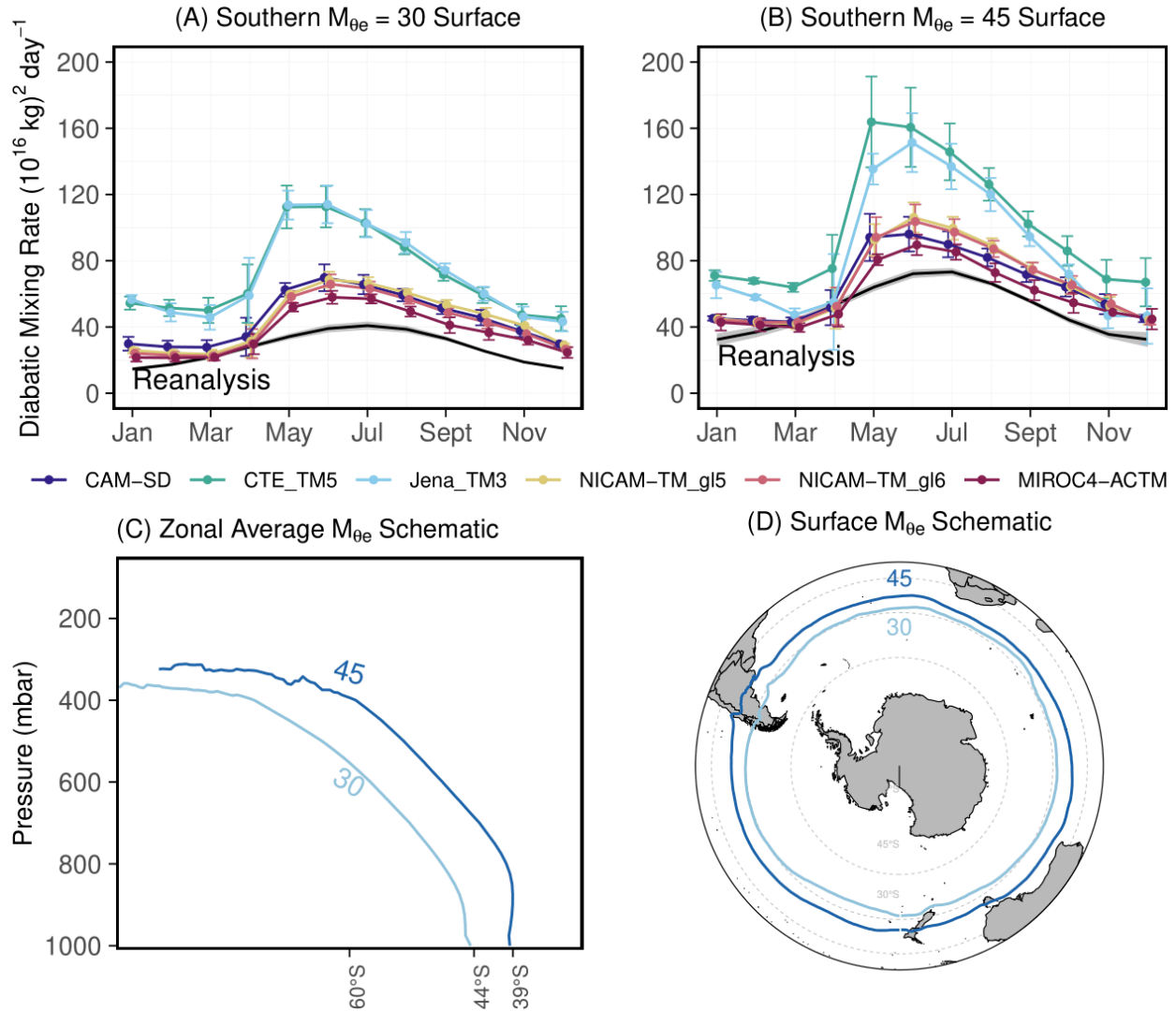
Our attempt to diagnose mixing rates in ATMs in the Northern Hemisphere mid-latitudes using ocean tracers alone is partly limited by the predominantly land surface. We find both summer and winter peaks in seasonal diabatic mixing rates in the northern mid-latitudes, driven by strong convection. Over land, convection peaks in summer due to strong surface heating that creates unstable atmospheric conditions. Over the ocean, however, convection peaks in winter due to larger air-sea temperature differences. Our ATM-diagnosed mixing rates in the Northern

Hemisphere may not capture the summer peak because atmospheric mixing processes over land may not be adequately reflected in transport of air-sea APO flux signals, which occurs initially over the ocean. This limitation is particularly significant in the Northern Hemisphere, where zonal mixing is slower (2-4 weeks) due to topographic blocking and stationary wave patterns. We plan to diagnose the land and ocean contrast in atmospheric diabatic mixing in the next APO-MIP1 by also forward transporting land tracers (e.g., CO₂ sources/sinks from the land biosphere). Our method is more robust in the Southern Hemisphere mid-latitudes due to faster zonal mixing (1-2 weeks) and the predominantly ocean surface. We also note that the distinct thermal capacities of land and ocean in the Northern Hemisphere create more complex surface M_{0e} outcrops with larger latitudinal shifts across seasons (Jin et al., 2021), as shown in Fig. 9C. We, however, account for these shifts in our analysis.

Our analysis reveals that the ATM-diagnosed diabatic mixing rate primarily reflects an intrinsic characteristic of the transport model, at least in the Southern Hemisphere, showing little sensitivity to the underlying flux pattern, tracers, and land-ocean differences, particularly in models with smaller mixing rates (i.e., two versions of NICAM-TM, MIROC4-ACTM, and CAM-SD). These four models demonstrate consistent mixing rates across different flux products (Figs. 8 and 10). This consistency is further supported by our analysis of diagnosed mixing rates for individual APO components (ΔO_2^{ocn} , ΔN_2^{ocn} , ΔCO_2^{ocn} , ΔO_2^{ff} , and ΔCO_2^{ff}) transported by ATMs with smaller mixing rates, which yields similar mixing rates despite these tracers having distinct signs, seasonal patterns, and magnitudes (Fig. S6). However, ATMs with faster mixing rate (e.g., Jena_TM3 and CTE_TM5) show large variability both across flux products (Fig. 9-10) and across tracers (Fig. S6). Notably, these two models exhibit approximately 50% slower diagnosed mixing rates for the fossil fuel CO₂ tracer (ΔCO_2^{ff}) compared to the other ocean flux tracers in the austral summer at the 30×10^{16} kg M_{0e} surface. We note that the fossil fuel CO₂ tracer has its main source in the Northern Hemisphere, and its mixing at the mid-latitude Southern Hemisphere preferentially occurs in the upper troposphere. In contrast, the air-sea flux tracers have significant sources/sinks over the Southern Ocean with rapid cross-isentrope mixing preferentially in the lower troposphere. This behavior suggests that these models simulate distinctly different mixing patterns between the planetary boundary layer (0-2 km) and the free troposphere. Specifically, these models appear to have excessive vertical mixing in the boundary

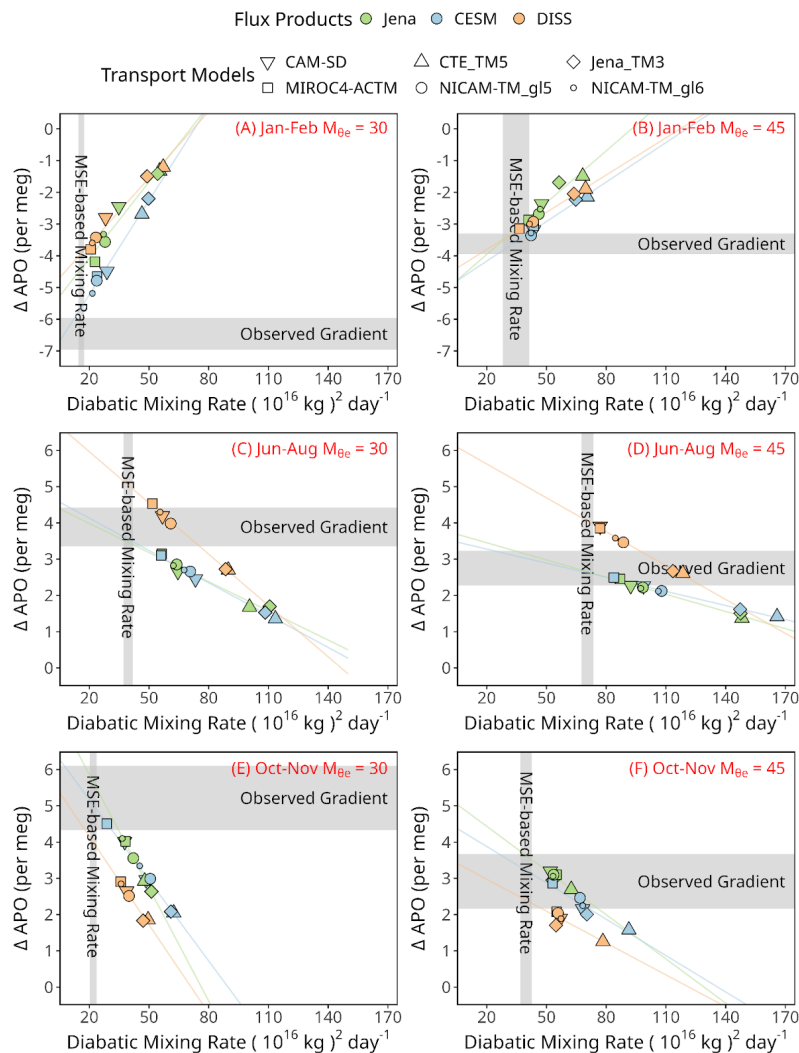
672 layer while maintaining more realistic transport in the free troposphere. Our method, however,
673 assumes a constant cross- M_{θ_e} diabatic mixing rate over the entire M_{θ_e} surface. The excessive
674 boundary layer mixing causes the diagnosed mixing rates in these models to be overly sensitive
675 to the specific vertical distribution of air-sea APO flux components.

676 Our evaluation of ATMs using simulations from APO-MIP1 advances the original framework of
677 Jin et al. (2024) in ~~two~~^{three} key aspects. First, we expand the experimental design by increasing
678 the number of participating ATMs to six and employing three different flux fields with each
679 ATM, generating 18 model realizations. This comprehensive matrix of simulations enables a
680 more systematic evaluation of both transport and flux-related biases. We demonstrate how
681 atmospheric tracer observations can be leveraged to independently evaluate and distinguish
682 between biases in surface fluxes and atmospheric transport models. Second, we enhance the
683 robustness of our MSE-diagnosed mixing rate calculations by incorporating two additional
684 reanalysis products and computing mixing rates at the native high resolution of each reanalysis,
685 rather than averaging to a coarser grid before the calculation. One limitation in our method is that
686 we only use M_{θ_e} calculated from MERRA-2 for each of the transport models rather than using
687 M_{θ_e} calculated from the individual transport model, which in principle can be done by
688 interpolating the temperature and humidity from parent reanalysis to the ATM grid. This
689 limitation would lead to slight inconsistency between the actual M_{θ_e} in the model and the value
690 we assigned to it. However, the differences between M_{θ_e} calculated from different reanalyses
691 remain small and our method ensures consistency in geography of each M_{θ_e} surface (Jin et al.,
692 2021).



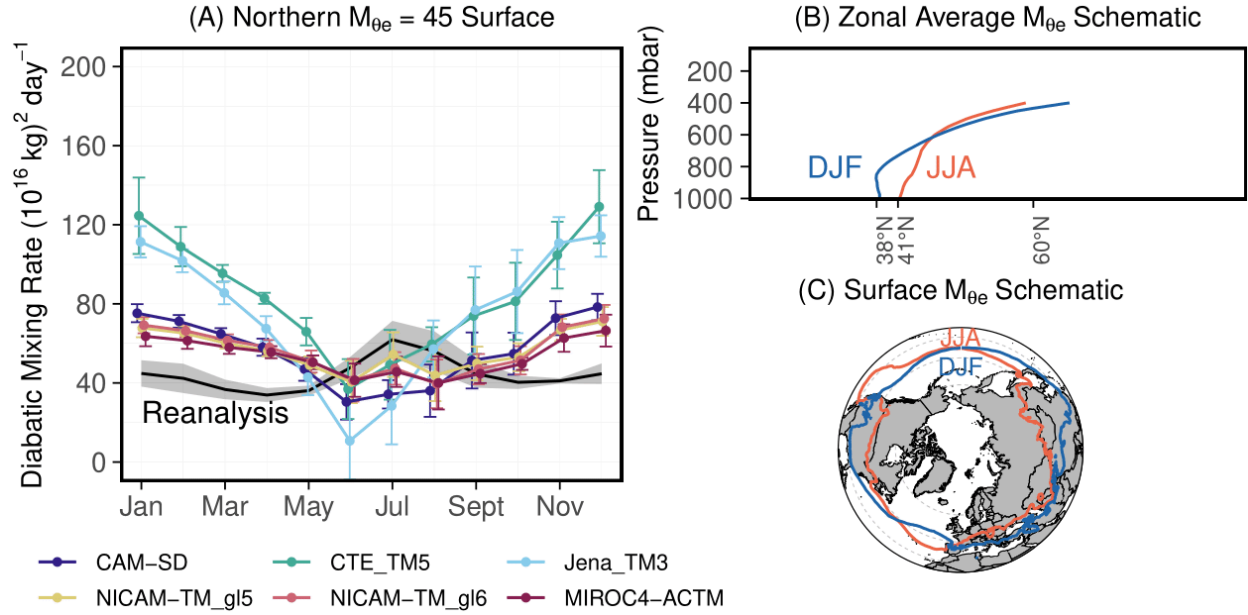
693

694 Figure 7: Climatological monthly diabatic mixing rates across the (A) 30 and (B) 45 (10^{16} kg)
 695 $M_{\theta e}$ surfaces in the Southern Hemisphere. ATM-diagnosed mixing rates are derived from six
 696 ATMs in APO-MIP1 that provide 3-D APO fields. Error bars represent the 1σ spread across the
 697 30 and $45 \times 10^{16} \text{ kg } M_{\theta e}$ of three flux products used here. Black lines represent MSE-diagnosed
 698 mixing rates as the average of four reanalysis MSE budgets, while the gray shaded regions
 699 represent the 1-sigma spread. (C) Schematic showing latitude-pressure distribution of
 700 troposphere zonal annual average $M_{\theta e}$, and (D) annual average near-surface $M_{\theta e}$ contours of the
 701 30 and 45 (10^{16} kg) surfaces, computed from MERRA-2 reanalysis for the year 2009. These two
 702 $M_{\theta e}$ surfaces have very small seasonal meridional variability.



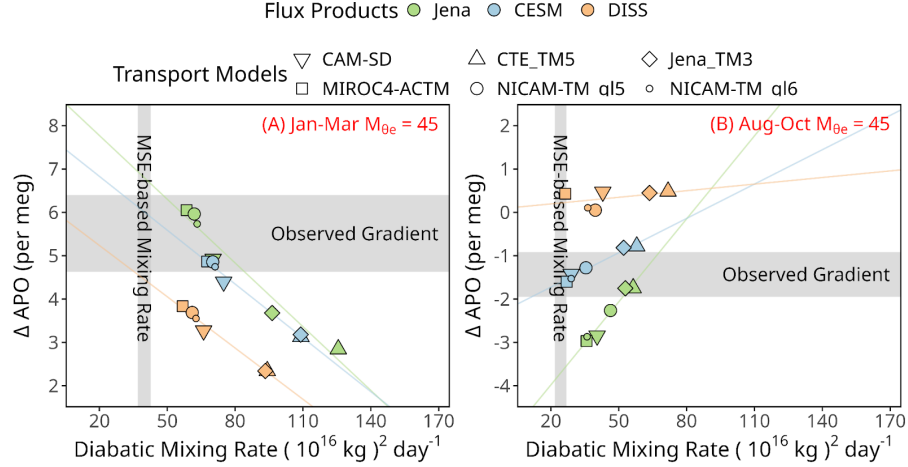
703

704 Figure 8: Using MSE-based diabatic mixing rates and airborne observations of cross-isentrope
 705 APO gradients to evaluate ATMs and flux models. Each panel compares model-diagnosed
 706 diabatic mixing rates (x-axis) and cross- M_{θ_e} APO gradients (y-axis) at the 30×10^{16} kg M_{θ_e}
 707 surface (A, C, E, $\sim 44^\circ\text{S}$ surface outcrop) and at 45×10^{16} kg M_{θ_e} (B, D, F, $\sim 39^\circ\text{S}$ surface
 708 outcrop). Results are shown for three seasonal periods: Jan-Feb (A-B), Jun-Aug (C-D), and
 709 Oct-Nov (E-F) based on available airborne campaigns. Points represent individual model
 710 simulations, with colors indicating flux products (Jena, CESM, DISS) and symbols denoting
 711 different ATMs. Vertical gray bands show the 1σ range of MSE-based mixing rates derived from
 712 four reanalysis products. Horizontal gray bands indicate the 1σ range of observed APO gradients
 713 after spatial and temporal bias correction. Colored lines show linear fits of mixing rates and APO
 714 gradients for each flux product across different transport models.



715

716 Figure 9: (A) Similar to Fig. 7, but showing climatological monthly diabatic mixing rates across
 717 the $45 (10^{16} \text{ kg}) M_{\theta_e}$ surface in the Northern Hemisphere. We note that JJA diabatic mixing rates
 718 in ATMs are poorly constrained due to close-to-zero cross- M_{θ_e} APO gradients. (B)
 719 Latitude-pressure distribution of zonal average $45 \times 10^{16} \text{ kg } M_{\theta_e}$ surfaces during boreal summer
 720 (JJA) and winter (DJF). The two M_{θ_e} surfaces end at the tropopause, which is higher in the
 721 summer in the mid-latitudes. (C) Corresponding Earth surface outcrops of the JJA and DJF $45 \times$
 722 $10^{16} \text{ kg } M_{\theta_e}$ surfaces. Unlike in the Southern Hemisphere where seasonal meridional variations in
 723 M_{θ_e} surfaces are small, the Northern Hemisphere shows pronounced seasonal shifts due to
 724 different land/ocean heating and cooling cycles.



725

726 Figure 10: Similar to Fig. 8, but showing diabatic mixing rates and cross- M_{0e} APO gradients in
 727 the Northern Hemisphere late winter / early spring (A) and late-summer / early fall (B) of the 45
 728 $\times 10^{16} \text{ kg } M_{0e}$ surface. We choose January to March and August to October due to sufficient
 729 aircraft sampling and maximum cross- M_{0e} APO gradients in these months.

730 3.3. Shipboard model-observation comparison over the Drake Passage

731 The APO-MIP1 simulations could not reproduce latitudinal variations in APO seasonal cycle
 732 amplitude observed from shipboard measurements from 53 to 65°S over the Drake Passage and
 733 adjacent to Tierra del Fuego and the Antarctic Peninsula. Observations reveal a strong
 734 meridional SCA gradient ($-2.1 \text{ per meg deg}^{-1}$, with deg positive northward), with SCA increasing
 735 sharply towards higher southern latitudes (Fig. 11). Model simulations substantially
 736 underestimate this latitudinal gradient (Fig. 11), showing weaker slopes averaged across ATMs
 737 of -1.2 (Jena), -0.5 (CESM), and 0.8 (DISS) per meg deg^{-1} . Notably, these gradients remain
 738 generally consistent across different ATMs for each flux product (± 0.26 , ± 0.13 , and ± 0.29 per
 739 meg deg^{-1} , respectively), suggesting this may predominantly be a result of zonal-scale latitudinal
 740 biases in flux seasonality. Underrepresentation of enhanced summertime productivity along the
 741 coast of the Antarctic Peninsula in flux products could also play a role. However, the Gould
 742 typically only transits waters with elevated chlorophyll south of approximately 62°S while the
 743 gradient biases appear further north. Furthermore, seasonally, the SCA biases are caused more by
 744 underestimation of the winter/spring drawdown in APO at high latitudes, rather than the smaller
 745 underestimation of summertime APO enhancement (Figs. S10-11). For CESM, this bias could

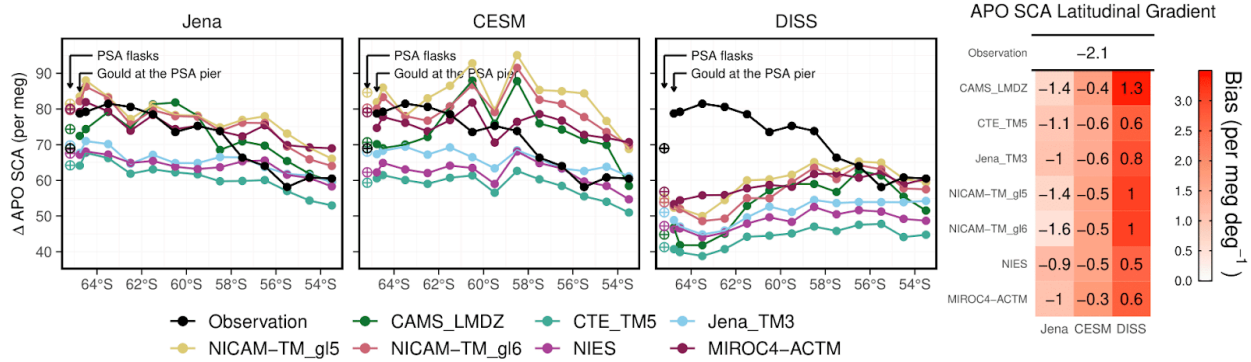
originate from incomplete process representation in the ocean biogeochemistry model and the underestimation of winter mixed-layer depths in the Pacific sector of the Southern Ocean, which has historically been a problem for Earth System Models (Sallée et al., 2013). The Jena flux product provides the closest match to the observed SCA gradient. However, several limitations remain, which likely stem from the coarse spatial resolution, limited atmospheric observational constraints over the Southern Ocean, and underrepresentation of mixing patterns around the PSA station (see details below and in SI). The DISS flux product is biased due to its underlying assumptions and sparse observational constraints, as discussed in Jin et al. (2023).

Across ATMs, we find systematic differences of up to $\pm 20\%$ in simulated mean SCA for the entire ship transects over the Drake Passage, independent of the input flux field, with CTE_TM5 consistently producing the smallest SCA and NICAM-TM_gl5 showing the largest. These differences across ATMs are likely caused by differences in marine boundary-layer ventilation in the models. Near-surface mixing over the Southern Ocean is challenging to model, owing to complex boundary-layer structure, strong wind shear, frequent storm systems, SST variations, and poorly represented clouds (Hyder et al., 2018; Knight et al., 2024; Lang et al., 2018; Truong et al., 2020). The coarse-resolution models used here may struggle to capture such phenomena, and the resulting variations in the concentration or dilution of flux signals near the surface drives differences in mean APO SCA. The systematic spread also likely reflects biases in the representation of large-scale diabatic mixing over the high southern latitudes. Models with strong diabatic mixing rates, such as TM5, tend to dilute the meridional gradient of seasonal amplitude through excessive mixing with lower-latitude air masses that have smaller SCAs, resulting in reduced amplitudes at high southern latitudes.

We find that observed SCA at PSA (64.5°S) from SIO flask measurements (~ 70 per meg, averaged from 2012 to 2017) is significantly smaller than nearby ship data from 64°S to 65°S (~ 80 per meg). However, model simulations suggest similar values for both locations. The shipboard measurements are closely tied to the SIO O_2 calibration scale, and any remaining scale differences would be unlikely to affect the seasonal APO SCA. Rather, the observed SCA difference occurs because SIO flask samples collected at PSA predominantly sample descending air masses from the east that have passed over Anvers Island and the Antarctic Peninsula, with peaks above 2000 m (characterized by small APO SCA), whereas the ship samples marine

boundary layer air including that over highly productive ocean regions (large APO SCA). As shown in Figs. S7-9, the SIO flasks are collected from the Terra Lab, on the east side of the station, with a wind selection criteria of 5-205°. Even while docked at Palmer (left-most points in Fig. 11), the Gould measurements show elevated SCA compared to PSA flask samples, because the pier is located to the west of the station with samples filtered to exclude air influenced by the station (Figs. S7-9). None of the ATMs, regardless of the flux product used, could reconstruct this feature, even though the models were sampled at the flask collection times. This difference is consistent with that seen between 900-mbar airborne samples and PSA flasks (Fig. 5E). The systematic bias points to the lack of resolution or physics that would be necessary, in either the reanalysis products or the ATMs, to accurately capture fine-scale circulation patterns, particularly the distinct air mass origins affecting ship versus station measurements. We note that the Jena flux product has been optimized to match seasonal APO cycles at Cape Grim Observatory (41°S) and at PSA (64.5°S), which may be the reason for its better performance on the SCA latitudinal gradient. It may do even better if the shipboard data were used in the inversion or if the effective sampling altitude of the SIO flasks at PSA were better accounted for.

Our analysis underscores the need for improvements in both ocean biogeochemistry models and ATMs. Future ocean process model developments should include improving accuracy of winter mixed-layer depths and higher-resolution ocean models with enhanced process representation to capture the fine-scale productivity patterns in the Southern Ocean. Additionally, current atmospheric transport models require improved resolution and physics to better represent the complex circulation patterns characteristic of coastal regions.



797

798 Figure 11: Latitudinal distribution of APO SCA across the Drake Passage region (53°S-65°S)
 799 derived from ship observations and model simulations. We calculate SCA by grouping
 800 observations and model simulations into 1 deg latitude bands, shown as points. Model results are
 801 color-coded by ATM and organized by flux products in separate panels. The full seasonal cycles
 802 of observed and simulated APO of these latitude bands are shown in Fig. S10. We also show
 803 SCA observed and simulated for the PSA flask record as open crossed circles (~64.5°S, shifted
 804 0.7° south for visibility), and for ship data while the Gould is docked at or close to the PSA pier
 805 (left-most points, calculated by selecting data from 64.82°S to 64.72°S and 64.1°W to 64.0°W).
 806 The right-most three bands (53°S to 55°S) are typically downwind of Tierra del Fuego (Figs.
 807 S7-9). Both observational and model data for each latitude band or at PSA were detrended using
 808 corresponding cubic smooth spline fits from SPO. SCA was calculated using two-harmonic fits.
 809 The rightmost panel shows the SCA latitudinal gradients (per meg deg⁻¹) from 53°S to 65°S, with
 810 red shading indicating model biases relative to observations. The gradient is calculated as linear
 811 fits of SCA from 53°S to 65°S for each ATM and flux product pair, and the observations. We
 812 exclude CAM-SD in this analysis because the ship data simulation is only available from 2012 to
 813 2015 (i.e., missing 2016 to 2017 data).

814 3.4. Implications for APO and CO₂ inversions and ATM development

815 Our study motivates a community effort to conduct APO inversions. Estimates of spatial and
 816 temporal variations in APO fluxes can improve our understanding of ocean biogeochemical
 817 processes and heat transport, and support verification of fossil-fuel emission estimates (Pickers et
 818 al., 2022; Rödenbeck et al., 2023). Currently, only one global-scale APO inversion product from
 819 Jena CarboScope (Rödenbeck et al., 2008) exists. This product shows excessive seasonal flux

820 amplitudes (Fig. 2) in the southern low-latitudes (~ 30 to 0°S)tropics and northern mid-latitudes
821 (~ 30 to 60°N) relative to the other two flux products, which show better consistency with
822 aircraft observations in their forward transport simulations (Fig. 6)~~are more consistent with~~
823 ~~aircraft observations (Figs. 8 and 9)~~. These biases in Jena APO inversion partly result from
824 limitations in the TM3 model, which exhibits excessive vertical mixing, particularly in the
825 eastern North Pacific, too rapid diabatic mixing in the southern mid-latitudes, and
826 underrepresentation of monsoon dynamics primarily due to coarse resolution (Jin et al., 2023).
827 The large spread and biases in ATMs shown in this study highlight the importance of developing
828 APO inversions using different ATMs and methodologies, as this will improve our ability to
829 fully assess methodological uncertainties and potential biases in inverted air-sea APO flux
830 estimates.

831 We encourage future inversion efforts to also assimilate column-mean data from airborne
832 campaigns, in addition to sparse surface stations, especially for studying climatological seasonal
833 fluxes. Our study finds that forward simulations from ATMs generally show large spread at
834 northeastern Pacific sites, particularly at LJO and CBA (Fig. 2), where simulations are sensitive
835 to model representation of the marine boundary layer and vertical mixing. The Scripps APO
836 observation network consists mainly of stations along a Pacific transect close to the primary
837 oceanic sources and sinks. Given this limited spatial coverage and our findings of significant
838 vertical mixing biases (e.g., at CBA and LJO) and local wind-direction biases (e.g., at LJO and
839 PSA) in ATMs at the station level, APO inversions that rely solely on these surface observations
840 may be subject to large representation errors. Airborne data, however, provide larger surface
841 footprints and column average metrics that are much less sensitive to vertical mixing biases. Our
842 analysis shows that ATMs are generally consistent with each other in simulating large-scale
843 annual and seasonal column-mean features along flight tracks (Fig. 6). Thus, inversions
844 configured to assimilate airborne column-mean observations would be promising. Further
845 improvement could also be achieved by incorporating shipboard observations to expand zonal
846 coverage, such as from the Gould, across the Atlantic (Pickers et al., 2017), and in the Western
847 Pacific (Tohjima et al., 2012). The study of Jin et al. (2023) used a different configuration of the
848 Jena inversion that also assimilated Japanese ship-based observations across the western Pacific
849 (Tohjima et al., 2012) from 40°S to 50°N . Forward transport of APO fluxes in that configuration

aligns better with station and airborne data compared to the configuration used in this study, particularly in reducing the SCA bias in the tropics, suggesting better flux representations.

Biases in diabatic mixing diagnosed from ATMs (Section 3.2) imply that CO₂ inversions using these ATMs are also likely biased. A previous study showed that summer-time Southern Ocean CO₂ estimates from inversion products are correlated with corresponding simulated summer-time cross-isentrope CO₂ gradients in inversions (Long et al., 2021b). The simulated gradients are shown to be biased too small due to too rapid diabatic mixing bias in ATMs leading to an overestimation of Southern Ocean CO₂ uptake in the summer (Jin et al., 2024). It is likely that biases in ATMs also contribute to the large spread found in OCO-2 MIP and Global Carbon Project (GCP) inversion ensembles (Byrne et al., 2023; Crowell et al., 2019; Friedlingstein et al., 2025; Peiro et al., 2022). We identify several priority areas for understanding biases in ATMs, particularly the inconsistency between diabatic mixing rates diagnosed from the MSE budgets of parent reanalysis and the tracer fields of coarser resolution ATMs identified here. These inconsistencies likely stem from several potential sources: (1) regridding of original reanalyses to the coarser resolution of the ATM grid, (2) for online GCMs using nudging, incomplete matching of the input meteorology, and (3) for offline models, recalculation or parameterization of convective mass fluxes in the coarser ATM. The first potential source of error from regridding could be evaluated by comparing MSE-based diabatic mixing rates from the parent and regridded fields as long as all components of MSE were included in the regridding. The second potential source of error from nudging could be evaluated by comparing MSE-based diabatic mixing rates from the regridded parent model and the nudged online simulation. Finally, the third potential source of error from recalculating or parameterizing vertical mass fluxes could be evaluated by comparing the MSE-based diabatic mixing rates from the regridded parent model and the tracer-based mixing rates from the ATM. It is notable that diabatic mixing rates diagnosed from two online models, MIROC4-ACTM and CAM-SD, which do not require regridding, are generally consistent with observations, with MIROC4-ACTM showing the best performance among all models (Figs. 7-10).

An important consideration is that the real atmosphere mixes MSE and tracers at different spatial and temporal scales. In the Northern Hemisphere, APO fluxes initially mix vertically over oceans, while strong CO₂ fluxes initially mix vertically over land. In contrast, MSE fluxes mix

initially over both land and ocean. Due to the large land area in the Northern Hemisphere, the zonal mixing time scale is much longer (~ 2 -4 weeks) so that diabatic mixing rates diagnosed from APO or CO₂ tracers could differ from each other and from those diagnosed from MSE tracers. In the Southern Hemisphere mid-latitudes, these potential differences are much smaller due to the predominance of ocean and rapid zonal mixing (~ 1 -2 weeks). In general, the timescales for diabatic mixing are longer than the timescales of zonal mixing, which support our approach of using tracer fluxes over both ocean and land to evaluate zonal-mean diabatic mixing. Future work should also develop metrics for quantifying along-isentrope (adiabatic) transport to complement our understanding of tracer mixing across isentropes. The timescales of adiabatic mixing influences tracer gradients along isentropic surfaces, which in turn affects diabatic mixing differently in the upper versus lower troposphere. It is also necessary to examine the sensitivity of mixing rates to model resolution, particularly vertical levels at the interface between the boundary layer and free troposphere, and boundary layer schemes. These ATM improvements are essential for enhancing both forward simulations and inverse estimates of surface fluxes.

4. Summary and Outlook

We conducted the Atmospheric Potential Oxygen forward Model Intercomparison Project (APO-MIP1) to generate forward simulations of APO and its components using different flux products and eight ATMs. This effort provides model APO simulations at surface stations, along aircraft flight paths, and on ships that can be directly compared with observations. Additionally, we provide 3-D APO fields from six of the eight ATMs. We use simulations from APO-MIP1 to evaluate eight ATMs and three flux products by comparing simulations against observations from surface stations, aircraft, and ships.

We find that model simulations of APO seasonal cycles using a given flux product show considerable summer-time spread at northern surface stations, particularly at two eastern Pacific stations, LJO and CBA (Fig. 3). The bias stems from challenges in accurately representing complex atmospheric vertical transport processes, marine boundary layer mixing, and coastal horizontal mixing in these regions. These findings highlight the limitations of current APO inversions that rely on a single ATM (i.e., TM3 used in Jena APO inversion) and sparse surface

909 observations. However, model simulations of column-average APO resolved from sampling
910 aircraft tracks are consistent across different ATMs, emphasizing the importance of airborne
911 measurements for constraining large-scale flux features.

912 Using airborne observations and a moist-isentropic coordinate framework, we demonstrate that
913 most ATMs overestimate diabatic mixing rates in the mid-latitudes of both hemispheres when
914 compared to mixing rates derived from energy budgets of reanalyses. Among all ATMs used
915 here, Jena_TM3 and CTE_TM5 show the largest biases. These constraints also enable us to
916 separate flux biases from transport-related biases, allowing independent evaluation of flux
917 models, which show that the CESM flux product is the best among the three flux products used
918 in this study. This prognostic model outperforms two observation based products because of
919 sparse atmospheric and surface observations, limitations in ATM used in atmospheric inversion,
920 and because seasonal APO fluxes are driven by physical and biological processes that CESM
921 represents well.

922 We encourage the broader community to develop new APO inversions, which could provide
923 independent constraints on ocean biogeochemical processes and improve our understanding of
924 the ocean carbon sink. Model simulations from APO-MIP1 can be used in other applications,
925 including the calibration of methods for estimating seasonal air-sea APO fluxes from global
926 atmospheric observations (e.g., Jin et al., 2023), constraining the representation of regional to
927 global marine production in Earth system models (e.g., Nevison et al., 2012, 2015, 2018), and for
928 understanding ESM biases in seasonal air-sea CO₂ exchange related to both thermal and
929 non-thermal forcings. The transport simulations can also support the evaluation of long-term
930 trends in O₂:CO₂ ratios over the Southern Ocean based on surface station gradients, useful for
931 assessing biogeochemical responses to climate change.

932 We expect APO-MIP1 to continue evolving as an active collaboration examining atmospheric
933 tracer transport and air-sea O₂ flux estimates. The current implementation excluded the air-sea
934 CO₂ component and long-term flux trends from the Jena flux product, and does not include
935 interannual and long-term flux trends in the DISS flux product, making these simulations
936 unsuitable for interpreting interannual to long-term air-sea O₂ fluxes features. Thus, we only
937 analyze APO seasonal cycles and meridional gradients here. The next phase of APO-MIP1 will
938 address these limitations by incorporating updated inversion flux fields based on a larger set of

atmospheric APO observations and including interannual variability. We will expand the scope by including terrestrial O₂ flux fields for O₂-specific analyses and seasonal-only component fluxes to investigate rectifier effects. The seasonal rectifier effect refers to the creation of non-zero annual mean atmospheric concentration gradients at surface stations even with balanced seasonal O₂ fluxes. This occurs when fluxes correlate with seasonal variations in atmospheric mixing. For example, strong summer O₂ outgassing combined with shallow PBL heights concentrates APO near the surface, while higher winter PBL dilutes the O₂ uptake signal, resulting in observed annual mean APO gradients even when the annual mean flux is zero. Additionally, we plan to update air-sea O₂ fluxes derived from surface ocean dissolved oxygen measurements by replacing Garcia and Keeling (2001) with fluxes calculated from recent machine learning interpolation of dissolved oxygen products (Gouretski et al., 2024; Ito et al., 2024; Sharp et al., 2023). We encourage broader participation from diverse modeling groups in the next phase of APO-MIP1.

Appendix A: Surface station, airborne, and shipboard APO measurements.

The surface station APO observations from the Scripps O₂ program have been described in (Keeling et al., 1998). Briefly, flask triplicates have been collected at biweekly to monthly frequency during clean background air conditions at a network of sites for over three decades, and returned to Scripps for analysis using interferometric and mass-spectrometric techniques. Here we use monthly data that was averaged from roughly bi-weekly data. The flask measurements are first adjusted to the middle of each month, parallel to the mean seasonal cycle for that station, before averaging. The APO-MIP1 output for these stations was reported matching the ObsPack CO₂ files from the Scripps O₂ Program, to take advantage of the established ObsPack format. These CO₂ measurements correspond to the same flask air on which O₂ is measured. The model output is treated in the same way as the observations to generate monthly means.

Airborne APO measurements from HIPPO, ORCAS, and ATom campaigns were made in situ with the NSF NCAR Airborne Oxygen Instrument (AO2), using a vacuum-ultraviolet absorption technique to measure O₂ and a single-cell infrared gas analyzer to measure CO₂ (Stephens et al., 2021). AO2 produces measurements every 2.5 s, which are averaged to 10 sec frequency for

merging with other aircraft data. To correct for flight-specific sampling offsets, the in situ AO₂ data were adjusted to agree with flask measurements collected during each flight using the NSF NCAR / Scripps Medusa flask sampler on a flight-by-flight average basis (Jin et al., 2023; Stephens et al., 2021).

HIPPO and ATom had nearly pole-to-pole coverage, and from near surface (150 - 300 m) to above the tropopause. HIPPO consisted of five campaigns between 2009 and 2011, and most data were collected above the Pacific. ATom consisted of four campaigns between 2016 and 2018, and each campaign had a Pacific transect and an Atlantic transect. ORCAS was a 6-week campaign with dense temporal sampling over the Drake Passage and ocean areas adjacent to the tip of South America and the Antarctic Peninsula. The APO-MIP1 output for these aircraft measurements was reported matching the ObsPack CO₂ files for each campaign. These data are also at 10 sec frequency but correspond to different instruments with different calibration intervals. To match the observed and model time series, we mask observations when model output is not available, and vice versa. We also exclude any stratospheric data, with the stratosphere defined as water vapor concentrations below 50 ppm and either ozone concentrations exceeding 150 ppb, or detrended N₂O levels (normalized to 2009) below 319 ppb (Jin et al., 2021). Water vapor and ozone were measured by the NOAA UAS Chromatograph for Atmospheric Trace Species instrument (Hintsa et al., 2021). N₂O was measured by the Harvard Quantum Cascade Laser System instrument (Santoni et al., 2014). We filter the airborne data to exclude continental or urban boundary-layer air sampled while landing, taking off, or conducting missed approaches at airports (Jin et al., 2021).

Shipboard APO measurements from the ARSV *L. M. Gould* were made in situ during over 90 transects of Drake Passage on 50 cruises between 2012 and 2017 using a fuel-cell method for O₂ and a two-cell non-dispersive infrared gas analyzer for CO₂. The instrumentation was similar to a previously developed tower system (Stephens et al., 2003), but adapted and optimized for shipboard use. The instrument produces measurements at 1 min frequency. The cruises occurred in all months of the year but are more sparse during austral winter. The Gould operated almost exclusively between Punta Arenas, Chile and Palmer Station, Antarctica, in support of resupplying and transferring personnel to Palmer Station. The cruises span from 53° to 65°S in all months, and extend as far as 70°S during summer months. The APO-MIP1 output for the

998 Gould was reported matching the ObsPack CO₂ file from the NOAA underway pCO₂ system.
999 This system measures atmospheric CO₂ for 15 min every two hours. To match the observed and
1000 model time series, we first calculate hourly means for each and then mask observations when
1001 model output is not available, and vice versa.

1002 The resolved APO annual mean and seasonal cycles have negligible measurement uncertainty
1003 compared to model spread because we average data over long time series for stations and over
1004 large spatial domains for aircraft and ships, effectively reducing the already small short-term
1005 instrument imprecision.

1006 **Appendix B: APO flux products**

1007 **B.1. Air-sea APO flux products**

1008 The first air-sea APO flux product (Jena) is air-sea APO flux from the Jena CarboScope APO
1009 Inversion (version ID: apo99X_v2021), which is available directly as F_{APO}^{ocn} (update of
1010 Rödenbeck et al., 2008). In this inversion, the posterior fluxes (variable name: apoflux_ocean)
1011 were optimized to best match observed APO at 9 stations in the Scripps O₂ Program surface
1012 network (Manning and Keeling, 2006) and at 2 stations from the National Institute for
1013 Environmental Studies (Tohjima et al., 2012). The prior air-sea CO₂ flux was not included in the
1014 forward simulations here. We note that the exclusion of prior air-sea CO₂ flux has only minimal
1015 impact on the simulated APO seasonal cycle and north-to-south annual gradient but reduces the
1016 tropical “bulge” of annual mean by approximately 1 per meg and results in close to zero
1017 long-term APO trend. The Jena product is available from 1999 to 2020 originally with spatial
1018 resolution of 2° latitude × 2.5° longitude at daily intervals, converted to 1° × 1°. The Jena
1019 inversion used the TM3 transport model, which is also one of the models participating in
1020 APO-MIP1. In the case of TM3 forward transport simulation, the Jena inversion posterior fluxes
1021 have been re-run forward through the ATM, and thus this combination of fluxes and transport
1022 should agree well at the surface stations used for inversion optimization.

1023 The second air-sea APO flux product (CESM) uses air-sea O₂, CO₂, and N₂ flux components
1024 from the Community Earth System Model (CESM2) Forced Ocean-Sea-Ice (FOSI) simulation
1025 (Yeager et al., 2022), which is forced by atmospheric fields from JRA55-do reanalysis (Tsujino

et al., 2018) and prognostic ocean biogeochemistry using the Marine Biogeochemistry Library (MARBL, Long et al., 2021a). The model directly produces $F_{O_2}^{ocn}$ and $F_{CO_2}^{ocn}$, while $F_{N_2}^{ocn}$ is calculated by scaling the ocean heat flux (Q , $W\ m^{-2}$) output using the relationship from Keeling and Shertz (1992) following

$$F_{N_2}^{ocn} = - \frac{1}{1.3} \cdot \frac{dS}{dT} \cdot \frac{Q}{C_p}, \quad (B1)$$

where dS/dT ($mol\ kg^{-1}\ C^{-1}$) is the temperature derivative of solubility using solubility coefficients from Hamme & Emerson (2004). C_p represents the specific heat capacity of seawater, which is assumed to be $3993\ J\ kg^{-1}\ C^{-1}$. The factor of $1/1.3$ is to adjust the seasonal amplitude due to the temporal lag between tracer flux and heat flux, as proposed by Jin et al. (2007).

These three CESM flux components have a resolution of 1° latitude \times 1° longitude grid with the North Pole displaced to Greenland. All fields are available from 1958 to 2020, but we only use fluxes from 1986 to 2020. $F_{O_2}^{ocn}$ and $F_{CO_2}^{ocn}$ are output from the model at daily resolution, whereas $F_{N_2}^{ocn}$ is calculated from monthly model heat fluxes then interpolated to daily resolution. This version of CESM was designed to initialize a seasonal-to-multiyear large ensemble (SMYLE) of coupled simulations for evaluating predictability. It is forced by observed meteorology starting in 1958, at which point it branches off of a FOSI configuration using JRA55-do atmospheric fields as surface boundary conditions (Yeager et al., 2022). The FOSI simulation consists of six consecutive cycles of 1958-2018 forcing, with the sixth cycle (used for SMYLE) extended through 2020. Annual mean heat fluxes from this configuration show a small cooling drift over the historical period, and thus the inferred annual mean and long-term trend of O_2 and N_2 flux should not be interpreted as realistic.

The third air-sea APO flux product (DISS) uses bottom-up air-sea O_2 and CO_2 flux estimates derived primarily from dissolved gas measurements. $F_{O_2}^{ocn}$ consists of a seasonal component calculated from the dissolved O_2 measurement based climatology of Garcia & Keeling (2001), with seasonal amplitude scaled by 0.82 according to Naegler et al. (2006), and an annual mean

component from the ocean inversion of Resplandy et al. (2016) for 21 regions using transport
 from MITgcm-ECCO. Bent (2014) reported that the 0.82 scaling factor significantly improved
 agreement between GK flux and HIPPO observations, based on simulations using one ATM (a
 different MIROC4-ACTM configuration). However, our results show that applying this 0.82
 scaling factor actually leads to an underestimation of modelled column-mean APO SCA when
 comparing with the combined HIPPO, ORCAS, and ATom observations at high latitudes in both
 hemispheres. The seasonal component ($1.125^\circ \times 1.125^\circ \times$ monthly) was linearly regridded to 1°
 $\times 1^\circ \times$ daily resolution. For the annual mean component, the original regional values (21 regions)
 were spatially interpolated to $1^\circ \times 1^\circ$ resolution while conserving the total sum within each
 region, then temporally interpolated to daily values. We use $F_{CO_2}^{ocn}$ from the machine learning
 interpolation of pCO₂ based air-sea CO₂ fluxes (Jersild et al., 2017; Landschützer et al., 2016).
 The version of this product that we used provides fluxes from 1982 to 2020, with resolution of 1°
 latitude $\times 1^\circ$ longitude \times monthly, which we interpolated to daily. We use Eq. B1 to calculate
 $F_{N_2}^{ocn}$ with heat fluxes from ERA5 reanalyses (Hersbach et al., 2020), which is available from
 1979 onwards, with resolution of 0.25° latitude $\times 0.25^\circ$ longitude \times monthly. Sea-surface
 temperature (SST) estimates required to calculate dS/dT (Eq. B1) are from World Ocean Atlas
 (WOA) v2018 with resolution of 1° latitude $\times 1^\circ$ longitude \times monthly. SST is available as a 1981
 to 2010 climatology but we use it repeatedly for 1986 to 2020.

B.2. Fossil fuel APO uptake products

We used two products for F_{APO}^{ff} . The first product (GridFED) uses fossil CO₂ emission and O₂
 uptake fluxes from Jones et al. (2021), downloaded from Jones et al. (2022). This product is
 available from 1959 to 2020, with resolution of 0.1° latitude $\times 0.1^\circ$ longitude \times monthly, which
 we interpolate to daily.

The second product (OCO2MIP) use $F_{CO_2}^{ff}$ as prepared for the OCO-2 Model Intercomparison
 Project (MIP) version 10, downloaded from Basu & Nassar (2021), with resolution of 1° latitude
 $\times 1^\circ$ longitude \times hourly. This $F_{CO_2}^{ff}$ product uses fossil fuel CO₂ emission from ODIAC (Oda et
 al., 2018) for 2000 to 2019. For 2020, the flux was scaled from 2019 using the ratio of 2020 to

1079 2019 global emissions reported by Liu et al. (2020). $F_{O_2}^{ff}$ is not available from this product, but
 1080 we scale the atmospheric field of ΔCO_2^{ff} by a factor of -1.4 to estimate ΔO_2^{ff} (Keeling, 1988;
 1081 Steinbach et al., 2011). We primarily use GridFED, except for CAMS_LMDZ where we use
 1082 OCO2MIP instead, because $F_{O_2}^{ff}$ from GridFED is missing for years after 2015. The differences
 1083 between these two products are negligible compared to the magnitude of ocean-driven APO
 1084 variations, for the seasonal metrics considered here.

1085 **Appendix C: Calculation of M_{θ_e} , cross- M_{θ_e} diabatic mixing rates and APO** 1086 **gradients**

1087 The mass-indexed moist isentropic coordinate M_{θ_e} is defined as the total dry air mass under a
 1088 specific moist isentropic surface (θ_e) in the troposphere of a given hemisphere. Surfaces of
 1089 constant M_{θ_e} are parallel to surfaces of constant θ_e but the relationship changes with season, as
 1090 the atmosphere warms and cools. M_{θ_e} surfaces have air mass (10^{16} kg) as the unit, and are
 1091 adjusted to conserve dry air mass below the surface at any instant in time. M_{θ_e} is calculated as a
 1092 function of θ_e and time following

$$1093 \quad M_{\theta_e}(x, t) = \sum M_x(t) | \theta_{e_x} < \theta_e, \quad (C1)$$

1094 where x indicates an individual grid cell of the atmospheric field, $M_x(t)$ is the dry air mass of
 1095 each grid cell x at time t , and θ_{e_x} is the equivalent potential temperature of the grid cell. For a
 1096 given θ_e threshold, the corresponding M_{θ_e} value is calculated by integrating the air mass of all
 1097 grid cells with θ_e value smaller than the threshold. We only integrate air mass in the troposphere,
 1098 which is defined here as potential vorticity unit (PVU) smaller than 2. At each time step, this
 1099 calculation yields a unique value of M_{θ_e} for each value of θ_e as well as a 3-D field of atmospheric
 1100 M_{θ_e} . Following the spatial pattern of θ_e , M_{θ_e} values generally increase from low to high altitudes
 1101 and from poles to equator. We generate daily M_{θ_e} fields using four different reanalysis products
 1102 (MERRA-2, JRA-55, JRA-3Q, and ERA5) at their native resolution, avoiding potential
 1103 information loss from grid interpolation (Gelaro et al., 2017; Hersbach et al., 2020; Kobayashi et
 1104 al., 2015; Kosaka et al., 2024).

1105 The calculation of diabatic mixing rates in ATMs is based on a box model approach, which uses
 1106 M_{θ_e} as boundaries. A schematic of the box model is available as Fig. 1 of Jin et al. (2024). The
 1107 box model invokes tracer air mass balance, which recognizes tracer inventory change (M_i , Tmol)
 1108 of each M_{θ_e} box equal to the sum of surface fluxes (F_i , Tmol day⁻¹) and the diabatic transport
 1109 between boxes ($T_{i,i+1}$, Tmol day⁻¹, positive poleward). The transport term is considered as a
 1110 diffusive system, which is parameterized as the product of diabatic mixing rate across the M_{θ_e}
 1111 boundary ($D_{i,i+1}$, (10¹⁶ kg)² day⁻¹) and the tracer concentration (χ_{i+1} , Tmol tracer per kg air mass)
 1112 gradient between two boxes. The full mass balance follows

$$\frac{\partial M_i}{\partial t} = \begin{cases} F_i + T_{i,i+1} & \text{if } i = 1 \\ F_i + T_{i,i+1} - T_{i-1,i} & \text{if } i > 1, \end{cases} \quad (C2)$$

1115 with

$$T_{i,i+1} = D_{i,i+1} \cdot \frac{\chi_{i+1} - \chi_i}{\Delta M_{\theta_e}}. \quad (C3)$$

1117 In these equations, i is the number label of the box and is set to be 1 at the highest latitude, ΔM_{θ_e}
 1118 is the distance in M_{θ_e} coordinates between box centers, which for evenly spaced boxes as used
 1119 here, is the same as the total air mass of each box. In this study, we set the range of each M_{θ_e} box
 1120 to be 15×10^{16} kg air mass, and therefore ΔM_{θ_e} equals the same value. The diabatic mixing rate
 1121 (D) can be expressed as

$$D_{i,i+1}(t) = \frac{\left[\sum_{i'=1}^{i'=i} \left(\frac{dM_{i'}(t)}{dt} - F_{i'}(t) \right) \right]}{[\chi_{i+1}(t) - \chi_i(t)]} \cdot \Delta M_{\theta_e}. \quad (C4)$$

1124 This method effectively reconstructs large-scale tracer transport features (T) in ATMs, as
 1125 demonstrated in Jin et al. (2024). We note that the diabatic mixing rate is a property of the
 1126 corresponding M_{θ_e} and is theoretically insensitive to the choice of box sizes. We calculate
 1127 climatological monthly average (2009 to 2018) diabatic mixing rates for each of the six transport
 1128 models using the 3-D APO fields from transporting each of the three flux products (Figs. 7 and
 1129 9). To assign M_{θ_e} at the model grid locations and times for each ATM, we always use M_{θ_e} from

1130 MERRA-2 interpolated to the ATM grid, to ensure spatial consistency. Using other reanalyses
 1131 only leads to small ($< 5\%$) differences in ATM-diagnosed diabatic mixing rates (Jin et al., 2024).

1132 Independent observational constraints on ATM-diagnosed mixing rates are calculated from moist
 1133 static energy (MSE) budgets of four meteorological reanalyses (Figs. 7 and 9). MSE is a measure
 1134 of static energy that is conserved in adiabatic ascent/descent and during latent heat release due to
 1135 condensation, and naturally aligns with surfaces of θ_e or M_{θ_e} . This diagnostic approach offers
 1136 more robust mixing rate estimates than tracer-based methods in part because MSE maintains
 1137 consistent, non-zero gradients at each reanalysis time step, unlike chemical tracers. Additionally,
 1138 MSE-based mixing rates are directly diagnosed from reanalysis on the original grid, avoiding
 1139 potential artifacts introduced when these fields are interpolated to coarser transport model grids,
 1140 and any recalculation of vertical mass fluxes and subgrid-scale mixing parameterizations in
 1141 ATMs.

1142 The MSE-diagnosed mixing rate calculation adapts our tracer box model framework. In this
 1143 adaptation, we replace tracer inventory (M_i , Tmol) by MSE (S_i , J), replace surface tracer flux (F_i ,
 1144 Tmol day $^{-1}$) by surface heat flux (Q_i , J day $^{-1}$), and add an additional term to account for
 1145 atmospheric radiative energy balance (R_i , J day $^{-1}$), following

$$1146 \quad D_{i,i+1}(t) = \frac{\left[\sum_{i'=1}^{i'=i} \left(\frac{dS_{i'}(t)}{dt} - Q_{i'}(t) - R_{i'}(t) \right) \right]}{[\chi_{i+1}(t) - \chi_i(t)]} \cdot \Delta M_{\theta_e} \quad (C5)$$

1147

1148 We note that the gradient on the denominator in Eq. C5 represents the MSE density gradient (J
 1149 per kg air mass) across the M_{θ_e} surface. The calculation of these terms requires air temperature,
 1150 specific humidity, surface heat flux, including surface sensible and latent heat flux, and radiative
 1151 imbalance from reanalysis. Further details on the process to diagnose mixing rate from both
 1152 ATMs and reanalyses can be found in Jin et al. (2024).

1153 The cross- M_{θ_e} APO gradient was calculated using data grouped into two adjacent boxes in the
 1154 M_{θ_e} space, with box centers spanning 15×10^{16} kg air mass across the target surface boundary.
 1155 For each box, we calculate the average APO concentration by trapezoidal integration of
 1156 detrended APO as a function of M_{θ_e} and dividing by the M_{θ_e} range (Jin et al., 2021). We carry out
 1157 the calculation for each airborne campaign, using the observations, model flight track output, and

1158 3-D model fields. Flight-track estimated cross- M_{0e} APO gradients are not directly comparable to
1159 simulated gradients from full 3-D fields, due to spatial and temporal coverage biases in airborne
1160 observations. We correct for both biases in the APO airborne observations and model flight track
1161 output (detailed in Supplement Text S1).

1162 **Code and Data Availability**

1163 The 10 components of air-sea APO flux and fossil fuel APO uptake products, and the output of
1164 ATM forward transport simulations of these 10 components, including ATM samples at surface
1165 stations, ship transects, aircraft measurements, and 3-D atmospheric fields, are available at
1166 <https://doi.org/10.5065/f3pw-a676> (Stephens et al., 2025). APO observations at surface stations
1167 from the Scripps O_2 network are available at <https://doi.org/10.6075/J0WS8RJR> (Keeling, 2019).
1168 All HIPPO 10-s merge data are available from Wofsy, 2017. Here we use updated HIPPO AO2
1169 data from (Stephens et al., 2021a, 2021b, 2021c, 2021d, 2021e). All ORCAS 10-s merge data are
1170 available at Stephens (2017). Here we use updated ORCAS AO2 data from Stephens et al.
1171 (2021f). All ATom 10-s merge data are available at <https://doi.org/10.3334/ORNLDAAC/1925>
1172 (Wofsy, 2021), including the version of AO2 data used here. O_2 and CO_2 measurements from
1173 ARSV Gould are available at <https://doi.org/10.26023/FDDD-PC3X-4M0X> (Stephens, 2025).
1174 Note that airborne O_2/N_2 data are all on the Scripps O_2 Program SIO2017 O_2/N_2 scale defined on
1175 March 16, 2020, surface station data are on the SIO2023 O_2/N_2 scale defined on August 30, 2024,
1176 and shipboard data are on the SIO2023 O_2/N_2 scale defined on August 30, 2024. Airborne CO_2
1177 measurements are on the WMO X2007 CO_2 scale, while station and shipboard CO_2 data are on
1178 the WMO X2019 CO_2 scale. The use of different scales has only minor impacts on interpreting
1179 APO seasonal cycles and latitudinal gradients. Code used to produce input flux files and to
1180 post-process submitted ObsPack files is available at <https://doi.org/10.5065/f3pw-a676> (Stephens
1181 et al., 2025).

1182 **Acknowledgments**

1183 We would like to acknowledge the efforts of the full HIPPO, ORCAS, and ATom science teams
1184 and the pilots and crew of the NSF NCAR GV and NASA DC-8, as well as the NSF NCAR and
1185 NASA project managers, field support staff, and logistics experts. Atmospheric O_2 measurements

on HIPPO were supported by NSF grants ATM-0628519 and ATM-0628388. ORCAS was supported by NSF grants PLR-1501993, PLR-1502301, PLR-1501997, and PLR-1501292. Atmospheric O₂ measurements on ATom 1 were supported by NSF grants AGS-1547626 and AGS-1547797. Atmospheric O₂ measurements on ATom 2-4 were supported by NSF AGS-1623745 and AGS-1623748. The recent atmospheric measurements of the Scripps O₂ program have been supported via funding from the NSF and the National Oceanographic and Atmospheric Administration (NOAA) under Grants OPP-1922922, [OPP-2329254](#), and NA20OAR4320278, respectively. The atmospheric O₂ measurements from ARSV Laurence M. Gould were supported by NSF grants ANT-0944761, PLR-1341425, and PLR-1543511. For sharing O₃, N₂O, and H₂O measurements, we thank Jim Elkins, Eric Hintsa, and Fred Moore for ATom-1 N₂O data; Ru-Shan Gao and Ryan Spackman for HIPPO O₃ data; Ilann Bourgeois, Jeff Peischl, Tom Ryerson, and Chelsea Thompson for ATom O₃ data; Stuart Beaton, Minghui Diao, and Mark Zondlo for HIPPO and ORCAS H₂O data; and Glenn Diskin and Joshua DiGangi for ATom H₂O data. YJ would like to acknowledge the Advanced Study Program Postdoctoral Fellowship in the NSF National Center for Atmospheric Research. This material is based upon work supported by the NSF National Center for Atmospheric Research, which is a major facility sponsored by the U.S. National Science Foundation under Cooperative Agreement No. 1852977. The work of FC was granted access to the HPC resources of CCRT under the allocation CEA/DRF, and of TGCC under the allocation A0130102201 made by GENCI. NC and PKP are supported by the Environment Research and Technology Development Fund (grant no. JPMEERF24S12205) and Arctic Challenge for Sustainability II (ArCS-II) project (grant no. JPMXD1420318865). YN is supported by JSPS KAKENHI (grant no. JP22H05006, JP80282151) and the Environment Research and Technology Development Fund (grant no. JPMEERF24S12210). IL and JH were supported by the Netherlands Organisation for Scientific Research (grant no. VI.Vidi.213.143 and NWO-2023.003).

Author Contributions

YJ and BS carried out the research and wrote the paper with input from all co-authors. YJ, BS, and MC designed the research. MC prepared input fluxes for the transport models. BS provided airborne and shipboard observation data. EM provided surface station and airborne observation

1215 data. YJ, FC, NC, JH, IL, SM, YN, PP, CR, and JV provided forward transport model
1216 simulations. All authors contributed to reviewing and editing the text.

1217 **Competing Interests**

1218 The contact author has declared that none of the authors has any competing interests.

1219 **References**

1220 Adcock, K. E., Pickers, P. A., Manning, A. C., Forster, G. L., Fleming, L. S., Barningham, T.,
1221 Wilson, P. A., Kozlova, E. A., Hewitt, M., Etchells, A. J., and Macdonald, A. J.: 12 years of
1222 continuous atmospheric O₂, CO₂ and APO data from Weybourne Atmospheric Observatory in the
1223 United Kingdom, *Earth Syst. Sci. Data*, 15, 5183–5206,
1224 <https://doi.org/10.5194/essd-15-5183-2023>, 2023.

1225 Bailey, A., Singh, H. K. A., and Nusbaumer, J.: Evaluating a Moist Isentropic Framework for
1226 Poleward Moisture Transport: Implications for Water Isotopes Over Antarctica, *Geophys. Res.*
1227 *Lett.*, 46, 7819–7827, <https://doi.org/10.1029/2019GL082965>, 2019.

1228 Baker, D. F., Law, R. M., Gurney, K. R., Rayner, P., Peylin, P., Denning, A. S., Bousquet, P.,
1229 Bruhwiler, L., Chen, Y.-H., Ciais, P., Fung, I. Y., Heimann, M., John, J., Maki, T., Maksyutov, S.,
1230 Masarie, K., Prather, M., Pak, B., Taguchi, S., and Zhu, Z.: TransCom 3 inversion
1231 intercomparison: Impact of transport model errors on the interannual variability of regional CO₂
1232 fluxes, 1988–2003, *Glob. Biogeochem. Cycles*, 20, <https://doi.org/10.1029/2004GB002439>,
1233 2006.

1234 Basu, S. and Nassar, R.: Fossil Fuel CO₂ Emissions for the OCO₂ Model Intercomparison
1235 Project (MIP) (2020.1), <https://doi.org/10.5281/zenodo.4776925>, 2021.

1236 Battle, M., Fletcher, S. M., Bender, M. L., Keeling, R. F., Manning, A. C., Gruber, N., Tans, P. P.,
1237 Hendricks, M. B., Ho, D. T., Simonds, C., Mika, R., and Paplawsky, B.: Atmospheric potential
1238 oxygen: New observations and their implications for some atmospheric and oceanic models,
1239 *Glob. Biogeochem. Cycles*, 20, 2005GB002534, <https://doi.org/10.1029/2005GB002534>, 2006.

1240 Belikov, D. A., Maksyutov, S., Krol, M., Fraser, A., Rigby, M., Bian, H., Agusti-Panareda, A.,
1241 Bergmann, D., Bousquet, P., Cameron-Smith, P., Chipperfield, M. P., Fortems-Cheiney, A.,
1242 Gloor, E., Haynes, K., Hess, P., Houweling, S., Kawa, S. R., Law, R. M., Loh, Z., Meng, L.,
1243 Palmer, P. I., Patra, P. K., Prinn, R. G., Saito, R., and Wilson, C.: Off-line algorithm for
1244 calculation of vertical tracer transport in the troposphere due to deep convection, *Atmospheric*
1245 *Chem. Phys.*, 13, 1093–1114, <https://doi.org/10.5194/acp-13-1093-2013>, 2013.

1246 Belikov, D. A., Maksyutov, S., Yaremchuk, A., Ganshin, A., Kaminski, T., Blessing, S.,
1247 Sasakawa, M., Gomez-Pelaez, A. J., and Starchenko, A.: Adjoint of the global
1248 Eulerian–Lagrangian coupled atmospheric transport model (A-GELCA v1.0): development and

validation, *Geosci. Model Dev.*, 9, 749–764, <https://doi.org/10.5194/gmd-9-749-2016>, 2016.

Bent, J.: Airborne Oxygen Measurements over the Southern Ocean as an Integrated Constraint of Seasonal Biogeochemical Processes, University of California, San Diego, 2014.

Blaine, T.: Continuous Measurements of Atmospheric Ar/N₂ as a Tracer of Air-Sea Heat Flux: Models, Methods, and Data, University of California, San Diego, 2005.

Byrne, B., Baker, D. F., Basu, S., Bertolacci, M., Bowman, K. W., Carroll, D., Chatterjee, A., Chevallier, F., Ciais, P., Cressie, N., Crisp, D., Crowell, S., Deng, F., Deng, Z., Deutscher, N. M., Dubey, M. K., Feng, S., García, O. E., Griffith, D. W. T., Herkommer, B., Hu, L., Jacobson, A. R., Janardanan, R., Jeong, S., Johnson, M. S., Jones, D. B. A., Kivi, R., Liu, J., Liu, Z., Maksyutov, S., Miller, J. B., Miller, S. M., Morino, I., Notholt, J., Oda, T., O'Dell, C. W., Oh, Y.-S., Ohyama, H., Patra, P. K., Peiro, H., Petri, C., Philip, S., Pollard, D. F., Poulter, B., Remaud, M., Schuh, A., Sha, M. K., Shiomi, K., Strong, K., Sweeney, C., Té, Y., Tian, H., Velasco, V. A., Vrekoussis, M., Warneke, T., Worden, J. R., Wunch, D., Yao, Y., Yun, J., Zammit-Mangion, A., and Zeng, N.: National CO₂ budgets (2015–2020) inferred from atmospheric CO₂ observations in support of the global stocktake, *Earth Syst. Sci. Data*, 15, 963–1004, <https://doi.org/10.5194/essd-15-963-2023>, 2023.

Carroll, D., Menemenlis, D., Adkins, J. F., Bowman, K. W., Brix, H., Dutkiewicz, S., Fenty, I., Gierach, M. M., Hill, C., Jahn, O., Landschützer, P., Lauderdale, J. M., Liu, J., Manizza, M., Naviaux, J. D., Rödenbeck, C., Schimel, D. S., Van Der Stocken, T., and Zhang, H.: The ECCO-Darwin Data-Assimilative Global Ocean Biogeochemistry Model: Estimates of Seasonal to Multidecadal Surface Ocean *p*CO₂ and Air-Sea CO₂ Flux, *J. Adv. Model. Earth Syst.*, 12, e2019MS001888, <https://doi.org/10.1029/2019MS001888>, 2020.

Chandra, N., Patra, P. K., Niwa, Y., Ito, A., Iida, Y., Goto, D., Morimoto, S., Kondo, M., Takigawa, M., Hajima, T., and Watanabe, M.: Estimated regional CO₂ flux and uncertainty based on an ensemble of atmospheric CO₂ inversions, *Atmospheric Chem. Phys.*, 22, 9215–9243, <https://doi.org/10.5194/acp-22-9215-2022>, 2022.

Chevallier, F.: On the parallelization of atmospheric inversions of CO₂ surface fluxes within a variational framework, *Geosci. Model Dev.*, 6, 783–790, <https://doi.org/10.5194/gmd-6-783-2013>, 2013.

Chevallier, F., Fisher, M., Peylin, P., Serrar, S., Bousquet, P., Bréon, F. -M., Chédin, A., and Ciais, P.: Inferring CO₂ sources and sinks from satellite observations: Method and application to TOVS data, *J. Geophys. Res. Atmospheres*, 110, 2005JD006390, <https://doi.org/10.1029/2005JD006390>, 2005.

Chevallier, F., Ciais, P., Conway, T. J., Aalto, T., Anderson, B. E., Bousquet, P., Brunke, E. G., Ciattaglia, L., Esaki, Y., Fröhlich, M., Gomez, A., Gomez-Pelaez, A. J., Haszpra, L., Krummel, P. B., Langenfelds, R. L., Leuenberger, M., Machida, T., Maignan, F., Matsueda, H., Morguá, J. A., Mukai, H., Nakazawa, T., Peylin, P., Ramonet, M., Rivier, L., Sawa, Y., Schmidt, M., Steele, L. P., Vay, S. A., Vermeulen, A. T., Wofsy, S., and Worthly, D.: CO₂ surface fluxes at grid point scale estimated from a global 21 year reanalysis of atmospheric measurements, *J. Geophys. Res.*, 115, D21307, <https://doi.org/10.1029/2010JD013887>, 2010.

1289 Chikira, M. and Sugiyama, M.: A Cumulus Parameterization with State-Dependent Entrainment
1290 Rate. Part I: Description and Sensitivity to Temperature and Humidity Profiles, *J. Atmospheric*
1291 *Sci.*, <https://doi.org/10.1175/2010JAS3316.1>, 2010.

1292 Crowell, S., Baker, D., Schuh, A., Basu, S., Jacobson, A. R., Chevallier, F., Liu, J., Deng, F.,
1293 Feng, L., McKain, K., Chatterjee, A., Miller, J. B., Stephens, B. B., Eldering, A., Crisp, D.,
1294 Schimel, D., Nassar, R., O'Dell, C. W., Oda, T., Sweeney, C., Palmer, P. I., and Jones, D. B. A.:
1295 The 2015–2016 carbon cycle as seen from OCO-2 and the global in situ network, *Atmospheric*
1296 *Chem. Phys.*, 19, 9797–9831, <https://doi.org/10.5194/acp-19-9797-2019>, 2019.

1297 Danabasoglu, G., Lamarque, J.-F., Bacmeister, J., Bailey, D. A., DuVivier, A. K., Edwards, J.,
1298 Emmons, L. K., Fasullo, J., Garcia, R., Gettelman, A., Hannay, C., Holland, M. M., Large, W.
1299 G., Lauritzen, P. H., Lawrence, D. M., Lenaerts, J. T. M., Lindsay, K., Lipscomb, W. H., Mills,
1300 M. J., Neale, R., Oleson, K. W., Otto-Bliesner, B., Phillips, A. S., Sacks, W., Tilmes, S., van
1301 Kampenhout, L., Vertenstein, M., Bertini, A., Dennis, J., Deser, C., Fischer, C., Fox-Kemper, B.,
1302 Kay, J. E., Kinnison, D., Kushner, P. J., Larson, V. E., Long, M. C., Mickelson, S., Moore, J. K.,
1303 Nienhouse, E., Polvani, L., Rasch, P. J., and Strand, W. G.: The Community Earth System Model
1304 Version 2 (CESM2), *J. Adv. Model. Earth Syst.*, 12, e2019MS001916,
1305 <https://doi.org/10.1029/2019MS001916>, 2020.

1306 Denning, A. S., Holzer, M., Gurney, K. R., Heimann, M., Law, R. M., Rayner, P. J., Fung, I. Y.,
1307 Fan, S.-M., Taguchi, S., Friedlingstein, P., Balkanski, Y., Taylor, J., Maiss, M., and Levin, I.:
1308 Three-dimensional transport and concentration of SF₆ A model intercomparison study
1309 (TransCom 2), *Tellus B Chem. Phys. Meteorol.*, 51, 266–297,
1310 <https://doi.org/10.3402/tellusb.v51i2.16286>, 1999.

1311 Emanuel, K. A.: A Scheme for Representing Cumulus Convection in Large-Scale Models, *J.*
1312 *Atmospheric Sci.*, 48, 2313–2329,
1313 [https://doi.org/10.1175/1520-0469\(1991\)048<2313:ASFRCC>2.0.CO;2](https://doi.org/10.1175/1520-0469(1991)048<2313:ASFRCC>2.0.CO;2), 1991.

1314 Faassen, K. A. P., Nguyen, L. N. T., Broekema, E. R., Kers, B. A. M., Mammarella, I., Vesala, T.,
1315 Pickers, P. A., Manning, A. C., Vilà-Guerau de Arellano, J., Meijer, H. A. J., Peters, W., and
1316 Luijkx, I. T.: Diurnal variability of atmospheric O₂, CO₂, and their exchange ratio above a boreal
1317 forest in southern Finland, *Atmospheric Chem. Phys.*, 23, 851–876,
1318 <https://doi.org/10.5194/acp-23-851-2023>, 2023.

1319 Faassen, K. A. P., Vilà-Guerau de Arellano, J., González-Armas, R., Heusinkveld, B. G.,
1320 Mammarella, I., Peters, W., and Luijkx, I. T.: Separating above-canopy CO₂ and O₂
1321 measurements into their atmospheric and biospheric signatures, *Biogeosciences*, 21, 3015–3039,
1322 <https://doi.org/10.5194/bg-21-3015-2024>, 2024.

1323 Friedlingstein, P., O'Sullivan, M., Jones, M. W., Andrew, R. M., Hauck, J., Landschützer, P., Le
1324 Quéré, C., Li, H., Luijkx, I. T., Olsen, A., Peters, G. P., Peters, W., Pongratz, J., Schwingshackl,
1325 C., Sitch, S., Canadell, J. G., Ciais, P., Jackson, R. B., Alin, S. R., Arneeth, A., Arora, V., Bates,
1326 N. R., Becker, M., Bellouin, N., Berghoff, C. F., Bittig, H. C., Bopp, L., Cadule, P., Campbell,
1327 K., Chamberlain, M. A., Chandra, N., Chevallier, F., Chini, L. P., Colligan, T., Decayeux, J.,
1328 Djeutchouang, L. M., Dou, X., Duran Rojas, C., Enyo, K., Evans, W., Fay, A. R., Feely, R. A.,

- 1329 Ford, D. J., Foster, A., Gasser, T., Gehlen, M., Gkritzalis, T., Grassi, G., Gregor, L., Gruber, N.,
 1330 Gürses, Ö., Harris, I., Hefner, M., Heinke, J., Hurtt, G. C., Iida, Y., Ilyina, T., Jacobson, A. R.,
 1331 Jain, A. K., Jarníková, T., Jersild, A., Jiang, F., Jin, Z., Kato, E., Keeling, R. F., Klein Goldewijk,
 1332 K., Knauer, J., Korsbakken, J. I., Lan, X., Lauvset, S. K., Lefèvre, N., Liu, Z., Liu, J., Ma, L.,
 1333 Maksyutov, S., Marland, G., Mayot, N., McGuire, P. C., Metzl, N., Monacci, N. M., Morgan, E.
 1334 J., Nakaoka, S.-I., Neill, C., Niwa, Y., Nützel, T., Olivier, L., Ono, T., Palmer, P. I., Pierrot, D.,
 1335 Qin, Z., Resplandy, L., Roobaert, A., Rosan, T. M., Rödenbeck, C., Schwinger, J., Smallman, T.
 1336 L., Smith, S. M., Sospedra-Alfonso, R., Steinhoff, T., et al.: Global Carbon Budget 2024, *Earth*
 1337 *Syst. Sci. Data*, 17, 965–1039, <https://doi.org/10.5194/essd-17-965-2025>, 2025.
- 1338 Gallagher, M. E., Liljestrand, F. L., Hockaday, W. C., and Masiello, C. A.: Plant species, not
 1339 climate, controls aboveground biomass O₂:CO₂ exchange ratios in deciduous and coniferous
 1340 ecosystems, *J. Geophys. Res. Biogeosciences*, 122, 2314–2324,
 1341 <https://doi.org/10.1002/2017JG003847>, 2017.
- 1342 Garcia, H. E. and Keeling, R. F.: On the global oxygen anomaly and air-sea flux, *J. Geophys.*
 1343 *Res. Oceans*, 106, 31155–31166, <https://doi.org/10.1029/1999JC000200>, 2001.
- 1344 Gaubert, B., Stephens, B. B., Basu, S., Chevallier, F., Deng, F., Kort, E. A., Patra, P. K., Peters,
 1345 W., Rödenbeck, C., Saeki, T., Schimel, D., Van Der Laan-Luijkx, I., Wofsy, S., and Yin, Y.:
 1346 Global atmospheric CO₂ inverse models converging on neutral tropical land exchange, but
 1347 disagreeing on fossil fuel and atmospheric growth rate, *Biogeosciences*, 16, 117–134,
 1348 <https://doi.org/10.5194/bg-16-117-2019>, 2019.
- 1349 Gelaro, R., McCarty, W., Suárez, M. J., Todling, R., Molod, A., Takacs, L., Randles, C. A.,
 1350 Darmenov, A., Bosilovich, M. G., Reichle, R., Wargan, K., Coy, L., Cullather, R., Draper, C.,
 1351 Akella, S., Buchard, V., Conaty, A., Da Silva, A. M., Gu, W., Kim, G.-K., Koster, R., Lucchesi,
 1352 R., Merkova, D., Nielsen, J. E., Partyka, G., Pawson, S., Putman, W., Rienecker, M., Schubert, S.
 1353 D., Sienkiewicz, M., and Zhao, B.: The Modern-Era Retrospective Analysis for Research and
 1354 Applications, Version 2 (MERRA-2), *J. Clim.*, 30, 5419–5454,
 1355 <https://doi.org/10.1175/JCLI-D-16-0758.1>, 2017.
- 1356 Golaz, J.-C., Larson, V. E., and Cotton, W. R.: A PDF-Based Model for Boundary Layer Clouds.
 1357 Part I: Method and Model Description, *J. Atmospheric Sci.*, 59, 3540–3551, 2002.
- 1358 Goto, D., Morimoto, S., Aoki, S., Patra, P. K., and Nakazawa, T.: Seasonal and short-term
 1359 variations in atmospheric potential oxygen at Ny-Ålesund, Svalbard, *Tellus B Chem. Phys.*
 1360 *Meteorol.*, 69, 1311767, <https://doi.org/10.1080/16000889.2017.1311767>, 2017.
- 1361 Gouretski, V., Cheng, L., Du, J., Xing, X., Chai, F., and Tan, Z.: A consistent ocean oxygen
 1362 profile dataset with new quality control and bias assessment, *Earth Syst. Sci. Data*, 16,
 1363 5503–5530, <https://doi.org/10.5194/essd-16-5503-2024>, 2024.
- 1364 Gruber, N., Gloor, M., Fan, S., and Sarmiento, J. L.: Air-sea flux of oxygen estimated from bulk
 1365 data: Implications For the marine and atmospheric oxygen cycles, *Glob. Biogeochem. Cycles*,
 1366 15, 783–803, <https://doi.org/10.1029/2000GB001302>, 2001.
- 1367 Gurney, K. R., Law, R. M., Denning, A. S., Rayner, P. J., Baker, D., Bousquet, P., Bruhwiler, L.,

1368 Chen, Y.-H., Ciais, P., Fan, S., Fung, I. Y., Gloor, M., Heimann, M., Higuchi, K., John, J.,
 1369 Kowalczyk, E., Maki, T., Maksyutov, S., Peylin, P., Prather, M., Pak, B. C., Sarmiento, J.,
 1370 Taguchi, S., Takahashi, T., and Yuen, C.-W.: TransCom 3 CO₂ inversion intercomparison: 1.
 1371 Annual mean control results and sensitivity to transport and prior flux information, *Tellus B*
 1372 *Chem. Phys. Meteorol.*, 55, 555–579, <https://doi.org/10.3402/tellusb.v55i2.16728>, 2003.

1373 Gurney, K. R., Law, R. M., Denning, A. S., Rayner, P. J., Pak, B. C., Baker, D., Bousquet, P.,
 1374 Bruhwiler, L., Chen, Y.-H., Ciais, P., Fung, I. Y., Heimann, M., John, J., Maki, T., Maksyutov, S.,
 1375 Peylin, P., Prather, M., and Taguchi, S.: Transcom 3 inversion intercomparison: Model mean
 1376 results for the estimation of seasonal carbon sources and sinks, *Glob. Biogeochem. Cycles*, 18,
 1377 <https://doi.org/10.1029/2003GB002111>, 2004.

1378 Hamme, R. C. and Emerson, S. R.: The solubility of neon, nitrogen and argon in distilled water
 1379 and seawater, *Deep Sea Res. Part Oceanogr. Res. Pap.*, 51, 1517–1528,
 1380 <https://doi.org/10.1016/j.dsr.2004.06.009>, 2004.

1381 Hamme, R. C. and Keeling, R. F.: Ocean ventilation as a driver of interannual variability in
 1382 atmospheric potential oxygen, *Tellus B Chem. Phys. Meteorol.*, 60, 706–717,
 1383 <https://doi.org/10.1111/j.1600-0889.2008.00376.x>, 2008.

1384 Heimann, M. and Körner, S.: The global atmospheric tracer model TM3: Model description and
 1385 user's manual Release 3.8a, 2003.

1386 Hersbach, H., Bell, B., Berrisford, P., Hirahara, S., Horányi, A., Muñoz-Sabater, J., Nicolas, J.,
 1387 Peubey, C., Radu, R., Schepers, D., Simmons, A., Soci, C., Abdalla, S., Abellan, X., Balsamo,
 1388 G., Bechtold, P., Biavati, G., Bidlot, J., Bonavita, M., De Chiara, G., Dahlgren, P., Dee, D.,
 1389 Diamantakis, M., Dragani, R., Flemming, J., Forbes, R., Fuentes, M., Geer, A., Haimberger, L.,
 1390 Healy, S., Hogan, R. J., Hólm, E., Janisková, M., Keeley, S., Laloyaux, P., Lopez, P., Lupu, C.,
 1391 Radnoti, G., de Rosnay, P., Rozum, I., Vamborg, F., Villaume, S., and Thépaut, J.-N.: The ERA5
 1392 global reanalysis, *Q. J. R. Meteorol. Soc.*, 146, 1999–2049, <https://doi.org/10.1002/qj.3803>,
 1393 2020.

1394 Hints, E. J., Moore, F. L., Hurst, D. F., Dutton, G. S., Hall, B. D., Nance, J. D., Miller, B. R.,
 1395 Montzka, S. A., Wolton, L. P., McClure-Begley, A., Elkins, J. W., Hall, E. G., Jordan, A. F.,
 1396 Rollins, A. W., Thornberry, T. D., Watts, L. A., Thompson, C. R., Peischl, J., Bourgeois, I.,
 1397 Ryerson, T. B., Daube, B. C., Gonzalez Ramos, Y., Commane, R., Santoni, G. W., Pittman, J. V.,
 1398 Wofsy, S. C., Kort, E., Diskin, G. S., and Bui, T. P.: UAS Chromatograph for Atmospheric Trace
 1399 Species (UCATS) – a versatile instrument for trace gas measurements on airborne platforms,
 1400 *Atmospheric Meas. Tech.*, 14, 6795–6819, <https://doi.org/10.5194/amt-14-6795-2021>, 2021.

1401 Hockaday, W. C., Masiello, C. A., Randerson, J. T., Smernik, R. J., Baldock, J. A., Chadwick, O.
 1402 A., and Harden, J. W.: Measurement of soil carbon oxidation state and oxidative ratio by ¹³C
 1403 nuclear magnetic resonance, *J. Geophys. Res. Biogeosciences*, 114, 2008JG000803,
 1404 <https://doi.org/10.1029/2008JG000803>, 2009.

1405 Holtslag, A. a. M. and Boville, B. A.: Local Versus Nonlocal Boundary-Layer Diffusion in a
 1406 Global Climate Model, *J. Clim.*, 6, 1825–1842,
 1407 [https://doi.org/10.1175/1520-0442\(1993\)006<1825:LVNBLD>2.0.CO;2](https://doi.org/10.1175/1520-0442(1993)006<1825:LVNBLD>2.0.CO;2), 1993.

1408 Hourdin, F. and Armengaud, A.: The Use of Finite-Volume Methods for Atmospheric Advection
 1409 of Trace Species. Part I: Test of Various Formulations in a General Circulation Model, *Mon.*
 1410 *Weather Rev.*, 127, 822–837,
 1411 [https://doi.org/10.1175/1520-0493\(1999\)127<0822:TUOFVM>2.0.CO;2](https://doi.org/10.1175/1520-0493(1999)127<0822:TUOFVM>2.0.CO;2), 1999.

1412 Hourdin, F., Talagrand, O., and Idelkadi, A.: Eulerian backtracking of atmospheric tracers. II:
 1413 Numerical aspects, *Q. J. R. Meteorol. Soc.*, 132, 585–603, <https://doi.org/10.1256/qj.03.198.B>,
 1414 2006.

1415 Hyder, P., Edwards, J. M., Allan, R. P., Hewitt, H. T., Bracegirdle, T. J., Gregory, J. M., Wood, R.
 1416 A., Meijers, A. J. S., Mulcahy, J., Field, P., Furtado, K., Bodas-Salcedo, A., Williams, K. D.,
 1417 Copsey, D., Josey, S. A., Liu, C., Roberts, C. D., Sanchez, C., Ridley, J., Thorpe, L., Hardiman,
 1418 S. C., Mayer, M., Berry, D. I., and Belcher, S. E.: Critical Southern Ocean climate model biases
 1419 traced to atmospheric model cloud errors, *Nat. Commun.*, 9, 3625,
 1420 <https://doi.org/10.1038/s41467-018-05634-2>, 2018.

1421 Ishidoya, S., Morimoto, S., Aoki, S., Taguchi, S., Goto, D., Murayama, S., and Nakazawa, T.:
 1422 Oceanic and terrestrial biospheric CO₂ uptake estimated from atmospheric potential oxygen
 1423 observed at Ny-Ålesund, Svalbard, and Syowa, Antarctica, *Tellus B Chem. Phys. Meteorol.*, 64,
 1424 18924, <https://doi.org/10.3402/tellusb.v64i0.18924>, 2012.

1425 Ishidoya, S., Uchida, H., Sasano, D., Kosugi, N., Taguchi, S., Ishii, M., Morimoto, S., Tohjima,
 1426 Y., Nishino, S., Murayama, S., Aoki, S., Ishijima, K., Fujita, R., Goto, D., and Nakazawa, T.:
 1427 Ship-based observations of atmospheric potential oxygen and regional air–sea O₂ flux in the
 1428 northern North Pacific and the Arctic Ocean, *Tellus B Chem. Phys. Meteorol.*, 68, 29972,
 1429 <https://doi.org/10.3402/tellusb.v68.29972>, 2016.

1430 Ito, T., Cervania, A., Cross, K., Ainchwar, S., and Delawalla, S.: Mapping Dissolved Oxygen
 1431 Concentrations by Combining Shipboard and Argo Observations Using Machine Learning
 1432 Algorithms, *J. Geophys. Res. Mach. Learn. Comput.*, 1, e2024JH000272,
 1433 <https://doi.org/10.1029/2024JH000272>, 2024.

1434 Jersild, A., Landschützer, P., Gruber, N., and Bakker, D. C. E.: An observation-based global
 1435 monthly gridded sea surface pCO₂ and air-sea CO₂ flux product from 1982 onward and its
 1436 monthly climatology (NCEI Accession 0160558), 2017.

1437 Jin, X., Najjar, R. G., Louanchi, F., and Doney, S. C.: A modeling study of the seasonal oxygen
 1438 budget of the global ocean, *J. Geophys. Res. Oceans*, 112, 2006JC003731,
 1439 <https://doi.org/10.1029/2006JC003731>, 2007.

1440 Jin, Y., Keeling, R. F., Morgan, E. J., Ray, E., Parazoo, N. C., and Stephens, B. B.: A
 1441 mass-weighted isentropic coordinate for mapping chemical tracers and computing atmospheric
 1442 inventories, *Atmospheric Chem. Phys.*, 21, 217–238, <https://doi.org/10.5194/acp-21-217-2021>,
 1443 2021.

1444 Jin, Y., Stephens, B. B., Keeling, R. F., Morgan, E. J., Rödenbeck, C., Patra, P. K., and Long, M.
 1445 C.: Seasonal Tropospheric Distribution and Air-Sea Fluxes of Atmospheric Potential Oxygen
 1446 From Global Airborne Observations, *Glob. Biogeochem. Cycles*, 37, e2023GB007827,

1447 <https://doi.org/10.1029/2023GB007827>, 2023.

1448 Jin, Y., Keeling, R. F., Stephens, B. B., Long, M. C., Patra, P. K., Rödenbeck, C., Morgan, E. J.,
 1449 Kort, E. A., and Sweeney, C.: Improved atmospheric constraints on Southern Ocean CO₂
 1450 exchange, *Proc. Natl. Acad. Sci.*, 121, e2309333121, <https://doi.org/10.1073/pnas.2309333121>,
 1451 2024.

1452 Jones, M. W., Andrew, R. M., Peters, G. P., Janssens-Maenhout, G., De-Gol, A. J., Ciais, P.,
 1453 Patra, P. K., Chevallier, F., and Le Quéré, C.: Gridded fossil CO₂ emissions and related O₂
 1454 combustion consistent with national inventories 1959–2018, *Sci. Data*, 8,
 1455 <https://doi.org/10.1038/s41597-020-00779-6>, 2021.

1456 Jones, M. W., Andrew, R. M., Peters, G. P., Janssens-Maenhout, G., De-Gol, A. J., Dou, X., Liu,
 1457 Z., Pickers, P., Ciais, P., Patra, P. K., Chevallier, F., and Le Quéré, C.: Gridded fossil CO₂
 1458 emissions and related O₂ combustion consistent with national inventories 1959–2020
 1459 (GCP-GridFEDv2021.3), <https://doi.org/10.5281/zenodo.5956612>, 2022.

1460 Kalnay, E., Kanamitsu, M., Kistler, R., Collins, W., Deaven, D., Gandin, L., Iredell, M., Saha, S.,
 1461 White, G., Woollen, J., Zhu, Y., Chelliah, M., Ebisuzaki, W., Higgins, W., Janowiak, J., Mo, K.
 1462 C., Ropelewski, C., Wang, J., Leetmaa, A., Reynolds, R., Jenne, R., and Joseph, D.: The
 1463 NCEP/NCAR 40-Year Reanalysis Project, *Bull. Am. Meteorol. Soc.*, 77, 437–472,
 1464 [https://doi.org/10.1175/1520-0477\(1996\)077<0437:TNYRP>2.0.CO;2](https://doi.org/10.1175/1520-0477(1996)077<0437:TNYRP>2.0.CO;2), 1996.

1465 Kay, J. E., Hillman, B. R., Klein, S. A., Zhang, Y., Medeiros, B., Pincus, R., Gettelman, A.,
 1466 Eaton, B., Boyle, J., Marchand, R., and Ackerman, T. P.: Exposing Global Cloud Biases in the
 1467 Community Atmosphere Model (CAM) Using Satellite Observations and Their Corresponding
 1468 Instrument Simulators, *J. Clim.*, <https://doi.org/10.1175/JCLI-D-11-00469.1>, 2012.

1469 Keeling, R.: Development of an Interferometric Oxygen Analyzer for Precise Measurement of
 1470 the Atmospheric O₂ Mole Fraction, Harvard University, 1988.

1471 Keeling, R. F.: Scripps O₂ Program Data. UC San Diego Library Digital Collections,
 1472 <https://doi.org/10.6075/J0WS8RJR>, 2019.

1473 Keeling, R. F. and Manning, A. C.: Studies of Recent Changes in Atmospheric O₂ Content, in:
 1474 *Treatise on Geochemistry*, Elsevier, 385–404,
 1475 <https://doi.org/10.1016/B978-0-08-095975-7.00420-4>, 2014.

1476 Keeling, R. F. and Shertz, S. R.: Seasonal and interannual variations in atmospheric oxygen and
 1477 implications for the global carbon cycle, *Nature*, 358, 723–727,
 1478 <https://doi.org/10.1038/358723a0>, 1992.

1479 Keeling, R. F., Najjar, R. P., Bender, M. L., and Tans, P. P.: What atmospheric oxygen
 1480 measurements can tell us about the global carbon cycle, *Glob. Biogeochem. Cycles*, 7, 37–67,
 1481 <https://doi.org/10.1029/92GB02733>, 1993.

1482 Keeling, R. F., Manning, A. C., McEvoy, E. M., and Shertz, S. R.: Methods for measuring
 1483 changes in atmospheric O₂ concentration and their application in southern hemisphere air, *J.*

- 1484 *Geophys. Res. Atmospheres*, 103, 3381–3397, <https://doi.org/10.1029/97JD02537>, 1998.
- 1485 Keeling, R. F., Walker, S. J., and Paplawsky, W.: Span Sensitivity of the Scripps Interferometric
1486 Oxygen Analyzer, 2020.
- 1487 Knight, C. L., Mallet, M. D., Alexander, S. P., Fraser, A. D., Protat, A., and McFarquhar, G. M.:
1488 Cloud Properties and Boundary Layer Stability Above Southern Ocean Sea Ice and Coastal
1489 Antarctica, *J. Geophys. Res. Atmospheres*, 129, e2022JD038280,
1490 <https://doi.org/10.1029/2022JD038280>, 2024.
- 1491 Kobayashi, S., Ota, Y., Harada, Y., Ebata, A., Moriya, M., Onoda, H., Onogi, K., Kamahori, H.,
1492 Kobayashi, C., Endo, H., Miyaoka, K., and Takahashi, K.: The JRA-55 Reanalysis: General
1493 Specifications and Basic Characteristics, *J. Meteorol. Soc. Jpn. Ser II*, 93, 5–48,
1494 <https://doi.org/10.2151/jmsj.2015-001>, 2015.
- 1495 Kosaka, Y., Kobayashi, S., Harada, Y., Kobayashi, C., Naoe, H., Yoshimoto, K., Harada, M.,
1496 Goto, N., Chiba, J., Miyaoka, K., Sekiguchi, R., Deushi, M., Kamahori, H., Nakaegawa, T.,
1497 Tanaka, T. Y., Tokuhira, T., Sato, Y., Matsushita, Y., and Onogi, K.: The JRA-3Q Reanalysis, *J.*
1498 *Meteorol. Soc. Jpn. Ser II*, 102, 49–109, <https://doi.org/10.2151/jmsj.2024-004>, 2024.
- 1499 Krol, M., Houweling, S., Bregman, B., van den Broek, M., Segers, A., van Velthoven, P., Peters,
1500 W., Dentener, F., and Bergamaschi, P.: The two-way nested global chemistry-transport zoom
1501 model TM5: algorithm and applications, *Atmospheric Chem. Phys.*, 5, 417–432,
1502 <https://doi.org/10.5194/acp-5-417-2005>, 2005.
- 1503 Krol, M., De Bruine, M., Killaars, L., Ouwersloot, H., Pozzer, A., Yin, Y., Chevallier, F.,
1504 Bousquet, P., Patra, P., Belikov, D., Maksyutov, S., Dhomse, S., Feng, W., and Chipperfield, M.
1505 P.: Age of air as a diagnostic for transport timescales in global models, *Geosci. Model Dev.*, 11,
1506 3109–3130, <https://doi.org/10.5194/gmd-11-3109-2018>, 2018.
- 1507 Landschützer, P., Gruber, N., and Bakker, D. C. E.: Decadal variations and trends of the global
1508 ocean carbon sink, *Glob. Biogeochem. Cycles*, 30, 1396–1417,
1509 <https://doi.org/10.1002/2015GB005359>, 2016.
- 1510 Lang, F., Huang, Y., Siems, S. T., and Manton, M. J.: Characteristics of the Marine Atmospheric
1511 Boundary Layer Over the Southern Ocean in Response to the Synoptic Forcing, *J. Geophys. Res.*
1512 *Atmospheres*, 123, 7799–7820, <https://doi.org/10.1029/2018JD028700>, 2018.
- 1513 Langenfelds, R. L.: Studies of the global carbon cycle using atmospheric oxygen and associated
1514 tracers, University of Tasmania, 2002.
- 1515 Law, R. M., Peters, W., Rödenbeck, C., Aulagnier, C., Baker, I., Bergmann, D. J., Bousquet, P.,
1516 Brandt, J., Bruhwiler, L., Cameron-Smith, P. J., Christensen, J. H., Delage, F., Denning, A. S.,
1517 Fan, S., Geels, C., Houweling, S., Imasu, R., Karstens, U., Kawa, S. R., Kleist, J., Krol, M. C.,
1518 Lin, S.-J., Lokupitiya, R., Maki, T., Maksyutov, S., Niwa, Y., Onishi, R., Parazoo, N., Patra, P.
1519 K., Pieterse, G., Rivier, L., Satoh, M., Serrar, S., Taguchi, S., Takigawa, M., Vautard, R.,
1520 Vermeulen, A. T., and Zhu, Z.: TransCom model simulations of hourly atmospheric CO₂:
1521 Experimental overview and diurnal cycle results for 2002, *Glob. Biogeochem. Cycles*, 22,

1522 <https://doi.org/10.1029/2007GB003050>, 2008.

1523 Liu, Z., Ciais, P., Deng, Z., Davis, S. J., Zheng, B., Wang, Y., Cui, D., Zhu, B., Dou, X., Ke, P.,
 1524 Sun, T., Guo, R., Zhong, H., Boucher, O., Bréon, F.-M., Lu, C., Guo, R., Xue, J., Boucher, E.,
 1525 Tanaka, K., and Chevallier, F.: Carbon Monitor, a near-real-time daily dataset of global CO₂
 1526 emission from fossil fuel and cement production, *Sci. Data*, 7, 1–12,
 1527 <https://doi.org/10.1038/s41597-020-00708-7>, 2020.

1528 Long, M. C., Moore, J. K., Lindsay, K., Levy, M., Doney, S. C., Luo, J. Y., Krumhardt, K. M.,
 1529 Letscher, R. T., Grover, M., and Sylvester, Z. T.: Simulations With the Marine Biogeochemistry
 1530 Library (MARBL), *J. Adv. Model. Earth Syst.*, 13, e2021MS002647,
 1531 <https://doi.org/10.1029/2021MS002647>, 2021a.

1532 Long, M. C., Stephens, B. B., McKain, K., Sweeney, C., Keeling, R. F., Kort, E. A., Morgan, E.
 1533 J., Bent, J. D., Chandra, N., Chevallier, F., Commane, R., Daube, B. C., Krummel, P. B., Loh, Z.,
 1534 Lujikx, I. T., Munro, D., Patra, P., Peters, W., Ramonet, M., Rödenbeck, C., Stavert, A., Tans, P.,
 1535 and Wofsy, S. C.: Strong Southern Ocean carbon uptake evident in airborne observations,
 1536 *Science*, 374, 1275–1280, <https://doi.org/10.1126/science.abi4355>, 2021b.

1537 Louis, J.-F.: A parametric model of vertical eddy fluxes in the atmosphere, *Bound.-Layer*
 1538 *Meteorol.*, 17, 187–202, <https://doi.org/10.1007/BF00117978>, 1979.

1539 Lujikx, I. T., Velde, I. R., Veen, E., Tsuruta, A., Stanislawski, K., Babenhauserheide, A., Zhang,
 1540 H. F., Liu, Y., He, W., Chen, H., Masarie, K. A., Krol, M. C., and Peters, W.: The CarbonTracker
 1541 Data Assimilation Shell (CTDAS) v1.0: implementation and global carbon balance 2001–2015,
 1542 *Geosci. Model Dev.*, 10, 2785–2800, <https://doi.org/10.5194/gmd-10-2785-2017>, 2017.

1543 Maksyutov, S., Patra, P., Onishi, R., Saeki, T., and Nakazawa, T.: NIES/FRCGC Global
 1544 Atmospheric Tracer Transport Model: Description, Validation, and Surface Sources and Sinks
 1545 Inversion, *J. Earth Simulator*, 9, 3–18, <https://doi.org/10.32131/jes.9.3>, 2008.

1546 Maksyutov, S., Oda, T., Saito, M., Janardanan, R., Belikov, D., Kaiser, J. W., Zhuravlev, R.,
 1547 Ganshin, A., Valsala, V. K., Andrews, A., Chmura, L., Dlugokencky, E., Haszpra, L.,
 1548 Langenfelds, R. L., Machida, T., Nakazawa, T., Ramonet, M., Sweeney, C., and Worthy, D.:
 1549 Technical note: A high-resolution inverse modelling technique for estimating surface CO₂ fluxes
 1550 based on the NIES-TM–FLEXPART coupled transport model and its adjoint, *Atmospheric*
 1551 *Chem. Phys.*, 21, 1245–1266, <https://doi.org/10.5194/acp-21-1245-2021>, 2021.

1552 Manning, A. C. and Keeling, R. F.: Global oceanic and land biotic carbon sinks from the Scripps
 1553 atmospheric oxygen flask sampling network, *Tellus B Chem. Phys. Meteorol.*, 58, 95,
 1554 <https://doi.org/10.1111/j.1600-0889.2006.00175.x>, 2006.

1555 Mellor, G. L. and Yamada, T.: A Hierarchy of Turbulence Closure Models for Planetary
 1556 Boundary Layers, *J. Atmospheric Sci.*,
 1557 [https://doi.org/10.1175/1520-0469\(1974\)031<1791:AHOTCM>2.0.CO;2](https://doi.org/10.1175/1520-0469(1974)031<1791:AHOTCM>2.0.CO;2), 1974.

1558 Miyazaki, K., Patra, P. K., Takigawa, M., Iwasaki, T., and Nakazawa, T.: Global-scale transport
 1559 of carbon dioxide in the troposphere, *J. Geophys. Res. Atmospheres*, 113, 2007JD009557,

1560 <https://doi.org/10.1029/2007JD009557>, 2008.

1561 Morgan, E. J., Manizza, M., Keeling, R. F., Resplandy, L., Mikaloff-Fletcher, S. E., Nevison, C.
1562 D., Jin, Y., Bent, J. D., Aumont, O., Doney, S. C., Dunne, J. P., John, J., Lima, I. D., Long, M. C.,
1563 and Rodgers, K. B.: An Atmospheric Constraint on the Seasonal Air-Sea Exchange of Oxygen
1564 and Heat in the Extratropics, *J. Geophys. Res. Oceans*, 126, e2021JC017510,
1565 <https://doi.org/10.1029/2021JC017510>, 2021.

1566 Naegler, T., Ciais, P., Rodgers, K., and Levin, I.: Excess radiocarbon constraints on air-sea gas
1567 exchange and the uptake of CO₂ by the oceans, *Geophys. Res. Lett.*, 33,
1568 <https://doi.org/10.1029/2005GL025408>, 2006.

1569 Naegler, T., Ciais, P., Orr, J. C., Aumont, O., and Rödenbeck, C.: On evaluating ocean models
1570 with atmospheric potential oxygen, *Tellus B Chem. Phys. Meteorol.*, 59,
1571 <https://doi.org/10.1111/j.1600-0889.2006.00197.x>, 2007.

1572 Najjar, R. G. and Keeling, R. F.: Mean annual cycle of the air-sea oxygen flux: A global view,
1573 *Glob. Biogeochem. Cycles*, 14, 573–584, <https://doi.org/10.1029/1999GB900086>, 2000.

1574 Nakanishi, M. and Niino, H.: An Improved Mellor–Yamada Level-3 Model with Condensation
1575 Physics: Its Design and Verification, *Bound.-Layer Meteorol.*, 112, 1–31,
1576 <https://doi.org/10.1023/B:BOUN.0000020164.04146.98>, 2004.

1577 Nevison, C., Munro, D., Lovenduski, N., Cassar, N., Keeling, R., Krummel, P., and Tjiputra, J.:
1578 Net Community Production in the Southern Ocean: Insights From Comparing Atmospheric
1579 Potential Oxygen to Satellite Ocean Color Algorithms and Ocean Models, *Geophys. Res. Lett.*,
1580 45, 10549–10559, <https://doi.org/10.1029/2018GL079575>, 2018.

1581 Nevison, C. D., Mahowald, N. M., Doney, S. C., Lima, I. D., and Cassar, N.: Impact of variable
1582 air-sea O₂ and CO₂ fluxes on atmospheric potential oxygen (APO) and land-ocean carbon sink
1583 partitioning, *Biogeosciences*, 5, 875–889, <https://doi.org/10.5194/bg-5-875-2008>, 2008.

1584 Nevison, C. D., Keeling, R. F., Kahru, M., Manizza, M., Mitchell, B. G., and Cassar, N.:
1585 Estimating net community production in the Southern Ocean based on atmospheric potential
1586 oxygen and satellite ocean color data, *Glob. Biogeochem. Cycles*, 26,
1587 <https://doi.org/10.1029/2011GB004040>, 2012.

1588 Nevison, C. D., Manizza, M., Keeling, R. F., Kahru, M., Bopp, L., Dunne, J., Tjiputra, J., Ilyina,
1589 T., and Mitchell, B. G.: Evaluating the ocean biogeochemical components of Earth system
1590 models using atmospheric potential oxygen and ocean color data, *Biogeosciences*, 12, 193–208,
1591 <https://doi.org/10.5194/bg-12-193-2015>, 2015.

1592 Nevison, C. D., Manizza, M., Keeling, R. F., Stephens, B. B., Bent, J. D., Dunne, J., Ilyina, T.,
1593 Long, M., Resplandy, L., Tjiputra, J., and Yukimoto, S.: Evaluating CMIP5 ocean
1594 biogeochemistry and Southern Ocean carbon uptake using atmospheric potential oxygen:
1595 Present-day performance and future projection, *Geophys. Res. Lett.*, 43, 2077–2085,
1596 <https://doi.org/10.1002/2015GL067584>, 2016.

1597 Nguyen, L. N. T., Meijer, H. A. J., van Leeuwen, C., Kers, B. A. M., Scheeren, H. A., Jones, A.
 1598 E., Brough, N., Barningham, T., Pickers, P. A., Manning, A. C., and Luijkx, I. T.: Two decades of
 1599 flask observations of atmospheric $\delta(\text{O}_2/\text{N}_2)$, CO_2 , and APO at stations Lütjehad (the Netherlands)
 1600 and Mace Head (Ireland), and 3 years from Halley station (Antarctica), *Earth Syst. Sci. Data*, 14,
 1601 991–1014, <https://doi.org/10.5194/essd-14-991-2022>, 2022.

1602 Niwa, Y., Tomita, H., Satoh, M., and Imasu, R.: A Three-Dimensional Icosahedral Grid
 1603 Advection Scheme Preserving Monotonicity and Consistency with Continuity for Atmospheric
 1604 Tracer Transport, *J. Meteorol. Soc. Jpn. Ser II*, 89, 255–268,
 1605 <https://doi.org/10.2151/jmsj.2011-306>, 2011.

1606 Niwa, Y., Machida, T., Sawa, Y., Matsueda, H., Schuck, T. J., Brenninkmeijer, C. A. M., Imasu,
 1607 R., and Satoh, M.: Imposing strong constraints on tropical terrestrial CO_2 fluxes using passenger
 1608 aircraft based measurements, *J. Geophys. Res. Atmospheres*, 117,
 1609 <https://doi.org/10.1029/2012JD017474>, 2012.

1610 Niwa, Y., Tomita, H., Satoh, M., Imasu, R., Sawa, Y., Tsuboi, K., Matsueda, H., Machida, T.,
 1611 Sasakawa, M., Belan, B., and Saigusa, N.: A 4D-Var inversion system based on the icosahedral
 1612 grid model (NICAM-TM 4D-Var v1.0) – Part 1: Offline forward and adjoint transport models,
 1613 *Geosci. Model Dev.*, 10, 1157–1174, <https://doi.org/10.5194/gmd-10-1157-2017>, 2017.

1614 Noda, A. T., Oouchi, K., Satoh, M., Tomita, H., Iga, S., and Tsushima, Y.: Importance of the
 1615 subgrid-scale turbulent moist process: Cloud distribution in global cloud-resolving simulations,
 1616 *Atmospheric Res.*, 96, 208–217, <https://doi.org/10.1016/j.atmosres.2009.05.007>, 2010.

1617 Numaguti, A., Takahashi, M., Nakajima, T., and Sumi, A.: Description of CCSR/NIES
 1618 Atmospheric General Circulation Model., CGER's Supercomput. Monogr. Rep., 3 (Ch 1),
 1619 National Institute for Environmental Studies, Tsukuba, Japan., 1997.

1620 Oda, T., Maksyutov, S., and Andres, R. J.: The Open-source Data Inventory for Anthropogenic
 1621 CO_2 version 2016 (ODIAC2016): a global monthly fossil fuel CO_2 gridded emissions data
 1622 product for tracer transport simulations and surface flux inversions, *Earth Syst. Sci. Data*, 10,
 1623 87–107, <https://doi.org/10.5194/essd-10-87-2018>, 2018.

1624 Parazoo, N. C., Denning, A. S., Berry, J. A., Wolf, A., Randall, D. A., Kawa, S. R., Pauluis, O.,
 1625 and Doney, S. C.: Moist synoptic transport of CO_2 along the mid-latitude storm track, *Geophys.*
 1626 *Res. Lett.*, 38, 2011GL047238, <https://doi.org/10.1029/2011GL047238>, 2011.

1627 Patra, P. K., Law, R. M., Peters, W., Rödenbeck, C., Takigawa, M., Aulagnier, C., Baker, I.,
 1628 Bergmann, D. J., Bousquet, P., Brandt, J., Bruhwiler, L., Cameron-Smith, P. J., Christensen, J.
 1629 H., Delage, F., Denning, A. S., Fan, S., Geels, C., Houweling, S., Imasu, R., Karstens, U., Kawa,
 1630 S. R., Kleist, J., Krol, M. C., Lin, S.-J., Lokupitiya, R., Maki, T., Maksyutov, S., Niwa, Y.,
 1631 Onishi, R., Parazoo, N., Pieterse, G., Rivier, L., Satoh, M., Serrar, S., Taguchi, S., Vautard, R.,
 1632 Vermeulen, A. T., and Zhu, Z.: TransCom model simulations of hourly atmospheric CO_2 :
 1633 Analysis of synoptic-scale variations for the period 2002–2003, *Glob. Biogeochem. Cycles*, 22,
 1634 <https://doi.org/10.1029/2007GB003081>, 2008.

1635 Patra, P. K., Houweling, S., Krol, M., Bousquet, P., Belikov, D., Bergmann, D., Bian, H.,

1636 Cameron-Smith, P., Chipperfield, M. P., Corbin, K., Fortems-Cheiney, A., Fraser, A., Gloor, E.,
 1637 Hess, P., Ito, A., Kawa, S. R., Law, R. M., Loh, Z., Maksyutov, S., Meng, L., Palmer, P. I., Prinn,
 1638 R. G., Rigby, M., Saito, R., and Wilson, C.: TransCom model simulations of CH₄ and related
 1639 species: linking transport, surface flux and chemical loss with CH₄ variability in the troposphere
 1640 and lower stratosphere, *Atmospheric Chem. Phys.*, 11, 12813–12837,
 1641 <https://doi.org/10.5194/acp-11-12813-2011>, 2011.

1642 Patra, P. K., Takigawa, M., Watanabe, S., Chandra, N., Ishijima, K., and Yamashita, Y.: Improved
 1643 Chemical Tracer Simulation by MIROC4.0-based Atmospheric Chemistry-Transport Model
 1644 (MIROC4-ACTM), *SOLA*, 14, 91–96, <https://doi.org/10.2151/sola.2018-016>, 2018.

1645 Peiro, H., Crowell, S., Schuh, A., Baker, D. F., O'Dell, C., Jacobson, A. R., Chevallier, F., Liu,
 1646 J., Eldering, A., Crisp, D., Deng, F., Weir, B., Basu, S., Johnson, M. S., Philip, S., and Baker, I.:
 1647 Four years of global carbon cycle observed from the Orbiting Carbon Observatory 2 (OCO-2)
 1648 version 9 and in situ data and comparison to OCO-2 version 7, *Atmospheric Chem. Phys.*, 22,
 1649 1097–1130, <https://doi.org/10.5194/acp-22-1097-2022>, 2022.

1650 Pickers, P. A., Manning, A. C., Sturges, W. T., Le Quéré, C., Mikaloff Fletcher, S. E., Wilson, P.
 1651 A., and Etchells, A. J.: In situ measurements of atmospheric O₂ and CO₂ reveal an unexpected O₂
 1652 signal over the tropical Atlantic Ocean, *Glob. Biogeochem. Cycles*, 31, 1289–1305,
 1653 <https://doi.org/10.1002/2017GB005631>, 2017.

1654 Pickers, P. A., Manning, A. C., Le Quéré, C., Forster, G. L., Luijkx, I. T., Gerbig, C., Fleming, L.
 1655 S., and Sturges, W. T.: Novel quantification of regional fossil fuel CO₂ reductions during
 1656 COVID-19 lockdowns using atmospheric oxygen measurements, *Sci. Adv.*, 8, eabl9250,
 1657 <https://doi.org/10.1126/sciadv.abl9250>, 2022.

1658 Resplandy, L., Keeling, R. F., Stephens, B. B., Bent, J. D., Jacobson, A., Rödenbeck, C., and
 1659 Khatiwala, S.: Constraints on oceanic meridional heat transport from combined measurements of
 1660 oxygen and carbon, *Clim. Dyn.*, 47, 3335–3357, <https://doi.org/10.1007/s00382-016-3029-3>,
 1661 2016.

1662 Resplandy, L., Keeling, R. F., Eddebbar, Y., Brooks, M., Wang, R., Bopp, L., Long, M. C.,
 1663 Dunne, J. P., Koeve, W., and Oschlies, A.: Quantification of ocean heat uptake from changes in
 1664 atmospheric O₂ and CO₂ composition, *Sci. Rep.*, 9, 20244,
 1665 <https://doi.org/10.1038/s41598-019-56490-z>, 2019.

1666 Rio, C. and Hourdin, F.: A Thermal Plume Model for the Convective Boundary Layer:
 1667 Representation of Cumulus Clouds, *J. Atmospheric Sci.*, <https://doi.org/10.1175/2007JAS2256.1>,
 1668 2008.

1669 Rödenbeck, C., Quéré, C. L., Heimann, M., and Keeling, R. F.: Interannual variability in oceanic
 1670 biogeochemical processes inferred by inversion of atmospheric O₂/N₂ and CO₂ data, *Tellus B*
 1671 *Chem. Phys. Meteorol.*, 60, 685–705, <https://doi.org/10.1111/j.1600-0889.2008.00375.x>, 2008.

1672 Rödenbeck, C., Adcock, K. E., Eritt, M., Gachkivskyi, M., Gerbig, C., Hammer, S., Jordan, A.,
 1673 Keeling, R. F., Levin, I., Maier, F., Manning, A. C., Moossen, H., Munassar, S., Pickers, P. A.,
 1674 Rothe, M., Tohjima, Y., and Zaehle, S.: The suitability of atmospheric oxygen measurements to

1675 constrain western European fossil-fuel CO₂ emissions and their trends, *Atmospheric Chem.*
1676 *Phys.*, 23, 15767–15782, <https://doi.org/10.5194/acp-23-15767-2023>, 2023.

1677 Russell, G. L. and Lerner, J. A.: A New Finite-Differencing Scheme for the Tracer Transport
1678 Equation, *J. Appl. Meteorol.*, 20, 1483–1498,
1679 [https://doi.org/10.1175/1520-0450\(1981\)020<1483:ANFDSF>2.0.CO;2](https://doi.org/10.1175/1520-0450(1981)020<1483:ANFDSF>2.0.CO;2), 1981.

1680 Sallée, J.-B., Shuckburgh, E., Bruneau, N., Meijers, A. J. S., Bracegirdle, T. J., and Wang, Z.:
1681 Assessment of Southern Ocean mixed-layer depths in CMIP5 models: Historical bias and forcing
1682 response, *J. Geophys. Res. Oceans*, 118, 1845–1862, <https://doi.org/10.1002/jgrc.20157>, 2013.

1683 Santoni, G. W., Daube, B. C., Kort, E. A., Jiménez, R., Park, S., Pittman, J. V., Gottlieb, E.,
1684 Xiang, B., Zahniser, M. S., Nelson, D. D., McManus, J. B., Peischl, J., Ryerson, T. B., Holloway,
1685 J. S., Andrews, A. E., Sweeney, C., Hall, B., Hintsa, E. J., Moore, F. L., Elkins, J. W., Hurst, D.
1686 F., Stephens, B. B., Bent, J., and Wofsy, S. C.: Evaluation of the airborne quantum cascade laser
1687 spectrometer (QCLS) measurements of the carbon and greenhouse gas suite – CO₂, CH₄, N₂O,
1688 and CO – during the CalNex and HIPPO campaigns, *Atmospheric Meas. Tech.*, 7, 1509–1526,
1689 <https://doi.org/10.5194/amt-7-1509-2014>, 2014.

1690 Satoh, M., Tomita, H., Yashiro, H., Miura, H., Kodama, C., Seiki, T., Noda, A. T., Yamada, Y.,
1691 Goto, D., Sawada, M., Miyoshi, T., Niwa, Y., Hara, M., Ohno, T., Iga, S., Arakawa, T., Inoue, T.,
1692 and Kubokawa, H.: The Non-hydrostatic Icosahedral Atmospheric Model: description and
1693 development, *Prog. Earth Planet. Sci.*, 1, 18, <https://doi.org/10.1186/s40645-014-0018-1>, 2014.

1694 Schuh, A. E. and Jacobson, A. R.: Uncertainty in parameterized convection remains a key
1695 obstacle for estimating surface fluxes of carbon dioxide, *Atmospheric Chem. Phys.*, 23,
1696 6285–6297, <https://doi.org/10.5194/acp-23-6285-2023>, 2023.

1697 Schuh, A. E., Jacobson, A. R., Basu, S., Weir, B., Baker, D., Bowman, K., Chevallier, F.,
1698 Crowell, S., Davis, K. J., Deng, F., Denning, S., Feng, L., Jones, D., Liu, J., and Palmer, P. I.:
1699 Quantifying the Impact of Atmospheric Transport Uncertainty on CO₂ Surface Flux Estimates,
1700 *Glob. Biogeochem. Cycles*, 33, 484–500, <https://doi.org/10.1029/2018GB006086>, 2019.

1701 Schuldt, K. N., Mund, J., Luijkx, I. T., Aalto, T., Abshire, J. B., Aikin, K., Andrews, A., Aoki, S.,
1702 Apadula, F., Baier, B., Bakwin, P., Bartyzel, J., Bentz, G., Bergamaschi, P., Beyersdorf, A.,
1703 Biermann, T., Biraud, S. C., Boenisch, H., Bowling, D., Brailsford, G., Chen, G., Chen, H.,
1704 Chmura, L., Clark, S., Climadat, S., Colomb, A., Commane, R., Conil, S., Cox, A., Cristofanelli,
1705 P., Cuevas, E., Curcoll, R., Daube, B., Davis, K., De Mazière, M., De Wekker, S., Della Coletta,
1706 J., Delmotte, M., DiGangi, J. P., Dlugokencky, E., Elkins, J. W., Emmenegger, L., Fang, S.,
1707 Fischer, M. L., Forster, G., Frumau, A., Galkowski, M., Gatti, L. V., Gehrlein, T., Gerbig, C.,
1708 Gheusi, F., Gloor, E., Gomez-Trueba, V., Goto, D., Griffiths, T., Hammer, S., Hanson, C., Haszpra,
1709 L., Hatakka, J., Heimann, M., Heliasz, M., Hensen, A., Hermanssen, O., Hintsa, E., Holst, J.,
1710 Ivakhov, V., Jaffe, D., Joubert, W., Karion, A., Kawa, S. R., Kazan, V., Keeling, R., Keronen, P.,
1711 Kolari, P., Kominkova, K., Kort, E., Kozlova, E., Krummel, P., Kubistin, D., Labuschagne, C.,
1712 Lam, D. H., Langenfelds, R., Laurent, O., Laurila, T., Lauvaux, T., Lavric, J., Law, B., Lee, O.
1713 S., Lee, J., Lehner, I., Leppert, R., Leuenberger, M., Levin, I., Levula, J., Lin, J., Lindauer, M.,
1714 Loh, Z., Lopez, M., Machida, T., et al.: Multi-laboratory compilation of atmospheric carbon

1715 dioxide data for the period 1957-2020; obspack_co2_1_GLOBALVIEWplus_v7.0_2021-08-18, ,
1716 <https://doi.org/10.25925/20210801>, 2021.

1717 Severinghaus, J.: Studies of the terrestrial O₂ and carbon cycles in sand dune gases and in
1718 Biosphere 2, Columbia University, 1995.

1719 Sharp, J. D., Fassbender, A. J., Carter, B. R., Johnson, G. C., Schultz, C., and Dunne, J. P.:
1720 GOBAI-O₂ : temporally and spatially resolved fields of ocean interior dissolved oxygen over
1721 nearly 2 decades, *Earth Syst. Sci. Data*, 15, 4481–4518,
1722 <https://doi.org/10.5194/essd-15-4481-2023>, 2023.

1723 Steinbach, J., Gerbig, C., Rödenbeck, C., Karstens, U., Minejima, C., and Mukai, H.: The CO₂
1724 release and Oxygen uptake from Fossil Fuel Emission Estimate (COFFEE) dataset: effects from
1725 varying oxidative ratios, *Atmospheric Chem. Phys.*, 11, 6855–6870,
1726 <https://doi.org/10.5194/acp-11-6855-2011>, 2011.

1727 Stephens, B.: ORCAS Merge Products. Version 1.0. UCAR/NCAR - Earth Observing
1728 Laboratory, <https://doi.org/10.5065/D6SB445X>., 2017.

1729 Stephens, B., Keeling, R., Bent, J., Watt, A., Shertz, S., and Paplawsky, W.: HIPPO-1 airborne
1730 oxygen instrument. Version 2.0. UCAR/NCAR—Earth Observing Laboratory.,
1731 <https://doi.org/10.5065/D6J38QVV>, 2021a.

1732 Stephens, B., Keeling, R., Bent, J., Watt, A., Shertz, S., and Paplawsky, W.: HIPPO-2 airborne
1733 oxygen instrument. Version 2.0. UCAR/NCAR—Earth Observing Laboratory.,
1734 <https://doi.org/10.5065/D65Q4TF0>, 2021b.

1735 Stephens, B., Keeling, R., Bent, J., Watt, A., Shertz, S., and Paplawsky, W.: HIPPO-3 airborne
1736 oxygen instrument. Version 2.0. UCAR/NCAR—Earth Observing Laboratory.,
1737 <https://doi.org/10.5065/D67H1GXJ>, 2021c.

1738 Stephens, B., Keeling, R., Bent, J., Watt, A., Shertz, S., and Paplawsky, W.: HIPPO-4 airborne
1739 oxygen instrument. Version 2.0. UCAR/NCAR—Earth Observing Laboratory.,
1740 <https://doi.org/10.5065/D679431D>, 2021d.

1741 Stephens, B., Keeling, R., Bent, J., Watt, A., Shertz, S., and Paplawsky, W.: HIPPO-5 airborne
1742 oxygen instrument. Version 2.0. UCAR/NCAR—Earth Observing Laboratory.,
1743 <https://doi.org/10.5065/D6WW7G0D>, 2021e.

1744 Stephens, B., Keeling, R., Bent, J., Watt, A., Shertz, S., and Paplawsky, W.: ORCAS Airborne
1745 Oxygen Instrument. Version 2.0. UCAR/NCAR - Earth Observing Laboratory.,
1746 <https://doi.org/10.5065/D6N29VC6>, 2021f.

1747 Stephens, B., Long, M., Jin, Y., Chandra, N., Chevallier, F., Hooghiem, J., Luijkx, I., Maksyutov,
1748 S., Morgan, E., Niwa, Y., Patra, P., Rodenbeck, C., and Vance, J.: Atmospheric Potential Oxygen
1749 forward Model Intercomparison Project (APO-MIP), <https://doi.org/10.5065/F3PW-A676>, 2025.

1750 Stephens, B. B.: ARSV Laurence M. Gould Atmospheric O₂ and CO₂ Measurements. Version

1751 1.0. UCAR/NCAR - Earth Observing Laboratory, <https://doi.org/10.26023/FDDD-PC3X-4M0X>,
1752 2025.

1753 Stephens, B. B., Keeling, R. F., Heimann, M., Six, K. D., Murnane, R., and Caldeira, K.: Testing
1754 global ocean carbon cycle models using measurements of atmospheric O₂ and CO₂
1755 concentration, *Glob. Biogeochem. Cycles*, 12, 213–230, <https://doi.org/10.1029/97GB03500>,
1756 1998.

1757 Stephens, B. B., Keeling, R. F., and Paplawsky, W. J.: Shipboard measurements of atmospheric
1758 oxygen using a vacuum-ultraviolet absorption technique, *Tellus B Chem. Phys. Meteorol.*, 75B,
1759 857–878, <https://doi.org/10.3402/tellusb.v55i4.16386>, 2003.

1760 Stephens, B. B., Gurney, K. R., Tans, P. P., Sweeney, C., Peters, W., Bruhwiler, L., Ciais, P.,
1761 Ramonet, M., Bousquet, P., Nakazawa, T., Aoki, S., Machida, T., Inoue, G., Vinnichenko, N.,
1762 Lloyd, J., Jordan, A., Heimann, M., Shibistova, O., Langenfelds, R. L., Steele, L. P., Francey, R.
1763 J., and Denning, A. S.: Weak Northern and Strong Tropical Land Carbon Uptake from Vertical
1764 Profiles of Atmospheric CO₂, *Science*, 316, 1732–1735, <https://doi.org/10.1126/science.1137004>,
1765 2007.

1766 Stephens, B. B., Long, M. C., Keeling, R. F., Kort, E. A., Sweeney, C., Apel, E. C., Atlas, E. L.,
1767 Beaton, S., Bent, J. D., Blake, N. J., Bresch, J. F., Casey, J., Daube, B. C., Diao, M., Diaz, E.,
1768 Dierssen, H., Donets, V., Gao, B.-C., Gierach, M., Green, R., Haag, J., Hayman, M., Hills, A. J.,
1769 Hoecker-Martínez, M. S., Honomichl, S. B., Hornbrook, R. S., Jensen, J. B., Li, R.-R.,
1770 McCubbin, I., McKain, K., Morgan, E. J., Nolte, S., Powers, J. G., Rainwater, B., Randolph, K.,
1771 Reeves, M., Schauffler, S. M., Smith, K., Smith, M., Stith, J., Stossmeister, G., Toohey, D. W.,
1772 and Watt, A. S.: The O₂/N₂ Ratio and CO₂ Airborne Southern Ocean Study, *Bull. Am. Meteorol.*
1773 *Soc.*, 99, 381–402, <https://doi.org/10.1175/BAMS-D-16-0206.1>, 2018.

1774 Stephens, B. B., Morgan, E. J., Bent, J. D., Keeling, R. F., Watt, A. S., Shertz, S. R., and Daube,
1775 B. C.: Airborne measurements of oxygen concentration from the surface to the lower
1776 stratosphere and pole to pole, *Atmospheric Meas. Tech.*, 14, 2543–2574,
1777 <https://doi.org/10.5194/amt-14-2543-2021>, 2021g.

1778 Stohl, A., Forster, C., Frank, A., Seibert, P., and Wotawa, G.: Technical note: The Lagrangian
1779 particle dispersion model FLEXPART version 6.2, *Atmospheric Chem. Phys.*, 5, 2461–2474,
1780 <https://doi.org/10.5194/acp-5-2461-2005>, 2005.

1781 Thompson, C., Wofsy, S. C., Prather, M. J., Newman, P. A., Hanisco, T. F., Ryerson, T. B.,
1782 Fahey, D. W., Apel, E. C., Brock, C. A., Brune, W. H., Froyd, K., Katich, J. M., Nicely, J. M.,
1783 Peischl, J., Ray, E., Veres, P. R., Wang, S., Allen, H. M., Asher, E., Bian, H., Blake, D.,
1784 Bourgeois, I., Budney, J., Bui, T. P., Butler, A., Campuzano-Jost, P., Chang, C., Chin, M.,
1785 Commane, R., Correa, G., Crounse, J. D., Daube, B., Dibb, J. E., DiGangi, J. P., Diskin, G. S.,
1786 Dollner, M., Elkins, J. W., Fiore, A. M., Flynn, C. M., Guo, H., Hall, S. R., Hannun, R. A., Hills,
1787 A., Hints, E. J., Hodzic, A., Hornbrook, R. S., Huey, L. G., Jimenez, J. L., Keeling, R. F., Kim,
1788 M. J., Kupc, A., Lacey, F., Lait, L. R., Lamarque, J.-F., Liu, J., McKain, K., Meinardi, S., Miller,
1789 D. O., Montzka, S. A., Moore, F. L., Morgan, E. J., Murphy, D. M., Murray, L. T., Nault, B. A.,
1790 Neuman, J. A., Nguyen, L., Gonzalez, Y., Rollins, A., Rosenlof, K., Sargent, M., Schill, G.,

1791 Schwarz, J. P., Clair, J. M. St., Steenrod, S. D., Stephens, B. B., Strahan, S. E., Strode, S. A.,
 1792 Sweeney, C., Thames, A. B., Ullmann, K., Wagner, N., Weber, R., Weinzierl, B., Wennberg, P.
 1793 O., Williamson, C. J., Wolfe, G. M., and Zeng, L.: The NASA Atmospheric Tomography (ATom)
 1794 Mission: Imaging the Chemistry of the Global Atmosphere, *Bull. Am. Meteorol. Soc.*, 103,
 1795 E761–E790, <https://doi.org/10.1175/BAMS-D-20-0315.1>, 2022.

1796 Thompson, R., Manning, A. C., Lowe, D. C., and Weatherburn, D. C.: A ship-based
 1797 methodology for high precision atmospheric oxygen measurements and its application in the
 1798 Southern Ocean region, *Tellus B Chem. Phys. Meteorol.*, 59, 643,
 1799 <https://doi.org/10.1111/j.1600-0889.2007.00292.x>, 2007.

1800 Thompson, R. L., Patra, P. K., Ishijima, K., Saikawa, E., Corazza, M., Karstens, U., Wilson, C.,
 1801 Bergamaschi, P., Dlugokencky, E., Sweeney, C., Prinn, R. G., Weiss, R. F., O'Doherty, S., Fraser,
 1802 P. J., Steele, L. P., Krummel, P. B., Saunio, M., Chipperfield, M., and Bousquet, P.: TransCom
 1803 N₂O model inter-comparison – Part 1: Assessing the influence of transport and surface fluxes on
 1804 tropospheric N₂O variability, *Atmospheric Chem. Phys.*, 14, 4349–4368,
 1805 <https://doi.org/10.5194/acp-14-4349-2014>, 2014.

1806 Tiedtke, M.: A Comprehensive Mass Flux Scheme for Cumulus Parameterization in Large-Scale
 1807 Models, *Mon. Weather Rev.*, 117, 1779–1800,
 1808 [https://doi.org/10.1175/1520-0493\(1989\)117<1779:ACMFSF>2.0.CO;2](https://doi.org/10.1175/1520-0493(1989)117<1779:ACMFSF>2.0.CO;2), 1989.

1809 Tohjima, Y., Minejima, C., Mukai, H., Machida, T., Yamagishi, H., and Nojiri, Y.: Analysis of
 1810 seasonality and annual mean distribution of atmospheric potential oxygen (APO) in the Pacific
 1811 region, *Glob. Biogeochem. Cycles*, 26, 2011GB004110, <https://doi.org/10.1029/2011GB004110>,
 1812 2012.

1813 Tohjima, Y., Terao, Y., Mukai, H., Machida, T., Nojiri, Y., and Maksyutov, S.: ENSO-related
 1814 variability in latitudinal distribution of annual mean atmospheric potential oxygen (APO) in the
 1815 equatorial Western Pacific, *Tellus B Chem. Phys. Meteorol.*, 67, 25869,
 1816 <https://doi.org/10.3402/tellusb.v67.25869>, 2015.

1817 Tohjima, Y., Mukai, H., Machida, T., Hoshina, Y., and Nakaoka, S.-I.: Global carbon budgets
 1818 estimated from atmospheric O₂/N₂ and CO₂ observations in the western Pacific region over a
 1819 15-year period, *Atmospheric Chem. Phys.*, 19, 9269–9285,
 1820 <https://doi.org/10.5194/acp-19-9269-2019>, 2019.

1821 Tohjima, Y., Shirai, T., Ishizawa, M., Mukai, H., Machida, T., Sasakawa, M., Terao, Y., Tsuboi,
 1822 K., Takao, S., and Nakaoka, S.: Observed APO Seasonal Cycle in the Pacific: Estimation of
 1823 Autumn O₂ Oceanic Emissions, *Glob. Biogeochem. Cycles*, 38, e2024GB008230,
 1824 <https://doi.org/10.1029/2024GB008230>, 2024.

1825 Truong, S. C. H., Huang, Y., Lang, F., Messmer, M., Simmonds, I., Siems, S. T., and Manton, M.
 1826 J.: A Climatology of the Marine Atmospheric Boundary Layer Over the Southern Ocean From
 1827 Four Field Campaigns During 2016–2018, *J. Geophys. Res. Atmospheres*, 125, e2020JD033214,
 1828 <https://doi.org/10.1029/2020JD033214>, 2020.

1829 Tsujino, H., Urakawa, S., Nakano, H., Small, R. J., Kim, W. M., Yeager, S. G., Danabasoglu, G.,

1830 Suzuki, T., Bamber, J. L., Bentsen, M., Böning, C. W., Bozec, A., Chassignet, E. P., Curchitser,
1831 E., Boeira Dias, F., Durack, P. J., Griffies, S. M., Harada, Y., Ilicak, M., Josey, S. A., Kobayashi,
1832 C., Kobayashi, S., Komuro, Y., Large, W. G., Le Sommer, J., Marsland, S. J., Masina, S.,
1833 Scheinert, M., Tomita, H., Valdivieso, M., and Yamazaki, D.: JRA-55 based surface dataset for
1834 driving ocean–sea-ice models (JRA55-do), *Ocean Model.*, 130, 79–139,
1835 <https://doi.org/10.1016/j.ocemod.2018.07.002>, 2018.

1836 Van Leer, B.: Towards the ultimate conservative difference scheme. IV. A new approach to
1837 numerical convection, *J. Comput. Phys.*, 23, 276–299,
1838 [https://doi.org/10.1016/0021-9991\(77\)90095-X](https://doi.org/10.1016/0021-9991(77)90095-X), 1977.

1839 Vogelesang, D. H. P. and Holtslag, A. A. M.: Evaluation and model impacts of alternative
1840 boundary-layer height formulations, *Bound.-Layer Meteorol.*, 81, 245–269,
1841 <https://doi.org/10.1007/BF02430331>, 1996.

1842 Watanabe, S., Miura, H., Sekiguchi, M., Nagashima, T., Sudo, K., Emori, S., and Kawamiya, M.:
1843 Development of an Atmospheric General Circulation Model for Integrated Earth System
1844 Modeling on the Earth Simulator, *J. Earth Simulator*, 9, 27–35, <https://doi.org/10.32131/jes.9.27>,
1845 2008.

1846 Wofsy, S.: ATom: Merged atmospheric chemistry, trace gases, and aerosols, version 2 (version
1847 2.0). ORNL Distributed Active Archive Center., <https://doi.org/10.3334/ORNLDAAAC/1925>,
1848 2021.

1849 Wofsy, S. C.: HIPPER Pole-to-Pole Observations (HIPPO): fine-grained, global-scale
1850 measurements of climatically important atmospheric gases and aerosols, *Philos. Trans. R. Soc.*
1851 *A*, 369, 2073–2086, <https://doi.org/10.1098/rsta.2010.0313>, 2011.

1852 Wofsy, S. C.: HIPPO merged 10-second meteorology, atmospheric chemistry, and aerosol data.
1853 Version 1.0. UCAR/NCAR - Earth Observing Laboratory.,
1854 https://doi.org/10.3334/CDIAC/HIPPO_010, 2017.

1855 Worrall, F., Clay, G. D., Masiello, C. A., and Mynheer, G.: Estimating the oxidative ratio of the
1856 global terrestrial biosphere carbon, *Biogeochemistry*, 115, 23–32,
1857 <https://doi.org/10.1007/s10533-013-9877-6>, 2013.

1858 Yeager, S. G., Rosenbloom, N., Glanville, A. A., Wu, X., Simpson, I., Li, H., Molina, M. J.,
1859 Krumhardt, K., Mogen, S., Lindsay, K., Lombardozzi, D., Wieder, W., Kim, W. M., Richter, J.
1860 H., Long, M., Danabasoglu, G., Bailey, D., Holland, M., Lovenduski, N., Strand, W. G., and
1861 King, T.: The Seasonal-to-Multiyear Large Ensemble (SMYLE) prediction system using the
1862 Community Earth System Model version 2, *Geosci. Model Dev.*, 15, 6451–6493,
1863 <https://doi.org/10.5194/gmd-15-6451-2022>, 2022.

1864 Zhang, G. J. and McFarlane, N. A.: Sensitivity of climate simulations to the parameterization of
1865 cumulus convection in the Canadian climate centre general circulation model,
1866 *Atmosphere-Ocean*, 33, 407–446, <https://doi.org/10.1080/07055900.1995.9649539>, 1995.